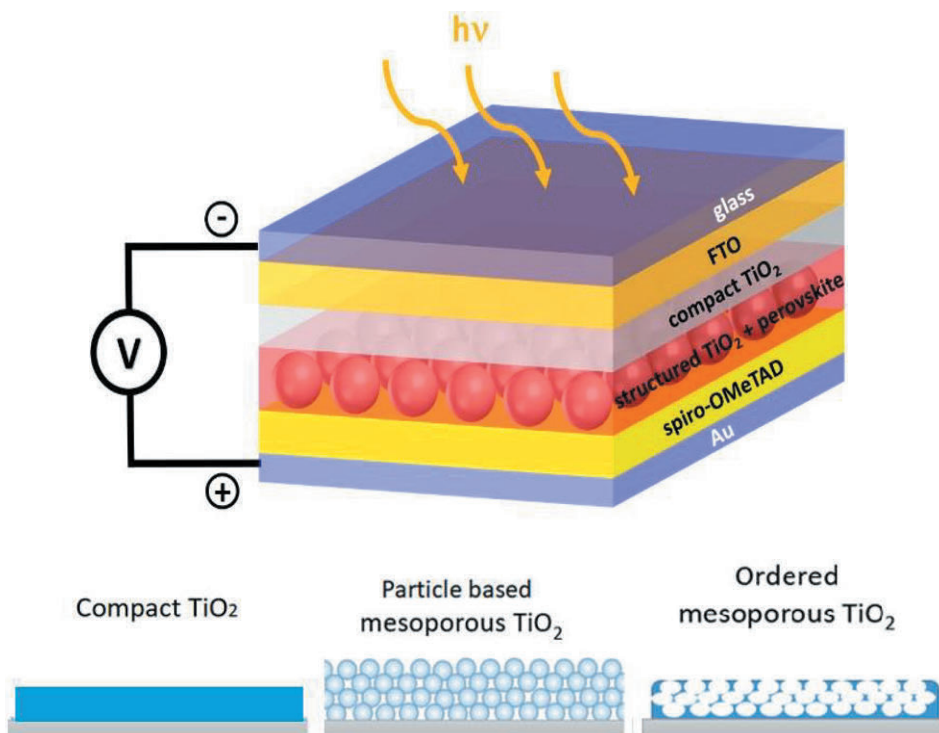


Muhammad Talha Masood

Solution-Processable Compact and Mesoporous Titanium Dioxide Thin Films as Electron-Selective Layers for Perovskite Solar Cells





Muhammad Talha Masood

Education:

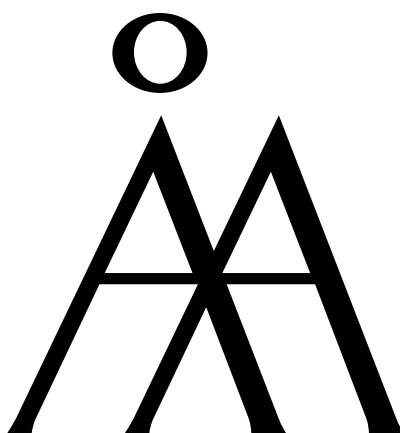
Bachelor of Science in Metallurgy & Materials Engineering
Ghulam Ishaq Khan Institute of Science & Technology (GIKI), Topi, Pakistan, 2009.

Master of Science in Engineering Materials Science
KTH, Royal Institute of Technology, Stockholm, Sweden, 2012.

Research interest:

Thin film photovoltaics, materials synthesis for solid oxide fuel cells (SOFCs),
ferrous and ferromagnetic shape memory alloys.

Solution-Processable Compact and Mesoporous Titanium Dioxide Thin Films as Electron-Selective Layers for Perovskite Solar Cells



Muhammad Talha Masood

Physical Chemistry

Laboratory of Molecular Science & Engineering

Faculty of Science and Engineering

Åbo Akademi University

Turku, Finland

2020

Supervised by:

Dr. Jan-Henrik Smått
Laboratory of Molecular Science & Engineering
Åbo Akademi University
Finland

Prof. Jouko Peltonen
Laboratory of Molecular Science & Engineering
Åbo Akademi University
Finland

Reviewed by:

Prof. Monica Lira-Cantu
Group leader; Nanostructured Materials for Photovoltaic Energy,
Catalan Institute of Nanoscience and Nanotechnology
Barcelona, Spain

Prof. Kati Miettunen
Faculty of Science & Engineering
University of Turku
Turku, Finland

Opponent:

Prof. Kati Miettunen
Faculty of Science & Engineering
University of Turku
Turku, Finland

ISBN 978-952-12-3956-4
Painosalama Oy, Turku, Finland 2020

“Those who are merciful will be shown mercy by the most Merciful. Be merciful to those on earth, and the One in heavens will have mercy upon you”.

Prophet Muhammad (SAW).

Dedicated to my beloved father, “**Mr. Malik Masood Sadiq**” who is the main person behind my educational progress.

Preface

First of all, I would like to thank my Kind and Merciful creator (Allah SWT) who kept me steadfast throughout this project. Without His assistance and mercy, I could have never achieved anything in my life. I am very grateful to my supervisor Dr. Jan-Henrik Smått, first of all for giving me an opportunity in this project and supporting me through the ups and downs during my doctoral studies. I am also thankful to Prof. Jouko Peltonen for his co-supervision and over all support.

This research work was initiated under financial support from “National University of Science & Technology” (NUST), Pakistan in March 2015. Many thanks to NUST for its contribution. I would also like to greatly acknowledge the Academy of Finland (2018-2019) and Jane & Aatos Erkkö Foundation (2019-2020) for additional financial support for this project.

My special gratitude goes to Dr. Paola Vivo, MSc Pontus Wistbacka and MSc. Annina Ojanperä who helped me during initial challenges such as the fabrication of perovskite active layers and devices by using two-step sequential deposition technique. For my third study where I was supposed to make planar-heterojunction PSCs, two-step sequential deposition method was not found to be an appropriate approach to get high efficiency devices. At this crucial stage, Dr. Mahboubeh Hadadian taught me the fabrication procedure for triple cation one-step perovskite via anti-solvent approach to prepare a good quality perovskite active layer.

I would like to specially thank Prof Ronald Österbacka and his students, Dr. Simon Sanden, Dr. Mathias Nyman, MSc Staffan Dahlström, MSc Christian Ahläng, Dr. Oskar J. Sandberg for their technical suggestions behind the device physics.

Special thanks to Dr. Christian Weinberger for helping me with inevitable difficulties while writing my first manuscript. He further extended his support through useful suggestions for the rest of this project.

MSc. Linus Silvander is highly acknowledged for being always available for SEM analysis. I am also grateful for prompt technical support from MSc Kenneth Stenlund and MSc Kjell-Mikael Källman.

I would also like to thank all my co-authors and team workers for their contributions namely Dr. Mahboubeh Hadadian, MSc Syeda Qudsia, MSc Emil Rosqvist, Dr. Jawad Sarfraz, Dr. Ghufra Hashmi, Dr. Kerttu Aitola and Professor Peter D. Lund. Special thanks to Dr. Maning Liu for performing steady state and time resolved photoluminescence measurements on my samples.

I am grateful to my lovely parents (Mr. Malik Masood Sadiq and Ms. Rukhsana Masood) since they have the greatest contribution in my education. On the other hand, my younger sisters (Hadia and Hala) were always a source of moral support. My sincere gratitude to my wife (Fatima) and lovely kids (Ibrahim & Abdullah) for providing a jolly and peaceful atmosphere to enjoy my research in Turkey.

I would like to pay special thanks to my mentor, Mufti Kamaluddin Ahmed who encouraged me to pursue research based career. Lastly many thanks to my teachers, Mufti Fawad Ali, Mufti Faheem Usman and Mufti Mahir Jameel for spiritual support and encouragement throughout my stay in Finland.

Table of Contents

Preface	4
Svensk sammanfattning	7
Abstract	9
List of abbreviations	11
List of publications	12
Supporting publication	12
Contribution of the author	13
1. Introduction and outline	14
2. Background and literature review	16
2.1. The sunlight as an infinite source of energy	16
2.2. Electricity generation from solar light	17
2.3. Types of solar cells	18
2.4. Perovskite solar cells	22
2.4.1. Working principle of a PSC	22
2.4.2. Structural evolution of the perovskite solar cell	24
2.4.3. Organo-lead halide perovskite as a photoactive material	25
2.4.4. Charge-selective contacts for PSCs	27
2.5. TiO ₂ electron-selective layer	28
2.6. Ordered mesoporous TiO ₂ layers	38
3. Aims of the study	41
4. Experimental	43
4.1. Materials	43
4.2. Device architecture	44
4.3. Device preparation	44
4.3.1. Compact TiO ₂ film preparation	45
4.3.2. Mesoscopic TiO ₂ scaffold	47
4.3.3. Organo-lead halide perovskite deposition	47
4.3.4. Hole-selective layer	48
4.3.5. Gold back contacts	49
4.4. Characterization methods	49
4.4.1. X-ray reflectometry	49
4.4.2. Grazing incidence x-ray diffraction	50
4.4.3. X-ray photoelectron spectroscopy	50
4.4.4. Atomic force microscopy	51
4.4.5. Ultraviolet-visible light spectroscopy	51

4.4.6.	Scanning electron microscopy.....	52
4.4.7.	Water contact angle measurements.....	53
4.4.8.	Photoluminescence spectroscopy.....	53
4.4.9.	Device characterization by current density versus voltage measurements.....	54
4.4.10.	Surface recombination measurements using dark MIS CELIV	56
5.	Results and discussion.....	58
5.1.	Optimization of ultrathin dip-coated compact TiO ₂ film thickness by tuning the molar concentration of TiCl ₄ precursor in the initial sol (Study 1)	58
5.1.1.	Crystal structure, thickness and densities of compact TiO ₂ films	58
5.1.2.	Topographical features of FTO substrates with and without compact TiO ₂ layers of different thicknesses	60
5.1.3.	Detection of pinholes through compact TiO ₂ films on top of FTO substrates	62
5.1.4.	Device performance versus compact TiO ₂ film thickness	64
5.1.5.	Conclusions from Study 1:	66
5.2.	Effect of surface activation of mesoscopic TiO ₂ scaffold (Study 2).....	66
5.2.1.	Characterization of PbI ₂ -coated mesoporous TiO ₂ and corresponding perovskite after conversion.....	67
5.2.2.	Device performance.....	70
5.2.3.	Proposed mechanism for the PbI ₂ formation and its conversion to perovskite	72
5.2.4.	Conclusions from Study 2	75
5.3.	Ordered mesoporous TiO ₂ films as a model for compact TiO ₂ containing well-defined pinholes for planar heterojunction perovskite solar cells (Study 3).....	75
5.3.1.	Structural properties of the ordered mesoporous TiO ₂ thin films.....	76
5.3.2.	Shifting from 2-step sequential deposition of the perovskite to 1-step mixed ion perovskite via anti-solvent approach.....	81
5.3.3.	Device performance and discussion.....	83
5.3.4.	Conclusions from Study 3	89
6.	Conclusions	90
7.	References.....	92

Svensk sammanfattning

Perovskitsolceller är ett lovande alternativ till att framställa billig elektricitet för att uppfylla framtidens energibehov. Alla solcellstyper är dock beroende av kvaliteten på sina laddningsselektiva kontakter. Bristfälliga selektiva kontakter i en solcell betyder att de laddningsbärare som skapas genom absorption av fotoner inte kan extraheras optimalt från det absorberande materialet. De övergripande målen i denna avhandling var att systematiskt studera morfologiska defekter i det elektronselektiva kompakta TiO_2 -lagret, undersöka hur ytaktivering av det mesoporösa TiO_2 -lagret med syreplasma och UV-ljus påverkar perovskitsolcellens prestanda, samt använda TiO_2 -filmer med en ordnad porstruktur för att modellera hur kompakta elektronselektiva TiO_2 -lager med väldefinierade defekter påverkar prestandan hos plana heteroövergångsperovskitsolceller.

I avhandlingens första studie optimerades tjockleken av det kompakta elektronselektiva TiO_2 -lagret med hjälp av doppbeläggningsmetoden för att minimera en potentiell blottläggning av elektriskt ledande fluordopade tennoxid-kristaller genom TiO_2 -lagret, dvs. "småhål" (*eng. pinholes*). När det elektronselektiva lagret (ESL) inte är tillräckligt tjockt för att helt täcka den grova FTO-ytan, är det sannolikt att parallella shunt-vägar uppkommer. Detta problem löstes genom att optimera koncentrationen av utgångsmaterialet (dvs. TiCl_4) i doppningssolen. En TiO_2 -filmtjocklek på 30 nm visade sig vara optimalt för ett välfungerande kompakt ESL-lager i perovskitsolceller. Doppbeläggningsmetoden kan anses vara ett steg emot en skalbar framställning av enhetliga tunnfilmer för användning i perovskitsolceller.

Vanligtvis beläggs det kompakta TiO_2 -lagret med ett mesoskopiskt nanopartikel-baserat TiO_2 -lager i konventionellt strukturerade perovskitsolceller. I avhandlingens andra studie aktiverades ytan på dylika mesoskopiska TiO_2 -lager antingen med plasmabehandling eller med UV-ljus för att förbättra ytans vätnings. De olika ytaktiveringsmetoderna påverkade sammansättningen av det ljusabsorberande perovskitmaterialet samt morfologin på dess täcksikt, vilket följaktligen ledde till märkbara förändringar i solcellens prestanda.

Vidare framställdes även mesoporösa TiO_2 -tunnfilmer med en ordnad porstruktur genom att använda blocksampolymerer som templat i samband med doppbeläggningsmetoden. Dessa porösa filmer visade sig var användbara för att modellera effekten av småhål i kompakta TiO_2 -ESL. I avhandlingens tredje studie undersöktes om dessa "avsiktligt införda" småhål i det kompakta TiO_2 -lagret påverkade prestandan hos plana heteroövergångsperovskitsolceller. TiO_2 -filmernas porositet ökades för att simulera en ökning av de införda småhålen. Ökningen i porositet hade en förvånansvärt liten påverkan på solcellens prestanda. En ökad porositet ledde till att kortslutningsströmmarna ökade en aning medan den öppna kretsspänningen minskade, vilket innebar att solcellernas helhetseffektivitet bibehölls. Däremot minskade reproducerbarheten av solcellernas prestanda märkbart när tjockleken på de porösa filmerna minskades till 20 nm. Studien tyder på att smala småhål inte påverkar solcellens prestanda negativt förutsatt att tjockleken på TiO_2 -lagret överskrider en viss kritisk gräns.

Ett viktigt resultat från detta arbete är att ultratunna kompakta TiO_2 -filmer innehåller småhål, som kan detekteras med hjälp av röntgenfotoelektronspektroskopi. Förutom att småhålen i det kompakta TiO_2 -lagret försämrar solcellens prestanda, leder de också till att det bildas s-formade böjningar i det negativa spänningsområdet i ström-spänningskurvorna. En annan slutsats var att ytråheten på det underliggande ledande substratet påverkar kvaliteten på det kompakta TiO_2 -lagret. Jämnare substrat förutspås bli helt täckta av tunna kompakta TiO_2 -lager utan att det bildas småhål. Småhål kan även

förekomma i tjockare kompakta TiO_2 -lager (pga. av mikrobubblor eller otillräcklig vätning av det underliggande ledande substratet), men dessa påverkar inte solcellens prestanda märkbart eftersom perovskitstrukturen inte kan bilda ett sammanlänkat nätverk igenom de smala defekterna ner till det ledande substratet. Ett annat viktigt utfall var insikten i att processeringsparametrarna i solcellsframställningen måste noggrant kontrolleras för att kunna undvika potentiella reproducerbarhetsproblem. Dessa processeringsparametrar innefattar bl.a. ytaktiveringsprotokoll, behandlingstider, samt förvarings- och hanteringsbetingelser.

Abstract

Perovskite solar cells (PSCs) is a promising photovoltaic technology for low-cost electricity generation to fulfill future demands. However, the success of any photovoltaic device is highly dependent on the quality of its selective contacts. Having poor selective contacts in a solar cell implies inappropriate extraction of photo-generated charge carriers in the absorbing material upon illumination. The overall aim of this research thesis was to systematically study three different aspects of the TiO_2 electron-selective layer (ESL) used in PSCs: First, to optimize the thickness of the compact TiO_2 layer in order to rule out the possibility of any morphological defects such as pinholes. Second, to activate the surface of the subsequent mesoscopic TiO_2 layer using oxygen plasma and UV light, and to investigate its influence on the performance of mesoscopic PSCs. Third, to use block co-polymer-templated ordered mesoporous TiO_2 films to model compact TiO_2 ESLs containing well-defined pinholes and to study the influence of these “induced” pinholes on the performance of planar heterojunction PSCs.

In the first study of this thesis, the thickness of dip-coated compact TiO_2 electron-selective layers (ESLs) was optimized to minimize possible exposure of conductive FTO (fluorine-doped tin oxide) crystals through the ESL (also termed pinholes). The dip coating method was employed as a step towards scalable and uniform thin films for PSCs. When the ESL is not thick enough due to insufficient amount of precursor available to cover the entire rough FTO surface, parallel shunt pathways are likely to form between the perovskite and the underlying FTO. This problem was solved by optimizing the TiCl_4 precursor concentration in the sol. A 30 nm thick compact TiO_2 layer was found to perform optimally in PSCs. With further increase in thickness of the compact TiO_2 layer, the device performance remains nearly the same. However, if the layer is too thick, it can potentially reduce the device performance due to increased resistance or increased light absorption by the compact TiO_2 layer.

A mesoscopic nanoparticle-based TiO_2 scaffold layer is generally coated on the top of the compact TiO_2 layer in conventionally structured PSCs. In the second study of this thesis, the surface of such mesoscopic TiO_2 layers was activated by oxygen plasma or UV light to enhance the wettability of the nanostructured layer. The different surface activation methods were found to significantly influence the composition of perovskite light absorber and the morphology of its capping layer, which subsequently manifested in changes in the device performance. Oxygen plasma treatment of the nanostructured layer resulted in the activation of both the exterior and interior surfaces of the scaffold, which subsequently resulted in a dense crystallization of the lead iodide (PbI_2) precursor within the nanostructure. This significantly reduced its conversion to perovskite upon its reaction with methylammonium iodide. On the other hand, exposure to UV light only activates the top-most surface of the scaffold. Thus, in this case the PbI_2 crystallized sparsely within the nanostructure similarly as when no surface activation is performed. Therefore, its conversion to perovskite was still quite efficient. The poor conversion of the plasma-treated sample resulted in a 25% reduction in the device performance in comparison to devices prepared without any surface activation. On the other hand, the performance of devices prepared on top of UV-treated mesostructured TiO_2 was found to be improved by 20% in comparison to non-treated samples.

Furthermore, ordered mesoporous TiO_2 thin films were prepared by di-block copolymer templating in combination with dip coating. These films turned out to be useful for modelling pinholes in compact TiO_2 ESLs. Therefore, in the third study, planar heterojunction PSCs were prepared to investigate if these “intentionally-induced” pinholes in the compact TiO_2 layers pose any threat to the device performance. The porosity of the TiO_2 films was increased to simulate the increase in density of so-

called “induced” pinholes. Surprisingly, the increase in porosity had a very small influence on the device performance. The short-circuit currents were found to slightly increase with a decrease in the open-circuit voltage; thus, the overall power conversion efficiencies remained nearly the same. However, the reproducibility of the device performance was found to be strongly reduced when the thickness of TiO_2 films (with highest porosity) was lowered down to 20 nm. This study suggests that the presence of narrow pinholes do not adversely affect the device performance provided that the thickness of the TiO_2 layer exceeds a certain critical limit.

An important finding from this work was that ultrathin compact TiO_2 films possess pinholes, which can be detected by X-ray photoelectron spectroscopy. The pinholes in the compact TiO_2 layer not only reduce the device performance but also cause the formation of s-shaped kinks in the negative voltage regime of the current-voltage curves. Another conclusion was that the roughness of the underlying conductive substrate influences the quality of the compact TiO_2 layer. Smoother substrates are expected to be completely covered by thin compact TiO_2 layers without the formation of pinholes. There is still a possibility of pinholes in thicker compact TiO_2 films (due to microbubble formation or improper wettability of the underlying conductive substrate), but they do not significantly reduce the device performance since the perovskite is not able to form interconnected networks throughout the narrow defects down to the underlying conductive substrate. Another important learning outcome was the knowledge that the processing parameters for device fabrication must be carefully controlled to avoid potential reproducibility issues. Such processing parameters include surface activation protocols, treatment times, and storage and handling conditions.

List of abbreviations

AFM	Atomic force microscopy
ALD	Atomic layer deposition
CdTe	Cadmium telluride
CIGS	Copper indium gallium diselenide
c-TiO ₂	Compact titanium dioxide
CZTS	Copper zinc tin sulfide
DSSC	Dye-sensitized solar cells
EISA	Evaporation-induced self-assembly
ESL	Electron-selective layer
EtOH	Ethanol
FF	Fill factor
FTO	Fluorine-doped tin oxide
GaAs	Gallium arsenide
GI-angle	Grazing incidence angle
GI-XRD	Grazing incidence x-ray diffraction
HSL	Hole-selective layer
ITO	Indium doped tin oxide
J _{sc}	Short-circuit current density
Li-TFSI	Lithium bis(trifluoromethanesulfonyl)imide
MAPbI ₃	Methylammonium lead iodide
MIS-CELIV	Metal-insulator-semiconductor charge extraction linear voltage
mp-TiO ₂	Mesoporous titanium dioxide
OPV	Organic photovoltaics
PCE	Power conversion efficiency
PSC	Perovskite solar cells
QDPV	Quantum dot photovoltaics
SEM	Scanning electron microscopy
S _R	Surface recombination velocity
SSPL	Steady-state photoluminescence
TCO	Transparent conductive oxide
THF	Tetra hydrofuran
TRPL	Time-resolved photoluminescence
UV-Vis	Ultraviolet-visible spectroscopy
V _{oc}	Open-circuit voltage
XPS	X-ray photoelectron spectroscopy
XRR	X-ray reflectometry

List of publications

1. **M. T. Masood**, C. Weinberger, J. Sarfraz, E. Rosqvist, S. Sandén, O. J. Sandberg, P. Vivo, G. Hashmi, P. D. Lund, R. Österbacka, and J-H. Smått, *Impact of Film Thickness of Ultrathin Dip-Coated Compact TiO₂ Layers on the Performance of Mesoscopic Perovskite Solar Cells*. ACS Applied Materials & Interfaces, 9, 2017, 17906-17913. (DOI: 10.1021/acsami.7b02868)
2. **M. T. Masood**, C. Weinberger, S. Qudsia, E. Rosqvist, O. J. Sandberg, M. Nyman, S. Sandén, P. Vivo, K. Aitola, P. D. Lund, R. Österbacka, J-H. Smått, *Influence of titanium dioxide surface activation on the performance of mesoscopic perovskite solar cells*. Thin Solid Films, 686, 2019, 137418. (DOI:10.1016/j.tsf.2019.137418)
3. **M. T. Masood**, S. Qudsia, M. Hadadian, C. Weinberger, M. Nyman, C. Ahläng, S. Dahlström, M. Liu, P. Vivo, R. Österbacka, J-H. Smått, *Investigation of Well-Defined Pinholes in TiO₂ Electron Selective Layers Used in Planar Heterojunction Perovskite Solar Cells*, Nanomaterials, 10, 2020, 181 (Open access, DOI:10.3390/nano10010181)

Supporting publication

- S1. P. Vivo, A. Ojanperä, J-H. Smått, S. Sandén, S. G. Hashmi, K. Kaunisto, P. Ihalainen, **M. T. Masood**, R. Österbacka, P. D. Lund, H. Lemmetyinen, *Influence of TiO₂ Compact Layer Precursor on the Performance of Perovskite Solar Cells*, Organic Electronics, 41, 2017, 287-293. (DOI:10.1016/j.orgel.2016.11.017)

Contribution of the author

Study 1: The author was responsible for the preparation of dip coating solutions and all the TiO₂ thin film samples. The author prepared lab-scale perovskite solar cells from some of the compact TiO₂-coated FTO substrates, while the others were sent for characterization. He designed the mask and therefore the dimensions of gold metal electrodes. He was responsible to measure J-V curves under illumination and analyse the data to determine the relative device performance. He also performed time-dependent current measurement for the best device at the maximum power point voltage. He also actively participated in writing the first draft of the manuscript.

Study 2: The author was involved in the conceptualization and was responsible for samples and device preparation. He performed the surface activation with oxygen plasma and UV light treatment on mesoporous TiO₂ films coated on top of glass/FTO/c-TiO₂ substrates. Thereafter he deposited the perovskite via two-step sequential deposition method. He performed the UV-vis measurements on the samples. He performed surface activation on the dye loaded mesoporous TiO₂ samples (by oxygen plasma and UV-light). Thereafter he performed the UV-vis to qualitatively correlate the depth of dye degradation with the type of surface activation. He prepared the lab scale devices and performed the dark and light J-V measurements to determine the device performance. He also performed the maximum power point measurements and wrote the first draft of the manuscript.

Study 3: The author was involved in the conceptualization and was responsible for samples and device preparation. He performed the UV-vis measurements on perovskite/TiO₂/Glass substrates. The author performed the dark and light J-V measurements and analysed the data. He also performed the maximum power point measurements and wrote the first draft of the manuscript.

1. Introduction and outline

Solar energy is a natural and abundant form of energy that can be converted into electrical energy by the use of a photovoltaic device (i.e., a solar cell). The use of solar cells for electricity generation is also environmentally friendly because they do not generate carbon emissions like the use of fossil fuels, which have already disturbed the ecosystem of our planet. This technology has a huge potential to fulfill our daily electricity requirements in a more economical and practical way compared to the electricity generation by power plants, which are technically dependent on huge infrastructure, high-tension cables, and are subject to frequent maintenance. The electricity generated from solar cells can be used for both small-scale domestic and large-scale industrial use. Many economies are highly agriculture-dependent where solar-powered tube wells are widely used for irrigating large areas of agricultural lands. Thus, electricity shortages and high cost of fossil fuels can be counteracted in remote areas by the use of efficient solar cells.¹

The photovoltaic technology was introduced in 1954 and was then based on crystalline silicon.² Even if more than 60 years have passed, crystalline silicon photovoltaics are still considered a reliable and mature technology in comparison to other types of solar cells. The demand of solar energy has increased exponentially in many countries, but the high cost of silicon is the reason for the limited use of silicon solar cells. This is because the fabrication of crystalline silicon is highly energy and labour intensive. Furthermore, as crystalline silicon is an indirect band gap semiconductor material, silicon solar cells cannot be manufactured in the form of thin films, which would reduce their manufacturing cost substantially.

Several emerging thin film photovoltaic technologies are at the research stage today. Out of them, perovskite solar cells (PSCs) are likely to reach the standard level of crystalline silicon solar cells. Organo-lead halide perovskites are direct band gap semiconductors with extraordinarily high charge carrier mobilities and diffusion lengths. The possibility to manufacture PSCs on a large-scale would make the technology highly cost-effective. This is because PSCs can be processed from solutions and at low temperatures, which also enables the use of flexible substrates. However, the technology still have some challenges to overcome, such as the poor long-term stability due to vulnerability against high humidity, and toxicity due to the presence of lead.

In a typical thin film photovoltaic device, efficient collection of photo-generated charge carriers is of utmost importance. The organo-lead halide perovskite can produce a high density of free charge carriers upon illumination, which must be efficiently extracted from the active layer. For this purpose, charge-selective contacts are required, which can selectively extract charges of one type of polarity while they block the charges of opposite polarity. In other words, electron-selective layers (ESLs) selectively extract photo-generated electrons, while hole-selective layers (HSLs) selectively extract photo-generated holes.

TiO₂ is considered to be one of the most suitable option as ESL material besides SnO₂ and ZnO. This is because its electron affinities are well aligned with the conduction band minima of organo-lead halide perovskites. However, since TiO₂ is a transition metal oxide, there can be slight variations in its energy levels and work functions, which are subject to change with the processing conditions.³ TiO₂ is known to be chemically stable, solution-processable, and a cheap ESL material for PSCs.

In this thesis, various aspects of compact and mesoporous TiO_2 photo-electrodes were studied for their use in PSCs. The compact TiO_2 layer is a dense film of TiO_2 which isolates the under lying transparent conductive oxide (TCO) substrate from the subsequent perovskite photo-active layer. The mesoporous TiO_2 layer helps to crystallize the perovskite and also increase the area of the perovskite/ TiO_2 interface to ensure efficient extraction of the photo-generated electrons from the perovskite. The thickness of the compact TiO_2 layer was first optimized in order to minimize the presence of potential morphological defects such as pinholes. In this case, pinholes can be defined as exposed regions of the transparent conductive oxide (TCO) layer through the compact ESL, and tend to significantly reduce the charge extraction efficiency due to excessive surface recombination owing to a direct contact between the perovskite and the underlying TCO. Such pinholes are generally encountered in ultrathin compact ESL films due to incomplete coverage of the rough underlying conductive substrate.

In the second study, mesoporous TiO_2 electron-selective layers were subjected to different surface activation protocols to enhance the wettability of the porous film structure prior to the deposition of perovskite active layer (via the two-step sequential deposition route). The enhanced wettability was expected to improve the interfacial contact between the perovskite and the TiO_2 ESL (i.e., increase the extraction efficiency of photo-generated electrons at the interface). However, the perovskite crystal formation, its composition and capping layer morphology were found to be directly influenced by different surface activation protocols, which ultimately affected the performance of the photovoltaic devices.

Furthermore, ordered mesoporous TiO_2 layers were used as mesoscopic scaffolds and were compared to TiO_2 nanoparticle-based mesoscopic scaffolds in terms of the solar cell performance. The ordered mesoporous TiO_2 thin films were later used as a model system for compact TiO_2 layers containing narrow pinholes in planar heterojunction PSCs. These so-called *induced* pinholes were found to be detrimental to the device performance only if the TiO_2 layer was thin enough to allow the perovskite to form direct shunt pathways through the ESL down to the underlying conductive substrate.

2. Background and literature review

2.1. The sunlight as an infinite source of energy

The Sun is the star at the heart of our solar system, which is nearly a perfect sphere⁴ and made up of hot plasma.⁵ It gives off electromagnetic radiation comprising ultraviolet, visible and infrared light called the sunlight. Some high energy radiation such as gamma rays are also emitted from the Sun's core as a result of nuclear fusion processes, but then the internal absorption and thermalization converts these high energy photons into low energy photons before they exit the Sun's surface. Therefore, such high energy radiation generally do not reach the upper part of Earth's atmosphere.

The spectrum of the solar radiation at the top of Earth's atmosphere is quite similar to that of a black body at a temperature of about 5250 °C⁶ as shown in Figure 1. The Sun's electromagnetic radiation is the primary source of energy that can be utilized on Earth. The upper level of Earth's atmosphere receives an average power density of about 1.366 kW/m². A large part of this solar energy is absorbed and scattered by the Earth's atmospheric gases such as O₂, O₃, H₂O and CO₂, and thus the value of the average power density comes down to ~1 kW/m² at Earth's sea level. This filtration of solar radiation is even more significant for the UV and IR parts of the spectrum. The fluctuation in average power density is considerably affected by the geographical and climatic variations. Figure 1 shows variations in solar radiation spectrum at the top of Earth's atmosphere and at the sea level. The spectrum shows that the highest intensity of the incoming radiation lies within the visible range, i.e., between 400 to 750 nm.⁷

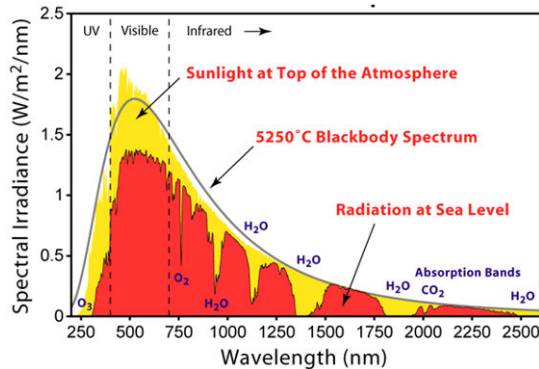


Fig 1. Solar radiation spectrum perpendicular to the Earth's surface.⁶

Though there are variations in the power density, solar energy is one of the well-distributed form of energy resources across the globe. There are clearly some regions in the world which are more advantageous for the solar energy utilization. Such regions are highlighted in red in Figure 2. The black spots in the figure identify the areas which possess the highest potential to utilize the energy from sunlight to meet the global requirement. It is not possible to find such an abundant availability of any other form of energy resource, including fossil fuels. The main challenge behind the optimal utilization of solar energy is not its availability, but how to efficiently convert it into other forms of useful energy.

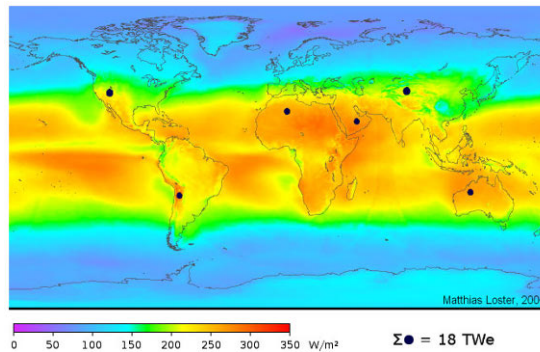


Fig 2. Global average solar irradiance. Areas in red possess higher share of solar energy on average. The black spots highlight the areas which receive enough solar energy which can potentially fulfil the global energy requirement.⁸

One of the most common usage of solar energy is seen in solar photovoltaics (PV) to generate electricity for daily use. Currently, the electricity for domestic and industrial use is generally produced by various types of power plants (e.g., coal, nuclear, hydro and wind) and transported via huge grid systems. However, the PV technology guarantees unlimited electricity from the Sun and it can be utilized even in remote areas where electricity supply from grid systems is highly challenging. On the other hand, photovoltaic modules can be assembled into photovoltaic power stations (or solar farms) to supply merchant power into electricity grids. Solar cells are also scalable because, theoretically, small area photovoltaic devices are not less efficient than larger ones. This is unlike other technologies such as wind turbines or generators, which lose their efficiency with decreasing size.⁹

2.2. Electricity generation from solar light

The conversion of solar energy (sunlight) to electrical energy is called the photovoltaic effect. The process is initiated by the absorption of a solar photon by a low-band gap semiconductor called a photoactive material. A photon with an energy greater than the active material's band gap excites an electron in its occupied valence band to its unoccupied conduction band. A hole (which is a charge carrier with an opposite polarity to that of an electron) is left behind in the valence band. The generation of electron-hole pairs is followed by their subsequent transportation towards the selective contacts for extraction.¹⁰ The charge transportation towards the selective contacts takes place under the influence of an internal electric field of the photovoltaic device called the built-in voltage. The electrons and holes must be extracted at the separate contacts, which are inherently selective for a charge carrier of one polarity, while they block the charge of the opposite polarity. These steps occur in all types of photovoltaic devices with some deviations in organic solar cells where the electron-hole pairs initially exist in the form of tightly bonded excitons,¹⁰ which must be separated quickly to avoid geminate recombination to ensure efficient extraction at the selective contacts.

Narrow band gap photoactive materials are usually preferred for photovoltaic applications because they typically absorb photons in the ultraviolet-visible (UV-vis) range^{10, 11} which comprises the largest portion of the solar spectrum close to Earth's surface (see Figure 1). The dimensions of any photovoltaic device are highly dependent on the light absorbing and charge transport properties of the active material. The active part in the device should be thick enough for efficient light harvesting, while it should be thin enough to prevent excessive electron-hole recombination within its bulk.

2.3. Types of solar cells

Solar cells can be classified based on different device features, e.g., the materials used, complexity, as well as the charge separation and collection of the device.¹² Figure 3 shows the classification of photovoltaic technologies on the basis of photoactive materials. However, it is also possible to classify photovoltaic technologies in terms of their historical evolution. In 1876, William Grylls Adams and his student observed the photovoltaic effect in solidified selenium. The efficiency of selenium solar cell was not enough to power any electrical appliance. However, they proved that a solid material could potentially change light into electricity. At the present, there are many different types of photovoltaic technologies available, including the ones shown in Figure 3. In this section, the classification of solar cells is discussed in terms of their historical evolution.

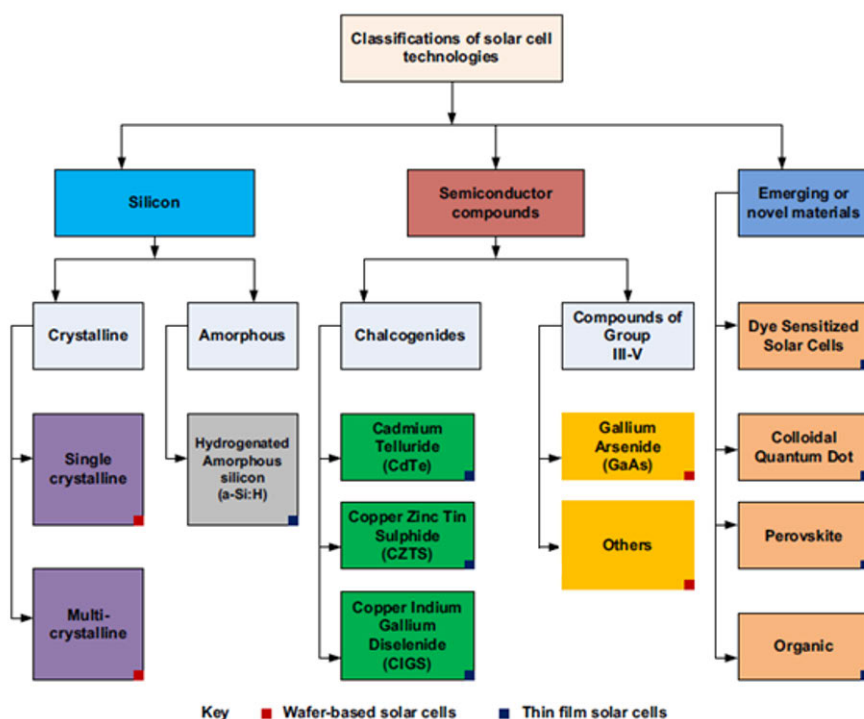


Fig. 3 Typical photovoltaic technologies classified on the basis of active material. Silicon, compound semiconductors and emerging new advanced photosensitive materials. The technologies marked as red are wafer-based photovoltaic devices while the blue ones are thin film solar cells. Both ways of classifying the solar cells are shown in this diagram.¹³

2.3.1. First generation solar cells

The photovoltaic technology was formally introduced in 1954 when Daryl Chaplin, Calvin Fuller and Gerald Pearson developed a silicon photovoltaic cell at Bell Telephone Laboratories in New Jersey.² It was prepared by using a diffused crystalline silicon p-n junction. The crystalline silicon is one of the oldest and most extensively used material in the semiconductor industry. Most of the commercially available photovoltaic modules still comprise of crystalline silicon.^{9, 14} The first generation of solar cells is proven to be technically reliable and has successfully reached market penetration.

Crystalline solar cells are further classified as **single crystalline** and **poly-crystalline** (or multi-crystalline) silicon solar cells depending upon their respective manufacturing process. The Czochralski process is typically used to manufacture single crystalline silicon. In this process a small silicon crystal is dipped into molten silicon and withdrawn with a very slow but constant speed.¹⁵ This forms cylindrical single crystal ingots, which can be later cut into wafers for further processing. Poly-crystalline silicon is manufactured by block casting of molten silicon to form a silicon slab which can then be cut into wafers. This results in the formation of randomly oriented crystalline grains.

The crystalline silicon for photovoltaic application should be highly pure and its manufacture involves energy intensive processes.¹⁶ The production of poly-crystalline silicon is relatively cheaper than single crystalline silicon. However, the performance is inferior due to the resistance posed by grain boundaries to the charge carriers.¹⁷ The best performing single crystalline and poly-crystalline silicon solar cells to date are reported to be 27.6% and 23.3% efficient, respectively.¹⁸ Crystalline silicon is an indirect band gap semiconductor, hence it is used in the form of relatively thick wafers to optimally absorb the sunlight. These wafers are fragile in nature and must therefore be carefully handled during transportation and installation. Therefore, crystalline silicon cannot be utilized in thin film and flexible solar cells.¹⁹

Gallium arsenide (GaAs) is a compound semiconductor with a direct band gap, which ensures its strong light absorption capability and very low non-radiative energy losses. The material can be used both in the form of wafers and thin films, because its direct band gap ensures sufficient light absorption.²⁰ Thin and flexible GaAs films can be fabricated using epitaxial lift-off of crystalline films grown on rigid substrates.²¹ The highest power conversion efficiency achieved for GaAs-based thin film solar cells is 29.1%.²² However, GaAs-based solar cells require more expensive materials and manufacturing techniques, and therefore they are not manufactured in large volumes as compared to other wafer-based photovoltaic technologies.

2.3.2. Second generation solar cells

In order to simplify the manufacturing process and reduce the cost, second generation solar cells (also known as thin film solar cells) have been introduced. These typically involve the deposition of thin layers of the photoactive materials onto glass or flexible substrates. The use of photo-active thin films for photovoltaic applications requires about 1–5% of the photo-active material in comparison to the amount needed for silicon wafer-based solar cells. This consequently reduces the cost to about half in comparison to first generation solar cells.²³

The photoactive materials for second generation solar cells include amorphous silicon, cadmium telluride, and copper indium gallium diselenide (CIGS). The efficiencies of most of the second generation solar cells are above 20%, which is slightly lower than the performance of crystalline silicon solar cells. However, the efficiencies of amorphous silicon solar cells are to date not more than 14.5%, which is attributed to the presence of midgap trap states within its mobility gap.¹⁸ The possibility to deposit the thin film photo-active materials on a flexible substrate makes them less likely to be damaged during handling.

Hydrogenated amorphous silicon (a-Si:H) is a non-crystalline form of silicon and it possesses a stronger light absorption capability than crystalline silicon which can be attributed to its direct mobility gap (i.e., direct band gap). Thinner and flexible devices can be made by combining an a-Si:H absorbing

layer with nanocrystalline silicon or amorphous silicon-germanium alloys to produce tandem solar cells without the need of lattice matching.²⁴ The a-Si:H solar cells are economical and do not require very energy intensive fabrication processes.

Due to the presence of non-passivated dangling bonds in amorphous silicon, there is a significant amount of mid-gap states which cause non-radiative recombination and significantly reduce the device performance. Therefore, a-Si:H solar cells are mainly suitable for small-scale and low-power applications. Their widespread use is also limited due to problems associated with light-induced degradation.^{24, 25}

Cadmium-telluride (CdTe) is also a direct band gap semiconductor and therefore has a strong light absorption.²⁶ The power conversion efficiencies for CdTe solar cells are reported to be about 22%¹⁸ and they have the shortest energy payback time compared to other thin film photovoltaics.²⁷ Furthermore, a high production rate combined with the high efficiency leads to the lowest module cost. However, the toxicity of cadmium and scarcity of tellurium have pushed scientists to look for other alternative materials.²⁸

Copper indium gallium diselenide ($\text{CuIn}_x\text{Ga}_{(1-x)}\text{Se}_2$, CIGS) is a compound semiconductor with a direct band gap between 1.0 to 1.7 eV and a high absorption coefficient. The band gap is dependent on the stoichiometry of the compound.²⁹ Just like the CdTe films, CIGS films can be prepared by solution processing and vapor deposition methods on both rigid and flexible substrates. This makes them suitable for integrated photovoltaic applications.³⁰ CIGS solar cells are also useful in space applications due to their high radiation resistance. There are still some challenges due to variations in stoichiometry, film integrity and material defects which are created during film processing. The scarcity of elemental indium is also another problem, which limits the large-scale production of CIGS solar cells.²⁸

It is important to mention that the second generation photovoltaic solar cells do not perform better than the first generation crystalline silicon solar cells, and therefore they have only been used for small-scale applications. Furthermore, the material toxicity related to the CIGS and CdTe technologies adds to the problem and therefore, scientists have been pushed towards other alternatives highlighted in the third generation solar cells.²⁸

2.3.3. Third generation solar cells

Third generation solar cells are based on technologies which are capable to circumvent the Shockley-Queisser limit of 31% to 41% efficiencies for single band gap photovoltaics.³¹ Third generation solar cells are also known as emerging thin film photovoltaics. Though some of the new generation solar cells might not be highly efficient in terms of their performance, they can be considered alternatives to expand the solar energy utilization, such as integrating the solar panels into building facades or onto automobile surfaces.³²

Copper zinc tin sulfide ($\text{Cu}_2\text{ZnSnS}_4$, CZTS) is one of the emerging thin film photoactive materials, which is an alternative to CIGS and can be made by similar processing techniques.³³ CZTS possesses similar properties as CIGS in terms of band gap and absorption coefficient, but defects and grain boundaries pose limitations to the carrier lifetimes. Just like CIGS films, material defects and variations in film integrity and material stoichiometry is still very challenging.³⁴ Another challenge is to minimize the

formation of secondary sulfur-rich phases (such as CuS, ZnS and SnS) in the material, which are highly detrimental to the performance of a solar cell.

Organic solar cells or organic photovoltaics (OPV) involve the use of semiconducting organic polymers or organic small molecules as light absorbing active materials. These organic materials consist of abundant elements and they can be tailored for desired functionalities.³⁵ These materials can be assembled into thin films by different low-cost deposition methods, such as solution processing, inkjet printing, and thermal evaporation. Just like other thin film solar cells, these organic thin films can be deposited onto a variety of substrates and do not require high-temperature sintering.³⁶ The organic materials comprise of carbon atoms covalently bonded with alternating single and double bonds (i.e., conjugated π systems). Primarily, the length and functional groups of the organic molecules (or polymers) affect the HOMO-LUMO levels or band gap of the molecules/materials.³⁷ A wide range of organic materials for application in organic photovoltaics can be solution-processed, which renders organic photovoltaic devices to be suitable for a range of applications, like powering independent sensors due to their light weight or as disposable and/or semi-transparent solar cells.³⁸ Unfortunately, there are still many challenges which hinder their market entrance, including inefficient charge separation of tightly bonded photo-generated electron-hole pairs (excitons). This is also problematic for sufficient charge extraction and gives rise to relatively low power conversion efficiencies. Many organic photovoltaic materials also possess poor long-term stability.

Quantum dot photovoltaics (QDPV) use semiconducting inorganic nanocrystals, called quantum dots (QDs), as light absorbing active material. The band gap of a bulk semiconductor depends on the choice of material and its chemical composition, whereas the band gap of a QD can be tuned by merely changing the size of the crystal.³⁹ QDs can be grown in different sizes, which makes it easier to obtain a range of different band gaps without modifying any other parameter. This makes it possible to harvest light in the near-infrared (NIR) range, which is challenging with other photovoltaic technologies. With QDs, it is also possible to produce multi-junction cells by using a single material system.⁴⁰ The QDPV can generate multiple electron-hole pairs from single high-energy photons.⁴¹ The fabrication of QDPV is relatively simple and economical, because of the possibility to use wet-chemistry methods. Nonetheless, they are currently only produced in small batches. There are still many challenges to solve before their commercialization, which include low power conversion efficiencies as a result of low charge mobilities and low open circuit voltages. Another problem is that there is still a lack of understanding of the QD surface chemistry.⁴²

Dye-sensitized solar cells (DSSCs) is the most mature and well-developed photovoltaic technology among the emerging thin film solar cells.⁴³ A typical DSSC comprises of a nanoporous inorganic scaffold film (typically TiO_2), which is sensitized with a light-absorbing organic dye (usually ruthenium complexes). Upon illumination, the photo-generated electrons in the organic dye are injected into the inorganic scaffold and extracted at a transparent conductive electrode (TCO). The organic dye is regenerated by using a liquid electrolyte, which transports ions to the counter electrode.⁴⁴ The DSSC technology has achieved record efficiencies up to 14 %⁴⁵ and it benefits from low-cost material and simple fabrication methods with a possibility of flexible modules. A major obstacle prohibiting their vast daily usage includes their limited long-term stability under illumination and high temperatures. However, issues related to long-term stability due to poor sealing of the cell can be minimized by replacing the liquid electrolyte with solid hole transport layers.⁴⁶ The DSSCs also suffer from low

absorption in the near infrared range (NIR) and low open circuit voltages due to interfacial recombination.⁴⁷

Among the third generation solar cells, **perovskite solar cells (PSCs)** are the most widely studied solar cells during the last decade. The first PSC was reported as a dye-sensitized solar cell in 2009, where organic-lead halide perovskite nanocrystals were used as sensitizer within the TiO₂ nanostructured photo-electrode. Now PSCs is recognized as a separate photovoltaic technology and is considered to be the most promising of the emerging thin film solar cells. PSCs are considered to be able to meet future energy demands, not only because of high efficiencies, but also because of the low raw material and manufacturing costs. A 500 nm-thin perovskite material is capable to absorb almost the entire visible part of the solar spectrum. The PSCs are also lightweight and suitable for flexible solar modules. Despite many positive features of PSCs, there are still some obstacles to be addressed before PSCs can be commercialized to full extent, including device reproducibility,⁴⁸ scalability,⁴⁹ and stability.⁵⁰ A more detailed review on PSCs is given in the following chapter.

2.4. Perovskite solar cells

PSCs are considered to be the most promising of the emerging thin film solar cells and their efficiencies are soon expected to compete with the efficiencies of conventional silicon-based photovoltaics. The first PSC had an efficiency of 3.8%⁵¹ (then considered as a DSSC). Within a decade, the device performance of PSCs has skyrocketed up to 25.2 %.¹⁸ Efforts are currently being made to commercialize this technology⁵² because it offers low-cost solar energy conversion due to the ease in fabrication and the possibility to make devices on top of glass or flexible substrates.^{53, 54}

2.4.1. Working principle of a PSC

PSCs work on the basis of the excellent light harvesting characteristics of the organo-lead-halide perovskite light absorbing material, which acts as the active layer in the device. The perovskite is sandwiched between an electron-selective layer (ESL) and a hole-selective layer (HSL). Electron-hole pairs are generated in the perovskite layer upon illumination with light. Electrons are selectively extracted by the ESL (such as TiO₂) and transported to an external circuit via a transparent conductive oxide (TCO) such as fluorine-doped tin oxide (FTO). On the other hand, holes are selectively extracted by the HSL (such as lithium-doped Spiro-OMeTAD). This is briefly explained in Figure 4a where TiO₂ is shown as an ESL. This device architecture is known as planar heterojunction PSC. The introduction of a mesoscopic TiO₂ layer on top of the compact TiO₂ layer increases the perovskite/TiO₂ interfacial contact area. The mesoscopic layer also provides a large number of nucleation sites for the perovskite crystallization. This architecture is shown in Figure 4b. In the presence of a mesoscopic layer, the electrons are primarily injected into TiO₂ nanostructure and subsequently into the compact TiO₂ layer.⁵⁵ The planar heterojunction architecture is generally reported to give lower power conversion efficiencies (PCEs) and higher hysteresis in the J-V curves in comparison to mesoscopic PSCs when TiO₂ is used as ESL.⁵⁶ However, there are some exceptional cases⁵⁷ where the active layer fabrication method, such as vapor-assisted perovskite deposition, render high device performance for planar heterojunction PSCs. Some technical differences between planar vs mesoscopic PSCs will be discussed in section 2.4.2.

Figure 4c further illustrates the working principle of PSCs in terms of band energy alignments between the different layers in a typical PSC. The absorption of light by the perovskite layer results in the excitation of electrons from the valence band to the conduction band leaving behind positively charged

holes (also known as the vacant electron positions) in the valence band of the perovskite. Since the conduction band minimum of the perovskite is higher than that of ESL (such as TiO_2 in this case), the electrons can be injected into the conduction band of the ESL. A higher conduction band minimum of the ESL relative to that of the perovskite results in an electron injection barrier, which can potentially result in a significant decrease in the internal quantum efficiency (IQE) of the device. The ESL can also be termed as a hole blocking layer because it does not allow hole extraction from the perovskite due to its high ionization energy (or valence band maximum) relative to that of the perovskite. On the other hand, the valence band maximum of the perovskite is lower than the HOMO level (highest occupied molecular orbital) of the HTM. Therefore, the holes from the valence band of the perovskite are injected into the valence band of the HTM. Thus, the organo-lead halide perovskite shows an ambipolar nature due to its good conductivity of both types of charge carriers in combination with high diffusion lengths.^{58, 59} Contrary to this, an ESL should ideally be an n-type semiconductor (in which electrons are the majority carriers) while the HSL should be a p-type semiconducting material (in which holes are the majority carrier). However, the charge-selectivity of the respective contacts primarily depends on the relative positions of their energy levels with respect to those of the perovskite layer at the interface. This is a fundamental requirement for all heterostructured photovoltaic devices, though it is not a hard and fast rule.¹² For example MoO_3 is strongly an n-type semiconductor due to the presence of oxygen vacancies. However, it is used to selectively extract holes in organic photovoltaic devices due to the presence of large interfacial dipoles.^{60, 61, 62}

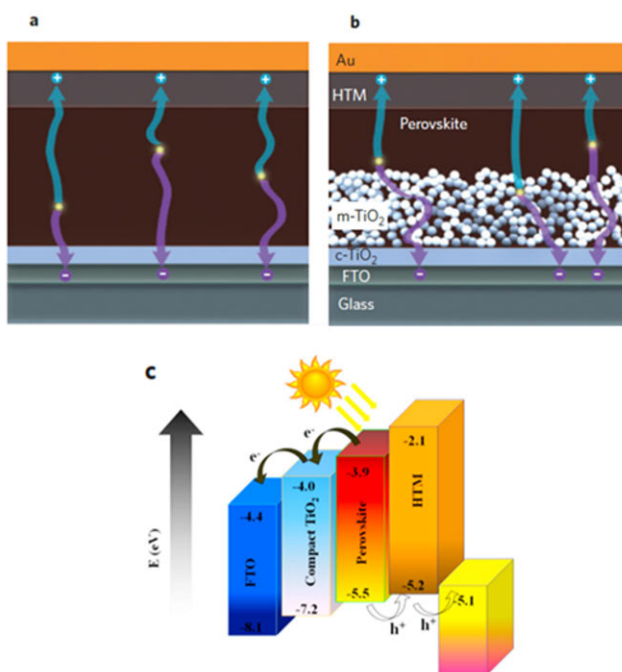


Fig 4: Schematic of (a) planar heterojunction architecture for PSCs with TiO_2 as an ESL, (b) mesoscopic PSCs with TiO_2 nanoparticle-based scaffold layer⁶³ on top of the compact TiO_2 layer. (c) Energy levels explaining the charge injection from the perovskite to their respective contacts⁶⁴ (electrons to compact TiO_2 and holes to HTM).

2.4.2. Structural evolution of the perovskite solar cell

PSCs have evolved from dye-sensitized solar cells (DSSCs) when Kojima et al⁵¹ first used 3D perovskite as an inorganic sensitizer (instead of a molecular dye) with a 3.9% PCE. Thereafter Park et al⁶⁵ reported a 6.5% device efficiency by introducing $\text{CH}_3\text{NH}_3\text{PbI}_3$ quantum dots on top of TiO_2 nanocrystals, which were surrounded by a redox electrolyte (Figure 5a). Organometallic lead halide perovskites are ionic compounds and therefore they quickly dissolve in polar solvents such as the electrolytes used in DSSCs. This not only adversely affects the device performance, but also the long-term stability. This problem was solved by replacing the redox liquid electrolyte with a solid hole transport material (Spiro-OMeTAD) (Figure 5 (b)).⁶⁶ This more stable PSC was reported to have 9.7% efficiency. Snaith et al⁶⁷ proposed a non-sensitization-type PSC, in which mixed halide perovskite-coated Al_2O_3 nanoparticles demonstrated a 10.9% PCE. The device performance was slightly better because the insulating Al_2O_3 nanoparticles allowed the electrons to reside within perovskite until they were extracted at the TiO_2 contact. This implies that the PSC can perform efficiently even in the absence of a mesoporous TiO_2 layer. Heo et al⁶⁸ infiltrated the mesoporous TiO_2 completely with perovskite to form a capping layer, which would subsequently isolate the nanostructured TiO_2 from the HSL. The device successfully demonstrated an improved performance of 12 % PCE (see Figure 5 (d)). A 15 % PCE was later achieved with the same device architecture when the perovskite was fabricated via a 2-step sequential deposition method. PbI_2 was deposited by spin coating followed by dipping the coated substrate into methylammoniumiodide solution.⁶⁹ Snaith et al⁷⁰ prepared a planar heterojunction PSC in which the perovskite layer was directly deposited on top of the compact TiO_2 layer by vapor deposition (Figure 5 (e)). In this case, a PCE of 15 % was successfully achieved without the need of a nanostructured layer to assist in the perovskite crystal growth.

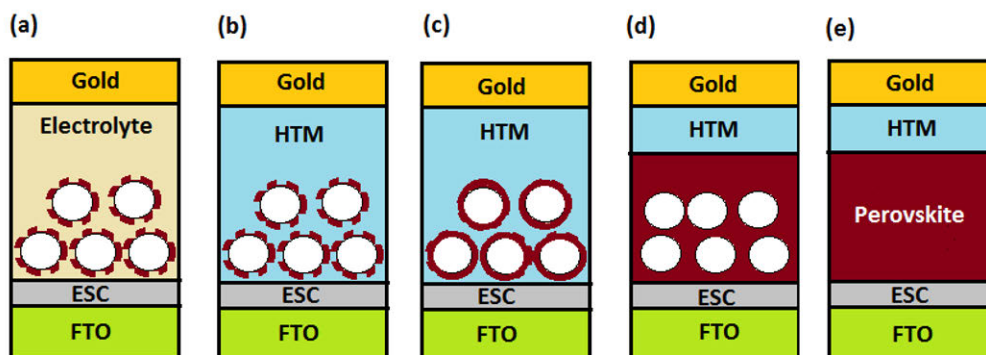


Fig 5: Evolution of the perovskite solar cell: (a) Sensitization with perovskite quantum dots on top of a TiO_2 structure surrounded by liquid electrolyte, (b) quantum dots and solid hole transport material, (c) perovskite coated on TiO_2 or non-conducting Al_2O_3 nanoparticles (scaffold), (d) TiO_2 scaffold infiltrated with perovskite and a thick capping layer of perovskite on top of the scaffold, (e) planar heterojunction perovskite solar cell (no scaffold). (Modified diagram from Park et al⁷¹)

The rapid progress in organic-inorganic lead halide perovskite is owing to the material's outstanding properties such as the direct and tunable band gap (between 1.5 and 1.6 eV,^{72, 73} ambipolar charge carrier transport properties,^{68, 74} high absorption coefficient,⁷⁵ high charge carrier mobilities,^{72, 76} low exciton binding energy (of about 10-50 meV)⁷⁷ which results in longer carrier diffusion lengths (100 nm to 1 μm),^{58, 59} long carrier lifetime,^{78, 79} and solution processability.^{80, 81} Therefore, it is worth discussing

some basic features about organo-lead halide perovskite material before moving on to the charge selective layers.

2.4.3. Organo-lead halide perovskite as a photoactive material

Named after a Russian mineralogist and statesman, Len Alexeyevich Perovski, perovskite is known as a crystal structure which is defined as a family of compounds with an ABX_3 chemical formula (where X is oxygen or a halogen anion). The perovskite crystal structure is based on corner sharing of eight $[BX_6]$ octahedras with the A cations occupying the cavity in the center (see Figure 6). The most commonly studied perovskites are oxides⁸² (such as $CaTiO_3$ and $BaTiO_3$) due to high ferroelectricity and superconductivity.⁷¹

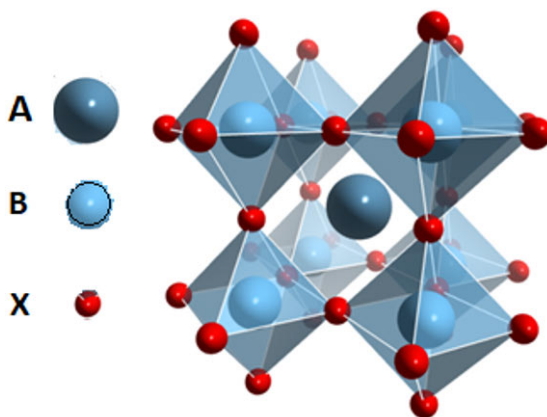


Fig 6: The structure of perovskite with ABX_3 general formula. Eight $[BX_6]$ octahedras surround the A site cation.⁸³

Halide perovskites received little attention until layered organometallic lead halide perovskites were found to exhibit a decrease in their band gap with increased dimensionality from 2D to 3D.⁸⁴ In hybrid organic-inorganic perovskites, one of the key building blocks of the perovskite is replaced with an organic molecular anion or a cation.^{85, 86} There are many such compounds which also include perovskites which comprise of both organic cations and anions.^{87, 88} One of the most commonly studied perovskites for optoelectronic applications is methylammoniumlead halide. In this perovskite, the organic methylammonium cation ($CH_3NH_3^+$) is surrounded by eight $[PbX_6]$ octahedras where X is the halide anion. The first methylammoniumlead iodide perovskite was synthesized in 1978 by Weber et al.⁸⁹ However, it was not until 2009 before this material was first tested as a sensitizer in photovoltaic applications.⁵¹

On the basis of the number of different A site cations, organo-lead halide perovskites can be classified as single cation (where A = Methylammonium (MA^+), $CH_3NH_3^+$ ^{69, 90, 91, 92} or Formamidium (FA^+) $CH(NH_2)_2^+$ or Cs^+ ,⁹³ double cation (A = MA^+ and FA^+ ⁹⁴ or MA^+ and Cs^+ ,⁹⁵ or triple cation (where A = FA^+ , MA^+ and Cs^+)^{96, 97} perovskites. The compositional engineering of the A site cation significantly influences different properties of the perovskite material. First of all, it affects the crystal geometry of the perovskite. The pioneering work on the effect of ionic size upon the crystal geometry of the perovskite was performed by Victor Moritz Goldschmidt in 1926⁹⁸ in which he proposed that by determining the tolerance factor (t) of the perovskite, one can estimate the crystallographic geometry

of the perovskite crystal (or in other words, its degree of distortion). In ideal cubic perovskites, the lattice parameter a can be described according to the following equation:

$$a = \sqrt{2}(r_A + r_X) = 2(r_B + r_X) \quad (1)$$

The Goldschmidt tolerance factor (t) of the perovskite crystal can be described according to the following equation which assumes that the bonding is purely ionic:

$$t = \frac{(r_A + r_X)}{\sqrt{2}(r_B + r_X)} \quad (2)$$

r_A , r_B and r_X stand for the ionic radii of the A site cation (surrounded by the eight octahedras), the B site cation (which is in the middle of the octahedras), and the X anion, respectively (see Figure 6). Ideal cubic perovskites such as SrTiO_3 has a t equal to 1. The size of A site cation crucially affects the tolerance factor. The smaller the size of the A cation, the lower is the value of t and therefore the $[\text{BX}_6]$ octahedras tilt to fill the space, which directly influences the crystal geometry. Generally, a perovskite having a tolerance factor between 0.9 and 1.0 is said to have an ideal cubic structure. With tolerance factors between 0.71 and 0.9, the perovskite is slightly distorted due to the tilted octahedras. Non-perovskite structures are formed with tolerance factors below 0.71 and above 1.0. Perovskites with t values greater than 1 generally have a hexagonal crystal structure.⁸²

The abovementioned trends in crystal geometry as a function of the tolerance factor were found for oxide perovskites. However, the rule is still valid for hybrid organic-inorganic lead halide perovskites.⁹⁹ It is also common that the crystal structure of a certain perovskite material varies depending on the temperature. For example, MAPbI_3 has a tolerance factor of 0.91 but it is tetragonal and not ideally cubic at room temperature. The tetragonal distortion parameter is greater than unity (i.e. $c/2a = 1.01$) at 300 K, due to the elongation of $[\text{PbI}_6]$ octahedras along the c -axis. With an increase in temperature above 57 °C, it is converted into cubic perovskite. However, the tetragonal MAPbI_3 is still a photo-active phase at room temperature and it is one of the most widely reported active materials used in PSCs with sufficiently good PCEs. Single cation FAPbI_3 has a tolerance factor above 1. Thus, it has a hexagonal crystal structure at room temperature, which is a yellow non-photoactive phase. CsPbI_3 has a tolerance factor below 0.8 and an orthorhombic structure, which is also a yellow non-photoactive phase. However, with appropriate combinations of MA^+ and/or Cs^+ cations into FAPbI_3 , the tolerance factor can be tuned to stabilize the black photoactive alpha (cubic) phase at room temperature.¹⁰⁰

Besides stabilizing the black photoactive alpha phase, the composition of the perovskite also influences its other physical and chemical properties. The addition of MA^+ to the FA^+ cations at the A site slightly reduces the band gap and causes a red shift to the material's absorption edge. This increases the light harvesting ability of the perovskite to generate additional photo-generated charge carriers.¹⁰¹

The organic-inorganic lead halide perovskites suffer from degradation due to moisture,¹⁰² heat,¹⁰³ oxygen¹⁰⁴ and light.¹⁰⁵ Heat, oxygen and photo-illumination also accelerate the process of moisture-induced degradation.¹⁰⁶ The moisture sensitivity of organo-lead halide perovskites is primarily due to the hygroscopic nature of the organic cations at the A site.^{107, 108} Therefore, the moisture sensitivity can be minimized by blending it with some appropriate inorganic cation (such as Cs^+ or Rb^+).^{109, 110} To some extent, the addition of Cs^+ cations also reduces other degradation mechanisms such as thermal degradation, light-induced trap state formation, phase transitions, and bias-induced ion migration.¹⁰⁹

The Cs⁺ addition also renders the perovskite to be less sensitive to the processing conditions and thus enhance the device reproducibility. It suppresses the stabilization of yellow phase impurities to improve the fill factor and J_{SC}. Device hysteresis is also significantly reduced by Cs⁺ cation addition.¹¹¹

Moisture-induced degradation of the perovskite can also be minimized by tuning the chemical composition of the X site anions. This is because the moisture-induced degradation also involves the formation of hydrogen-halide bonds, which results in the breaking up of lead-halide bonds in the perovskite crystal.¹¹² The perovskites with mixed halides are slightly more stable against moisture, which is attributed to the lower energy of formation of H-I bonds than of H-Cl and H-Br¹¹³ bonds. The optical band gap of the perovskite can also be tuned by adjusting the amount and/or type of halide at the X site. This is because the conduction and valence band positions of perovskite depend on the nature of the hybrid orbitals of the lead and halide ions. The changes in the ionic radii and the electronic properties of different halides can principally introduce changes in the band gap of the perovskite.¹¹⁴

The organo-lead halide perovskite materials are also hazardous to health and environment due to the toxic nature of lead cations at the B site of the crystal structure. This creates an additional hurdle for its sustainable application and commercialization. The most common approach to encounter this problem is to use the chemical lead reduction strategy (CLR); in which lead is replaced with some other group 14 element such as Tin (Sn) or Germanium (Ge).^{115, 116, 117} A completely lead-free MASnI₃ was reported by Noel et al.¹¹⁸ in 2014 with a PCE of over 6%. Since then many CLR strategies were adopted to reduce the lead content in the perovskite. However, the overall device performance and stability of lead-free PSCs remain below organo-lead halide PSCs. This is because the B site cation in the perovskite must possess a stable +2 oxidation state while Sn and Ge are more stable in the +4 oxidation state. This not only affects the stability of the perovskite crystals, but also tend to introduce deep defect states. Zheng et al. introduced another strategy called physical lead reduction (PLR) in which the thickness of the perovskite light absorber was reduced to decrease the overall consumption of organo-lead halide material. This was done with some compromise in the device efficiency.¹¹⁹

In this thesis, a single cation MAPbI₃ perovskite deposited via the two-step sequential deposition method was used in the first two studies. In the third study, a triple cation perovskite prepared via the anti-solvent approach with Cs_x(MA_{0.17}FA_{0.83})(1-x)Pb(I_{0.83}Br_{0.17})₃ stoichiometry was used, which has earlier been reported by Saliba et al.¹²⁰

2.4.4. Charge-selective contacts for PSCs

Efficient electron-hole pair generation in the organo-lead halide perovskite active layer is highly dependent on its chemical composition, thickness and compactness. However, this is useful for a photovoltaic device only if the respective charge carriers produced within the active layer are efficiently extracted. For this purpose, material properties like charge selectivity and majority charge carrier extraction ability influence the selection of the most appropriate material to be used as charge extraction layers (or contacts) for a given photovoltaic device. In this chapter, I will briefly discuss about the contacts for extraction of charge carriers generated within the active layer of a solar cell upon illumination. A contact must be selective for the extraction of charges with one polarity, while it should be able to block the charges with the opposite polarity; this is called charge selectivity. Therefore, both electron-selective layers (ESL) and hole-selective layers (HSL) are vital in a good PSC. The charge extraction and transport mechanisms of ESL and HSL are highly dependent on their energy level band

alignment with respect to the perovskite light absorber material.¹²¹ The right selection and design of the ESLs and HSLs are crucial to avoid surface recombination, which directly influences important photovoltaic parameters such as V_{OC} (the open circuit voltage) and FF (the fill factor).¹²² In this section, fundamental information about the ESL is elaborated, while the most basic features about the HSL are also discussed.

2.4.4.1. Electron-selective layers

The main purpose of an ESL is to extract and transport the photo-generated electrons from the perovskite active layer to the transparent conductive oxide (TCO), such as FTO or ITO (indium-doped tin oxide). At the same time, it should be able to effectively block the holes from the perovskite. Unwanted recombination can occur during the electron extraction and transportation process, but this can be minimized considerably by selecting the proper ESL material.¹²¹ An appropriate ESL is said to give low dark currents and series resistances.¹²³ Its charge transport properties are highly dependent on the electron mobility, which should be high enough to avoid charge build-up at the ESL/perovskite interface while its work function and the conduction band edge should be aligned slightly below the conduction band minima of the perovskite active layer⁵⁶ (see Figure 4c). ESL materials can either be inorganic or organic. Inorganic ESL materials (such TiO_2 , SnO_2 and ZnO) are generally employed in the n-i-p configuration, while organic ESL materials (e.g., $PC_{71}BM$, fullurene C_{60} and its derivatives, etc.) can be utilized in both n-i-p and inversed p-i-n junction PSCs.¹²¹

2.4.4.2. Hole-selective layers

The hole-selective layer (HSL) is an important component in an efficient PSC. It prohibits the photo-generated electrons to be extracted, while it selectively extracts the photo-generated holes in the perovskite active layer and transports them to the back metal contact electrode (usually gold or silver). It also prevents a direct contact between the back metal contact electrode and the perovskite active layer, which enhances the device stability. A good quality HSL is important for a good hole extraction efficiency and influences the V_{OC} by determining the splitting of the quasi-fermi energy levels of the perovskite.^{124, 125, 126} Just like the ESL, HSL materials can also be organic or inorganic. To date, the organic Spiro-OMeTAD is the most widely used HSL material. However, it suffers from poor conductivity in its pristine form; therefore dopants such as cobalt complexes, 4-*tert*-butylpyridine and lithium bis(trifluoro-methyl sulfonyl)imide (Li-TFSI) are required in appropriate amounts to enhance the conductivity.¹²¹

2.5. TiO_2 electron-selective layer

TiO_2 has been extensively studied as a photo-catalyst due to its high chemical activity and stability.¹²⁷ Since it is a good n-type semiconductor, it has also been extensively used as photo-electrodes in different optoelectronic applications. Despite many other alternatives available, TiO_2 is still considered as one of the most suitable choices as the compact thin film and mesoporous electron selective layer in PSCs.¹²⁸ TiO_2 exists in three different polymorphs; brookite, anatase and rutile. All these crystal structures are in fact built up from distorted TiO_6 octahedras, but in different connection arrangements.^{127, 129} Anatase is the most widely used ESL material in PSCs, because it is economical, environmentally friendly, highly transparent, tailorable in terms of its electronic properties and highly compatible with perovskite in terms of its energy levels.¹³⁰ Rutile TiO_2 has a more positive conduction band edge than anatase, which results in lower V_{OC} in PSCs.¹³¹ Brookite is said to have a relatively more negative conduction band edge and therefore it can potentially give slightly better efficiencies in

DSSCs¹³² and PSCs.¹³⁰ In this thesis, compact and mesoscopic TiO₂ anatase layers were the main research focus.

TiO₂ (anatase) is known for its low electron affinity (−4.3 eV) and high ionization energy (−8.0 eV). The presence of some oxygen deficiencies in this material act as shallow donors and therefore TiO_x (anatase) is typically an n-type semiconductor with a work function between −4.3 to −4.5 eV, which is quite close to its conduction band edge. Its deep-lying valence band is primarily responsible for its hole blocking ability at its interface with the perovskite active layer.³ TiO₂ thin films in compact and mesoporous design have been widely studied for their application in PSCs. Extensive research in the last decade has focused on the different problems associated with TiO₂ ESL and some of the most important ones are discussed as follows.

The presence of morphological defects such as pinholes can result in direct contact between the perovskite active layer and the transparent conductive oxide (TCO), which results in excessive surface recombination at the perovskite/TCO interface.^{133, 134} Thus, the presence of pinholes in any ESL is indeed detrimental to the performance of PSCs.¹³⁵ Pinholes in ESLs are predominantly reported as incomplete surface coverage of the ESL film on top of the conductive FTO, which results in FTO crystals protruding through the metal oxide films creating a direct contact with the perovskite.^{133, 134} The poor wettability of the underlying conductive substrate (due to the presence of organic contamination) or microbubble formation during the film deposition or drying stages can be additional sources of incomplete coverage. Thus, they are most commonly reported in ultrathin metal oxide films used as ESLs. The exposure of the underlying TCO substrate can also be the consequence of thermally or mechanically induced cracks in relatively thick ESLs.^{53, 136} In this thesis, detailed experiments were performed to study pinholes in c-TiO₂ layer and their ultimate influence on the performance of PSCs.

Low electron mobility and variations in alignment of the TiO₂ conduction band edge relative to the perovskite generally act as sources of charge extraction barriers and reduce the charge extraction efficiency. There have been several concerns about lower PCEs and high hysteresis⁵⁶ when using TiO₂ as an ESL in the planar heterojunction PSC architecture. This is attributed to intrinsically low electron mobility ($10^{-5} \text{ cm}^2 \text{ V}^{-1} \text{ s}^{-1}$)¹³⁷ of TiO₂ and problems associated with a slight misalignment of its conduction band edge with that of the perovskite.^{56, 137} However, the hysteresis is also attributed to several other reasons, including ion movement which tends to counteract the internal electric field of the device and influence the charge extraction efficiency at the selective contacts.¹³⁸

The charge build-up at the TiO₂/perovskite interface, which significantly reduces the charge extraction efficiency, ultimately ends up with a poorly performing photovoltaic device. Upon introduction of a mesoscopic TiO₂ layer on top of the compact TiO₂ film, there is an improvement in the PCE and hysteretic behavior. This is due to an increase in the TiO₂/perovskite interfacial area, which has a positive influence on the electron extraction efficiency.¹³⁹ The optimal structure of the mesoporous TiO₂ layer in terms of porosity and pore size is important for efficient and low hysteretic photovoltaic devices.^{140, 141} The mesoscopic structure also acts as a scaffold to assist the crystallization of perovskite active layer. In the two-step sequential deposition of perovskite into a mesoporous scaffold layer, the conversion of PbI₂ to perovskite is more efficient compared to the conversion on top of a planar substrate. Sun et al¹⁴² studied the conversion efficiency of PbI₂ to perovskite as a function of the porosity of the mesoscopic TiO₂ layer. High porosity resulted in better infiltration of PbI₂ and CH₃NH₃I into the porous structure, which subsequently resulted in an improved conversion of PbI₂ to

perovskite. The device efficiencies with a highly porous mesoscopic layer were found to be 25% higher than for the devices with a low porosity mesoscopic layer. A similar approach was also reported by Shao et al.¹⁴³ They systematically demonstrated a reduction in hysteresis as a function of porosity. The significant reduction in hysteresis as a function of porosity was attributed to an increased interfacial contact between the perovskite and TiO₂ which suppresses charge accumulation at the interface. Seyed-Talebi et al.¹⁴⁴ studied the crystallization and nucleation of perovskite as a function of TiO₂ porosity. Higher porosity resulted in large grain-sized perovskite that gave higher device efficiencies, while the enhanced interfacial contact area between perovskite and TiO₂ resulted in a reduced hysteresis. The crystallization of the perovskite capping layer, which should be highly compact and pinhole-free to avoid the formation of parallel shunts between HSL and TiO₂ ESL, is influenced by the nucleation at the TiO₂ mesostructure. Better pore filling of the perovskite also suppresses the decomposition of the perovskite to PbI₂, which is only possible with a highly porous scaffold layer. Block co-polymer-templated ordered mesoporous TiO₂ layers have also been used to make efficient perovskite solar cells.^{141, 145} In this thesis, some preliminary experiments were performed to study ordered mesoporous layers as scaffold layers, which later on turned out to be useful to model pinhole-containing compact TiO₂ layers in planar heterojunction PSCs.

Several other approaches have been found to effectively counteract the issues related to charge build-up at the TiO₂/perovskite interface. One of these approaches includes the modification of **surface properties** of compact and mesoscopic TiO₂ thin films. For instance, Giordano et al.¹⁴⁶ doped mesoporous TiO₂ ESL with Li⁺ ions to passivate the electronic defect states, which act as non-radiative recombination centers. This resulted in increased charge collection efficiency of TiO₂ photo-electrode and therefore the PCE improved from 17% to above 19%. The hysteresis index also reduced significantly to below 0.3%. Passivation of the electronic defect states at the surface (and bulk) of TiO₂ ESLs has been carried out in a number of ways, including the use of single-walled carbon nanotubes (SWCNTs).¹⁴⁷ The use of specialized ionic liquids is also said to reduce the sub-band gap electron trap states in TiO₂ close to its interface with the perovskite and improve the electron extraction efficiency of the ESL.¹⁴⁸ Though the planar heterojunction device architecture suffers from poor charge collection efficiency (especially under forward voltage sweep),¹⁴⁹ Wojciechowski and Li et al. showed a significant improvement in the performance of such devices by modifying the c-TiO₂ surface with fullerene derivatives.^{150, 151} Tao et al. introduced a C₆₀-PCBM interlayer between the compact TiO₂ ESL and the perovskite active layer, which helped to reduce s-shaped features in the light J-V curves in forward sweep. Furthermore, it also reduced the hysteretic behavior of the planar device.¹⁵²

Cojocaru et al. reported that an additional TiCl₄ chemical treatment is beneficial for the TiO₂/perovskite interface.¹⁵³ The TiCl₄ treatment of the compact TiO₂ layer tends to fill in the cracks and other morphological defects such as pinholes; thus this significantly improves the device efficiencies for planar heterojunction PSCs.¹⁵⁴ The TiCl₄ treatment helps to remove surface trap states which act as charge recombination centers. From a morphological point of view, it reduces the agglomeration of TiO₂ nanoparticles in the mesoscopic layer. Furthermore, it controls the surface roughness and pore size which is needed for optimal loading of the nanostructure with the active perovskite material.¹⁵⁵ The TiCl₄ treatment also improves the interconnectivity between the TiO₂ nanoparticles building up the mesoscopic layer.¹⁵⁶

Increasing the wettability of mesoporous TiO₂ by surface treatments such as UV-ozone¹⁵⁷ is generally practiced before the deposition of the perovskite via the 1-step method. This further increases the

nucleation centers¹⁵⁸ on the scaffold structure, which renders a highly compact capping layer of perovskite. The UV or UV-ozone treatment of TiO₂ can also change the oxidation state of the titanium cation from Ti⁴⁺ to Ti³⁺, which is due to the creation of oxygen vacancies in the TiO₂ lattice.¹⁵⁷ Oxygen vacancies generally act as n-type dopants to shift the work function closer to the conduction band minimum,⁶¹ which can ultimately enhance the conductivity of TiO₂. This potentially supports the electron extraction from the perovskite and thus reduces the chance for recombination.¹⁵⁷ Prior to the deposition of the active material on top of the TiO₂ layer, surface treatment by UV-ozone also helps to remove residual organics (originating from the precursors, solvents, or atmosphere), because these organics tend to form surface states which are detrimental to efficient electron injection into TiO₂.¹⁵⁹

It is well-known that oxygen plasma treatment of TiO₂ surface also plays a vital role in removing organic species from TiO₂ surfaces; however no systematic study has been performed to study the influence of oxygen plasma treatment on the photovoltaic performance of PSCs. Nevertheless, some studies show that plasma treatment improves the loading of photoactive dye for DSSCs.¹⁶⁰ In the second study of this thesis, we systematically studied the effect of oxygen plasma and UV-light surface activation of the mesoscopic TiO₂ scaffold on the resulting perovskite composition and morphology.

Electron back-transfer from TiO₂ to the perovskite is said to be another reason behind recombination at the TiO₂/perovskite interface. Different methodologies have been adopted to counteract electron back-transfer such as the use of p-type CuI islands at the TiO₂/perovskite interface.¹³⁷ The use of inert metal oxide nanoparticles on top of the c-TiO₂ layer, such as Al₂O₃,^{67, 161} or ZrO₂,¹⁶² have been reported to effectively enhance the V_{OC} of the device. Mesoscopic TiO₂ films comprising ultrathin MgO-coated TiO₂ nanoparticles on top of the c-TiO₂ significantly improves the fill factor along with the V_{OC}.¹⁶³

The use of different TiO₂ precursors, such as titanium isopropoxide, titanium diisopropoxide bis(acetylacetonate), and titanium tetrachloride (TiCl₄), significantly influences the **morphology and crystallinity** of the resulting TiO₂ films. For example, the use of TiCl₄ as a precursor has been reported to produce pinhole-free and smooth compact TiO₂ layer for efficient and low hysteresis PSCs.¹⁶⁴ The presence of chloride ions on the surface of compact TiO₂ films and at their interface with the perovskite active layer tend to suppress deep trap states and minimize the interfacial surface recombination. This tends to enhance the V_{OC} and the FF with additional long-term stability.^{165, 166}

The presence of sub-band gap states can result in non-radiative recombination within the ESL material and this would adversely affect the electron-transfer to the transparent conductive oxide. The presence of these sub-band gap states at the TiO₂/perovskite interface can be a source of surface recombination and therefore adversely affect the device performance. The sub-band gap states are also sometimes formed during prolonged light soaking which is one of the fundamental reasons behind reduced long-term stability of the photovoltaic device.¹²⁸ This is generally because the UV part of the solar spectrum render the direct excitation of the TiO₂ band gap, which results in the photocatalytic desorption of oxygen from TiO₂ surface. The removal of oxygen results in the activation of oxygen vacancies, which act as mid-gap trap states for the electrons being injected into the conduction band of TiO₂. These electrons are not mobile if they fall into the mid-gap states. Instead, they tend to undergo recombination at the TiO₂/perovskite or the TiO₂/HSL interfaces. This process is time dependent and prolonged light soaking results in a significant decrease in the magnitude of photocurrents. This can generally be avoided by using UV cutoff filters, which even go up to 450 nm, in order to prevent direct band gap excitation of TiO₂ selective contacts. However, this also significantly

reduces the overall device performance. The use of UV cutoff filters is generally used when studying the long-term stability of PSCs or DSSCs.^{167, 168}

The ESL **film deposition method and deposition rate** can significantly influence the surface coverage and the denseness of produced ESL layer.¹⁶⁹ Thus, TiO₂ layers deposited via different methods can influence the device performance. Some deposition methods are *vapor phase methods*, while others are *solution-process able*. Vapor phase methods include pulsed laser deposition (PLD) for both compact¹⁷⁰ and nanostructured TiO₂¹⁷¹, and radio frequency (RF) magnetron sputtering¹⁷² although none of them have been widely studied. On the other hand, atomic layer deposition (ALD) has frequently been reported and is often referred to be the best ESL deposition technique owing to its capability to deposit uniform, dense, and defect-free films even on rough substrates.¹⁷³ This is because ALD films tend to follow the same texture as that of the underlying FTO substrate. This is contrary to the solution-processed TiO₂ ESL films, which tend to have variations in film thickness due to the change in the texture of the FTO substrate.¹⁷³ Methods based on solution-processing include spray pyrolysis, spin coating and dip coating.

In order to fabricate large-scale PSC panels, it must be possible to deposit all layers via scalable film deposition approaches. Scalable deposition of thin films means that the film quality and thickness are uniform regardless of the substrate size. Scalable deposition methods include inkjet printing, aerosol spray pyrolysis, and dip coating. Huckaba et al¹⁷⁴ reported that inkjet printing can be used to deposit scalable mesoporous TiO₂ layers for PSCs. Furthermore, initial efforts of depositing perovskite by a sequential dip coating process has been already tested to prepare perovskite layers on top of 30 x 26 cm² substrates.¹⁷⁶ Since the dip coating method is known to be highly scalable, this method was primarily used for the deposition of compact TiO₂ layers in this thesis. In order to minimize manufacturing costs, it is also desirable if the deposition techniques support roll-to-roll manufacturing. Apart from the spin coating method, the deposition techniques described in the following text (ALD, spray pyrolysis, and dip coating) are all compatible with roll-to-roll manufacturing.¹⁷⁷ However, roll-to-roll processing generally involves flexible polymeric substrates, which limits them to relatively low processing temperatures. In this section, the most widely used deposition methods are discussed, which also includes the dip coating method.

1. Atomic layer deposition

Atomic layer deposition (ALD) is an ideal tool for the preparation of efficient and stable PSCs.¹⁷³ This method can produce thin film semiconductors with atomic scale precision with the ability to tune the material composition and film thickness with excellent conformity.¹⁷⁸ Pinhole-free and more homogeneous compact TiO₂ layers can be achieved with the ALD method in comparison to solution-processed layers.¹⁶⁹ The compact TiO₂ films are highly uniform and follow the texture of the underlying conductive FTO substrate. The ALD method has also proven to be an excellent deposition technique to fabricate highly efficient HTM-free PSCs.¹⁷⁹ Lu et al. pointed out that the optimum thickness of TiO₂ ESL films in PSCs is about 10 nm when prepared via the ALD method, which is thinner than for other deposition techniques.¹⁸⁰ Lu et al. later proposed that the conduction band edge and the Fermi level of TiO₂ prepared via the ALD method are slightly lower than for the solution-processed c-TiO₂ films, which can be another potential reason behind better device performance.¹⁸¹ ALD technique is also suitable for roll-to-roll manufacturing.¹⁸² ALD process is schematically described in Figure 7.

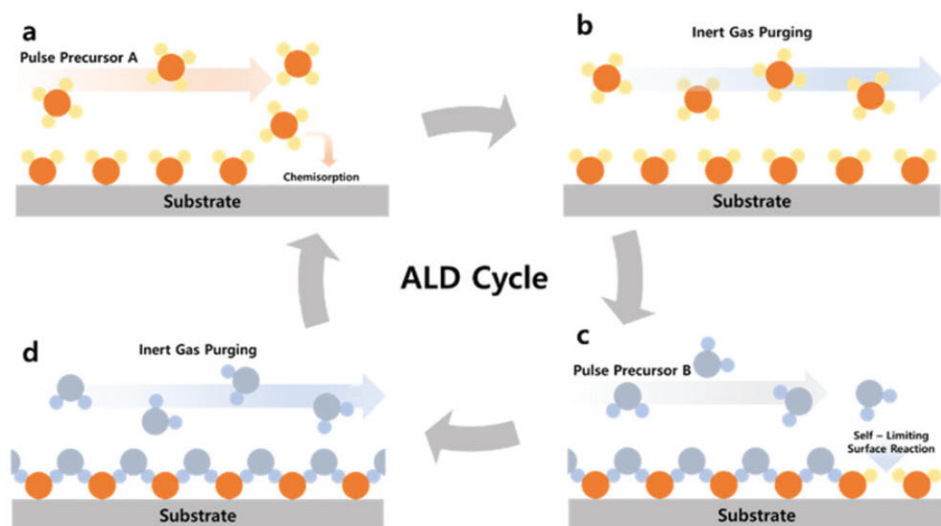


Fig 7. Schematic representation of a typical ALD process. It shows one cycle which forms one monolayer of the substance on the substrate. (a and c) A and B source precursor pulse; (b and d) inert gas purging of the of residual precursor source.¹⁷³

The ALD process is a layer-by-layer deposition method of inorganic thin films on a substrate. The substrate is exposed to the reactants in the form of gaseous precursors. Unlike chemical vapor deposition, ALD does not allow all the reactants to approach the substrate simultaneously; rather it allows one reactant to enter the reaction chamber at a time. In other words, the reactants are injected into the reaction chamber sequentially in the form of non-overlapping pulses. In each of these pulses, the reactant molecules react with the surface such that once the reactive sites on the surface are consumed, the reaction stops automatically. This is one ALD cycle. The thickness of the film deposited in one ALD cycle depends on the nature of precursor-surface interaction. Therefore, in order to reach the required level of film thickness, repeated number cycles need to perform.¹⁸³

Although ALD can produce high quality TiO_2 films, there are several drawbacks with the method that limits its use in the fabrication of PSCs. Precursor and purging pulses are time-consuming processes. Thus, the effective deposition rate is even lower than in other chemical vapor deposition (CVD) processes.¹⁸³ The equipment itself and the infrastructure required for this process are very expensive and thus it is not readily available.¹⁸⁴ Furthermore, high purity substrates are required which adds cost to the process.¹⁸⁵

2. Aerosol spray pyrolysis

Spray pyrolysis is said to be a scalable and low-cost deposition method for making compact TiO_2 layers. It can produce TiO_2 anatase films of a similar quality as in spin coating, but the films prepared via spray pyrolysis are ultra-compact, bulk-like films with a reduced defect density.¹⁸⁶ There are variations in the setup for the spray pyrolysis of thin metal oxide films.¹⁸⁷

Aerosol spray pyrolysis of c- TiO_2 layers generally requires a hot plate on which FTO glass substrates can be directly placed.⁵² The solution for spray pyrolysis comprises of acetylacetone and titanium

diisopropoxide bis(acetylacetonate) dissolved in ethanol. The solution is sprayed onto the substrate with pure oxygen as a carrying gas. The spraying is performed at an angle of about 45° to the surface of substrate. The spraying is performed by rapidly moving the nozzle around in a single circle to cover all the substrates placed on the hot plate.

The spray pyrolysis method is the most widely used method for the fabrication of highly compact TiO₂ ESLs for PSCs. It is also well known to be suitable for roll-to-roll manufacturing, which is not only economical but also efficient because of its continuous nature. Perovskite photovoltaic devices comprising compact TiO₂ layers prepared via spray pyrolysis generally perform better than devices made from spin-coated compact TiO₂ layers.¹⁶⁹ Compact TiO₂ films made by spray pyrolysis are also used for other applications such as sensors and photocatalysts.¹⁸⁷

Unfortunately, the spray pyrolysis technique requires a good hands-on experience in order to prepare reproducible compact TiO₂ films. There is a high risk of variations in the film quality depending on the person who is performing the deposition. This is because the spraying is performed manually by moving the spraying nozzle in a circle above the substrates at an approximate angle of 45° with respect to the substrate surface.

3. Spin coating

Spin coating is another technique to deposit thin films such as compact and mesoporous TiO₂ thin layers on flat substrates. A small amount of the colloidal precursor dispersion is applied on the center of the substrate. The substrate is then rotated with a high speed in order to spread the colloidal dispersion (or any coating material) under the influence of centrifugal acceleration. If the colloidal dispersion is applied on the substrate while it is rotating, it is called dynamic spin coating. The equipment used to perform spin coating is called a spin coater.

The rotation of the coated substrate is continued to remove excess fluid, which spins off the edges of the substrate until the required film thickness of the remaining gel-like film is achieved. The solvent used to prepare the coating material is usually very volatile so that it is able to simultaneously evaporate during the spinning process. However, non-volatile solvent like water can also be used. Solidification due to evaporation starts in the middle of the substrate and continues until the entire film is solidified (see Figure 9). Furthermore, remnants of the solvent can be evaporated by subsequent annealing of the substrate at an appropriate temperature. The concentration and viscosity of the solution and spin speed determines the ultimate film thickness. The pioneering theoretical analysis of the spin coating process was performed by Emsile et al.¹⁸⁸

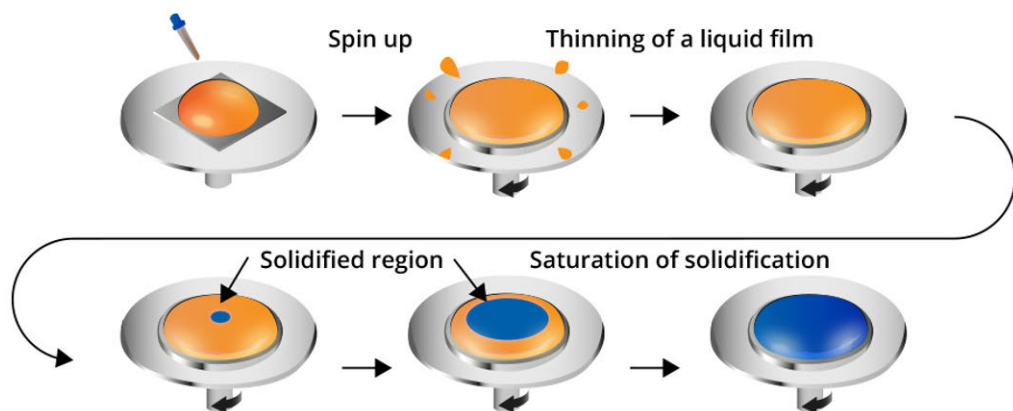


Fig 9. Spin coating sol-gel steps.¹⁸⁹

The mesoscopic TiO_2 , perovskite, and HSL layers are usually prepared via spin coating. However, spin-coated compact TiO_2 ESL layers are reported to have a higher density of pinholes in comparison to compact layers prepared from ALD or spray pyrolysis.¹⁶⁹ This is manifested by inferior device performance in comparison to devices prepared on ALD or spray-pyrolyzed compact TiO_2 layers. This technique also pose limitation towards scalable devices because the final film is not uniform in terms of thickness. Furthermore, spin coating is a batch process that does not comply for roll-to-roll manufacturing at the industrial scale.¹⁷⁷ Furthermore, this technique pose limitation towards scalable devices, because the final film is not uniform in terms of thickness. The most widely used deposition techniques for making compact TiO_2 are spray pyrolysis and spin coating.¹⁹⁰

4. Dip coating

In this thesis, all devices were prepared on top of dip-coated compact TiO_2 ESL (i.e., the first deposited layer in the device). Hong et al. prepared c- TiO_2 layers via dip coating route.¹⁹⁰ A similar study was performed by Haimeur et al¹⁹¹ in which they determined the optimal thickness of compact TiO_2 layer to be about 50 nm. Above 50 nm, the optical and electronic properties of compact TiO_2 tend to adversely affect the device performance. Also, optimization of ultrathin dip-coated compact TiO_2 ESL for perovskite solar cells is reported in this thesis (see Study 1). Furthermore, Huang et al¹⁹² reported efficient perovskite solar cells with low hysteresis by depositing the compact TiO_2 and perovskite active layers by dip coating.

Dip coating is one of the oldest commercially applied coating processes. It involves dipping the entire substrate into a solution or dispersion followed by its withdrawal at a constant speed. The process comprises of the three following stages:¹⁹³

- a. **Immersion and dwell time:** The substrate is immersed into the precursor solution and subsequently left there for a certain dwell time in order to ensure sufficient interaction between the solution and the substrate.
- b. **Deposition and drainage:** The substrate is pulled out of the solution in the upward direction with a constant speed, which results in the formation of a thin layer of precursor solution on the substrate. The excess solution is drained from the surface under the influence of gravity.

- c. **Evaporation:** The solvent evaporates from the film to form a gel while further removal of the solvent can be promoted by heating. The coating might be subjected to further heat treatments at elevated temperatures to decompose residual organics and/or to induce crystallization of the deposited material.

At a first glance, the dip coating process appears rather simple. However, a more detailed understanding of the process at a microscopic scale enables one to tailor the quality and structure of final films. Having understanding of the fundamentals of sol-gel processing is the key to optimize the coatings according to the requirements for a particular application.

The sol-gel process for the preparation of TiO_2 thin films can be explained in terms of the partial charge model which was introduced by Jolivet and co-workers.¹⁹⁴ Upon adding the TiCl_4 precursor to an aqueous solvent (in this case a mixture of ethanol, tetrahydrofuran and water), the precursor dissociates into Ti^{4+} and Cl^- ions. The solvated Ti^{4+} ions are easily hydrolyzed in the aqueous environment, which ultimately lowers the pH of the sol. This results in the formation of aquo-hydroxo complexes $[\text{Ti}(\text{OH})_2(\text{OH}_2)_2]^{2+}$ in the dip coating solution.¹⁹⁵ Upon withdrawing the substrate from the solution, solvent evaporation increases the concentration of this complex to initiate sol-gel condensation reactions that form an amorphous titanium oxide layer on the substrate surface. Thereafter, the film is exposed to high temperature calcination to convert it to crystalline anatase TiO_2 .

The substrate is withdrawn upwards from the solution reservoir at a constant speed U_0 . The upward movement of the substrate entrains the liquid in a fluid mechanical boundary layer, which splits into two parts above the surface of the solution reservoir, such that the outer layer of the liquid returns back to the solution reservoir (see Figure 10). The point at which the liquid splits into two parts is called the stagnation point (S). As a result of solvent evaporation and liquid drainage back into the reservoir, the entrained liquid film on the substrate acquires a wedge-like shape, which terminates at a well-defined drying line (marked as $x = 0$ in Figure 11). Above this drying line (also called the triple phase boundary), non-volatile species such as the precursor and possible polymeric templating agents (such as block co-polymers) form an as-deposited layer called a gel, which can later be subjected to further curing, e.g., via calcination.¹⁹³

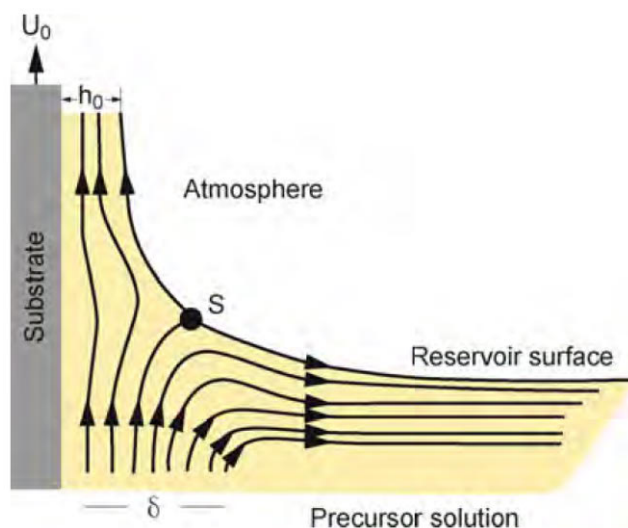


Fig 10. Detailed schematic of the flow patterns (or streamlines) during the dip coating process. U_0 is the withdrawal speed, S is the stagnation point, δ is the boundary layer, and h_0 is the thickness of the entrained fluid film on the substrate.¹⁹³

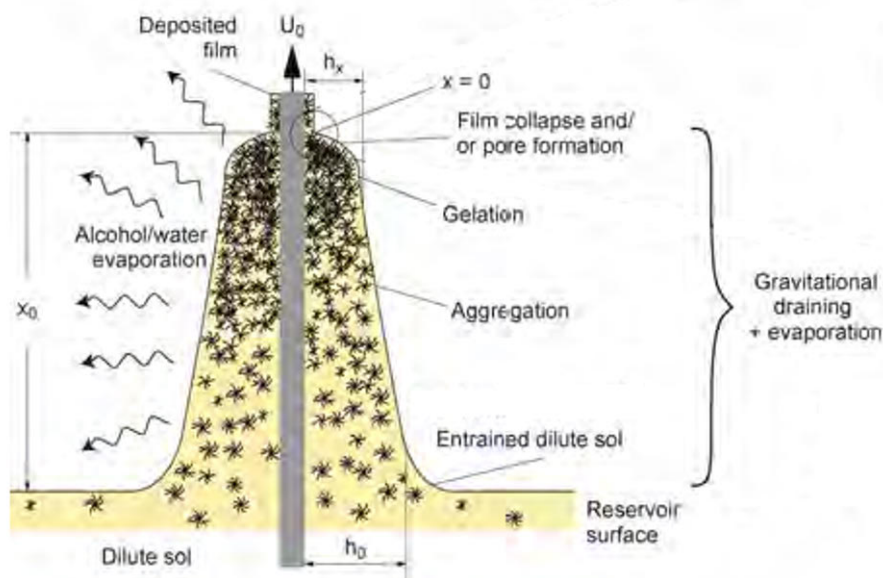


Fig 11. Schematic representation of structural development of the thin film during dip coating performed at a constant withdrawal speed (U_0). The gel-like film is formed as a result of draining along with solvent evaporation and continuous condensation reactions. U_0 is the withdrawal speed, $h(x)$ is film thickness at position x (taking $x=0$ at drying line). h_0 is the entrained film thickness just above the stagnation point S (before evaporation).¹⁹³

If the withdrawal speed (U_o) and the liquid viscosity (η) is high enough to lower the curvature of gravitational meniscus, the thickness of as deposited film (h_o) tends to balance the viscous drag (ηU_o) and gravity force (ρg) according to the following equation:¹⁹³

$$h_o = c_1 \left(\frac{\eta U_o}{\rho g} \right)^{1/2}$$

where ρ is the density of the liquid, g is acceleration due to gravity and c_1 is a constant (0.8 for Newtonian liquids).

When the withdrawal speed of the substrate from the solution is low (typically between 1 to 10 mm/s) and the viscosity of the solution is also low (which is normally the case for sol-gel systems), the liquid-vapor surface tension plays a crucial role in the final film thickness. The equation can then be written as follows:¹⁹³

$$h_o = 0.94 \frac{(\eta U_o)^{2/3}}{\gamma LV^{1/6} (\rho g)^{1/2}}$$

2.6. Ordered mesoporous TiO₂ layers

Different morphologies of mesoporous TiO₂ layers have been incorporated into PSCs to investigate how they contribute to the device performance. Among them, nanoparticle-based^{191, 196, 197} (most widely reported so far), nanorods,¹⁹⁸ inverse opal,¹⁹⁹ and ordered mesoporous¹⁴⁵ structures have been reported. In the first two studies of this thesis, nanoparticles were used to prepare mesostructured TiO₂ layers as scaffold in the devices. Block co-polymer-templated ordered mesoporous TiO₂ films have been previously employed as mesoscopic scaffolds in PSCs.¹⁴⁰ However, in the third study of this thesis, ordered mesoporous TiO₂ films were used to model compact TiO₂ layers containing well-defined pinholes. The porous films were then incorporated into planar heterojunction PSCs to investigate the influence of so-called “induced pinholes” on the device performance. These films were prepared by the evaporation-induced self-assembly (EISA) method, which was first reported by Stucky et al. as an alternative method to synthesize mesoporous transition metal oxides.²⁰⁰ Gradual evaporation of alcohol is followed by the formation of an inorganic network with nanocrystalline domains around the voids of a liquid crystalline phase. As a consequence, well-defined ordered mesophases are formed.

The preparation of ordered-mesostructured thin films involves different parameters which influence the evaporation-induced self-assembly process. They can be divided into two broad categories:²⁰¹

1. **Chemical parameters:** which can only be controlled during preparation of the dip coating solution. For instance, the relative amounts of surfactant, inorganic precursor and the solvent which ultimately influence the classical sol-gel hydrolysis-condensation reactions in the initial sol.
2. **Processing parameters:** This can be controlled during the deposition process, such as the relative humidity. These parameters govern the diffusion of volatile species such as ethanol and water molecules to and from the film. They tend to influence the final composition, morphology and thickness of the final mesostructured film.

In order to prepare ordered mesoporous thin films with high reproducibility, optical homogeneity and transparency, it is important to understand the three main stages of EISA process which are listed and explained as follows while they are schematically explained in Figure 12.²⁰¹

a. The preparation of the initial sol

Homogeneous films are formed only if the solvent is highly volatile and able to wet the substrate. The chemistry of the inorganic precursor and the surfactant head groups must be known since the self-assembly during the deposition process is highly influenced by the interactions between them. The initial solution must be a perfectly controlled sol-gel system such that the hydrolysis and the condensation steps of the precursor are adjusted by selecting the appropriate components and their relative amounts (which include the pH, water content and the level of dilution). Furthermore, the relative amounts of the organic templates and the inorganic precursors must be adjusted to form stable intermediate phases and the final structure which must not collapse during the treatment process when the organic template is removed. The relative amount of the organic template also decides the final mesostructure in terms of morphology and porosity. The initial solution should be able to favor fast hydrolysis and slow condensation so that small inorganic oligomers form quickly while they do not further condense to form continuous inorganic network at macro scale within the solution. The initial sol is shown as step 1 in Figure 12. At this stage, the inorganic precursors or oligomers, surfactant molecules are suspended in the ethanol/water solvent.²⁰¹

b. The processes during film deposition via dip coating

A layer of the initial sol is left deposited on the surface of substrate upon withdrawing it from the initial sol with a continuous speed. Immediately after deposition, the evaporation of the volatile species such as water and ethanol takes place at the air/film interface. The evaporation results in progressive enrichment of TiO_2 oligomers and surfactant molecules. When the concentration of the surfactant molecules reaches the critical micelle concentration (CMC) in the deposited sol, micelles start to form due to the segregation of hydrophobic chains in the surfactant molecules. The segregation of the inorganic titania oligomers followed by their further condensation around the micelles ultimately results in the formation of a well-organized hybrid intermediate mesostructured film which behaves like a liquid-crystalline (LC) phase. At this stage, one can modify the ordered arrangement of the mesostructure by varying the atmospheric composition. The volatile molecules (i.e., ethanol and water) equilibrate between the film media and the environment. In other words, the amount of volatile species in the film can be modulated by adjusting the vapor pressure in the atmosphere. For example, the quantity of water in the film at this stage varies as a function of relative humidity (RH). This period is therefore called the modulable steady state (MSS). During this stage, the ordered arrangement of the mesostructure can be varied by controlling the atmospheric conditions (especially the relative humidity). EISA can thus be described as a competition between the kinetics of condensation versus the kinetics of organization (of micelles and the inorganic titania network in the film medium). Both of these kinetics can be controlled by modulating the kinetics of diffusion of volatile species to and from the film.²⁰¹

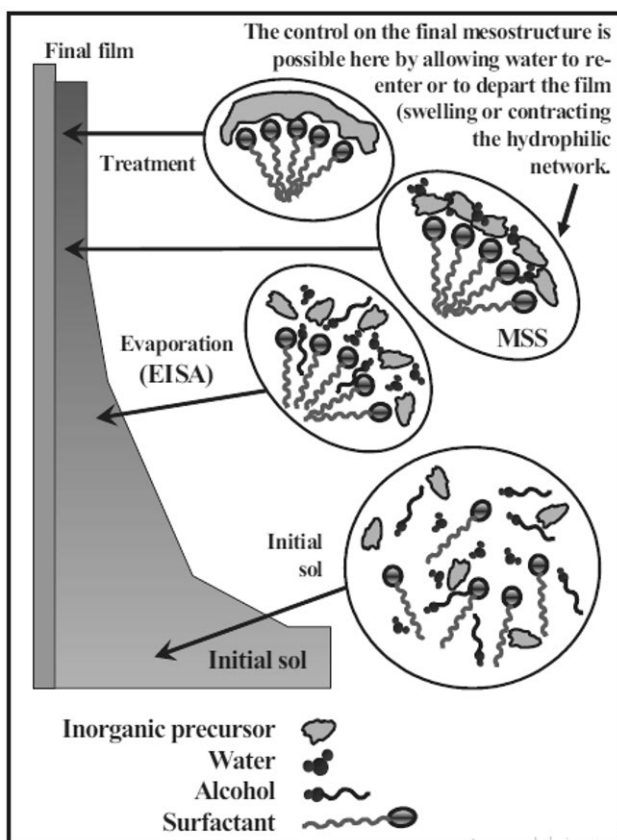


Fig 12. Deposition of mesostructured thin film by dip coating method. **Step 1**; the initial sol comprising of inorganic precursor, surfactant molecules suspended in ethanol-water mixture as a solvent. The concentration of the inorganic precursor is optimized to slow down its condensation. **Step 2**, the evaporation of the volatile solvent takes place while the surfactant molecules start to form micelles as soon as their concentration exceeds the CMC. **Step 3**, this stage is also called modulable steady state (MSS). The evaporation of solvent is complete and the film equilibrium is established between the film and its surroundings. The final mesostructure can be modulated by controlling the RH. **Step 4**, the inorganic network is completely condensed to form a stable hybrid mesostructure.²⁰¹

c. The treatment stage

This step is performed in order to complete the condensation of the inorganic titania network and to induce the porosity by eliminating the template. This is usually done by heat treatment at elevated temperatures which results in stiffening and crystallization of the amorphous inorganic network and thermal decomposition of the organic phase. This stage is usually accompanied by unidirectional contraction of the film perpendicular to the substrate surface.²⁰¹

3. Aims of the study

In this thesis, TiO_2 compact and mesoporous thin films were studied as electron-selective layers in PSCs. The compact TiO_2 is a dense layer which is used with or without subsequent mesoporous TiO_2 layer (which is then loaded with the perovskite active layer). The mesostructured TiO_2 layer acts as a scaffold to support the crystallization of the perovskite and increase the interfacial contact between the perovskite and TiO_2 (ESL). Devices without mesoscopic TiO_2 layers are called planar heterojunction PSCs, which have a simpler device architecture in comparison to mesoscopic PSCs (the detailed discussion about PSC architectures can be found in section 2.4.2.). For this thesis, three different studies were performed on TiO_2 ESLs for PSCs, which are schematically described in Figure 13.

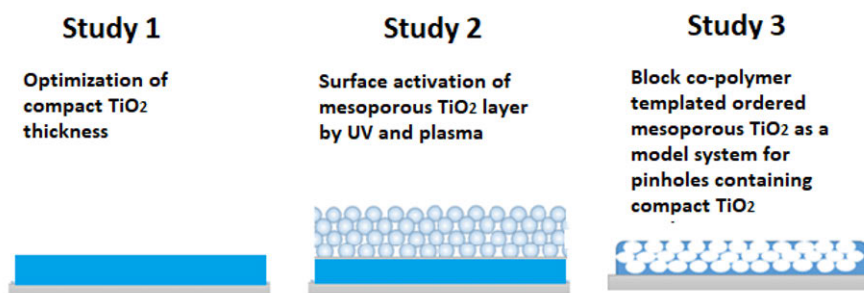


Fig 13. Schematic representation of the study plan for this thesis.

Study 1: The presence of morphological defects in an ESL such as pinholes can pose a serious threat to the performance of PSCs. The pinholes in an ESL are a source of direct contact between the perovskite and transparent conductive substrate (such as FTO). This results in a very high level of surface recombination at FTO/perovskite interface and the induction of leakage currents into the device. Therefore, the first aim of this research thesis was to optimize the thickness of TiO_2 ESL for the optimal performance of mesoscopic PSCs (prepared via two-step sequential deposition of the perovskite active layer). The thickness of compact TiO_2 layer was optimized by tuning the concentration of TiCl_4 precursor in ethanol/water solution (which was then deposited using the dip coating technique). The ultimate goal was to overcome the presence of pinholes in the compact TiO_2 ESL to avoid parallel shunts between perovskite and FTO. The compact TiO_2 layer with optimal thickness was later used in Study 2.

Study 2: An optimal nanoparticle-based mesoscopic TiO_2 layer is important to ensure high electron extraction efficiency to get the optimal performance of a PSC. Thus, a systematic study was performed to investigate the effect of various surface activation methods for mesoscopic TiO_2 layers on the performance of mesoscopic PSCs. Nanoparticle-based mesoporous TiO_2 layers coated on top of c- TiO_2 /FTO/glass substrates were subjected to two different surface activation protocols (oxygen plasma and UV light) prior to the deposition of perovskite (via the 2-step deposition method). The two different surface activation protocols significantly influenced the device performance due to a change in the perovskite morphology, and the conversion efficiencies of PbI_2 to MAPbI_3 .

Study 3: Block co-polymer-templated ordered mesoporous TiO_2 thin films were used to model compact TiO_2 layers containing a high density of “induced” pinholes. The pinholes are well known to be detrimental to the device performance owing to the formation of parallel shunt pathways as a result of direct contact between perovskite and the FTO. Thus the aim of this study was to deliberately induce the defects (i.e., the pinholes) in the compact TiO_2 films and study how far they can reduce the device performance provided that the pinholes are extremely narrow (i.e., in between 13 to 15 nm). The increase in compact TiO_2 film porosity was modelled as increase in the pinhole density. The planar heterojunction device architecture was used (in this study) to avoid the covering of pore openings by the TiO_2 nanoparticles which are generally used to prepare the mesoscopic scaffold layer (just like in study 1 and 2). The device performance as a function of film porosity was studied where the porosity was tuned by changing the block co-polymer to TiCl_4 precursor molar ratio. Film thickness was also changed while keeping the constant porosity by tuning the solvent content in the sol used to deposit the TiO_2 film. The porous films of different thickness were also studied against the device performance.

4. Experimental

4.1. Materials

1. Conductive and non-conductive substrates for thin film analysis and devices:

- TCO22-7/Li fluorine-doped tin oxide coated glass (7 ohm/sq. FTO) from Solaronix SA.
- TCO22-15 fluorine-doped tin oxide coated glass (15 ohm/sq. FTO) from Solaronix SA.
- Non-conducting microscope glass substrates from VWR International.

2. TiO₂ compact layers:

- Precursor*: TiCl₄ (>99%) from Fluka.
- Wettability enhancer*: Pluronic F127 block co-polymer from Sigma Aldrich.
- Solvents*: Ethanol (>99.5%) from ALTIA Oyj, tetrahydrofuran (THF, > 99%) from Sigma Aldrich.
- Poly (butadiene-*b*-ethylene oxide) di-block co-polymer templates*: P2952-BdEO, P2326-BdEO, P19919-BdEO from Polymer Source.

3. Mesoscopic TiO₂ scaffold:

- Nanoparticle paste*: 30 NR-D transparent titania paste, from Greatcell Solar.
- Solvent*: Ethanol (>99.5%) from ALTIA Oyj.

4. Perovskite light absorber:

- Salts*: Lead (II) iodide (PbI₂, >98.0%), lead (II) bromide (PbBr₂), Methyl Ammonium Iodide (MAI>98.0) from TCI (Tokyo Chemical Industries co) Europe. Formamidium Iodide (FAI), Methyl Ammonium Bromide (MABr) from Greatcell Solar. Cesium Iodide (CsI > 99.999%, PURATREM) from Gute Chemie abcr
- Solvents*: N,N, Dimethylformamide (DMF, Anhydrous 99.8%), Dimethylsulfoxide-d₆ (anhydrous, 99.9 atom %), 2-Propanol (Anhydrous 99.5%) from Sigma Aldrich

5. Hole Transport Material:

- Polymer*: Spiro-OMeTAD (99%) from Feiming Chemicals Ltd. and Luminescence Technologies Corp.
- Dopant salts*: bis(trifluoromethane)sulfonimide (Li-TFSI), tri-*s*-(2- (1H-pyrazol-1-yl)-4-tert-butylpyridine) (4-TBP) and cobalt(III) tri[bis-(trifluoromethane)sulfonimide] (FK 209 Co (III), >98%) from Sigma Aldrich
- Solvents*: Chlorobenzene (Anhydrous 99.8%), Acetonitrile (anhydrous 99.8%) from Sigma Aldrich.

6. Top metal electrode:

Gold, Au wires. (from Jalometallitukku Bergman and 24 karat)

4.2. Device architecture

Figure 13 shows two-dimensional schematics describing the dimensions of the PSCs samples used in this work. Each sample comprises of two back metal contacts made of gold. In other words, there are two devices per sample. A 4 cm x 2 cm piece of FTO glass substrate was initially etched from one side and the dimension of the etched region was 1.5 cm x 2 cm (see Figures 14a and 14b). The other layers for the preparation of PSCs were subsequently deposited as shown in Figure 14c and 14d. Overall, Figure 14c is helpful to explain the importance of etched region. One end of the gold metal electrodes should lie on top of the spiro-OMeTAD-based hole transport layer, while the other end of the gold contact should be in the etched region. If FTO is not removed from this region, the gold contacts will be in direct contact with FTO causing direct shunts. If this region is not properly etched, i.e., when some FTO still remains, there is a risk of contact-related issues in the devices. The first study was performed using TCO22-7/Li FTO glass (sometimes called Tec 7), while the rest of the studies utilized TCO22-15 FTO glass (Tec 15). In the first study of this thesis, I observed that chemical etching of the TCO22-7/Li FTO glass is more difficult than for TCO22-15, because despite repeating the chemical etching multiple times, it was not possible to completely remove the remaining FTO in the case of TCO22-7/Li. This could easily be observed with a simple multimeter, which would show substantial conductivity in the etched region. Therefore, in Study 1, laser etching was performed to remove the FTO layer. On the contrary, the TCO22-15 FTO glass would not show any conductivity (i.e., infinite or very high resistance) when chemical etching was performed using zinc and aqueous HCl solution.

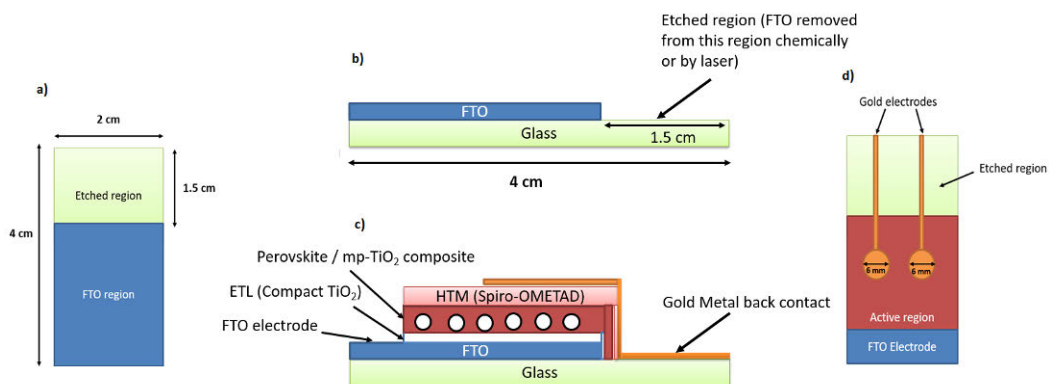


Fig 14. Architecture of the devices used in this thesis: (a) Etched FTO glass (top-view with dimensions for each region), (b) side-view of the etched FTO glass substrate, (c) side-view of a complete device, and (d) top-view of the complete solar cell sample with two circular gold contacts (i.e., two devices) each with 6 mm in diameter.

4.3. Device preparation

In this work, compact and mesoporous TiO₂ films were prepared and their contribution to the performance of PSCs when incorporated into the device was investigated. In the first study, I focused on electron-selective layers based on compact TiO₂ films deposited via the dip coating method from a colloidal sol using TiCl₄ as the precursor. The goal was to determine the minimum thickness needed to obtain pinhole-free compact TiO₂ films. In the second study, mesoporous TiO₂ scaffold was exposed to two different surface activation methods (i.e., UV irradiation and oxygen plasma treatment) to systematically study their influence on the performance of mesoscopic PSCs. In the third study,

ordered mesoporous TiO₂ films were synthesized using block co-polymers as structure directing agents and were used as model systems to study the effect of pinholes in the compact TiO₂ layers.

Etching of fluorine-doped tin oxide substrates

FTO layer was removed from the denoted areas either by laser etching or chemical etching (see Figure 13). The area of the etched region was kept around 2 cm x 1.5 cm from one side. For TCO22-7 FTO substrates (used in the first study), I opted for the laser etching facility available at Aalto University, Espoo, Finland. A Cencorp 300 LM setup was used with a 20 W Ytterbium fiber laser. The operational parameters were: speed 500 mm/s, power 10%, frequency 20 KHz, and line spacing 25 μ m.

Chemical etching was performed for the TCO22-15 FTO substrates in studies 2 and 3 because they were found to be easily etched chemically in comparison to TCO22-7. It was done by spreading zinc powder over the region to be etched (while covering the rest of the FTO region with Kapton tape). A 4 M HCl solution was dropwise placed on the zinc powder. The zinc powder reacts with the HCl, which is evident from the generation of hydrogen gas bubbles. The zinc powder ionizes and gives part of its electrons to H⁺ ions from the HCl to form H₂ gas, while the rest of electrons are utilized in reducing H₃O⁺ ions to H atoms, which are able to diffuse into the FTO lattice and reduce Sn⁴⁺ ions to metallic tin.

The etched substrates were then sonicated at room temperature in a 2% aqueous Hellmanex III solution, deionized water, acetone, and 2-propanol for 11 min each. The substrates were then plasma-treated for 5 minutes before performing the dip coating of the compact TiO₂ layer.

4.3.1. Compact TiO₂ film preparation

The dip coating sols used for the preparation of the compact TiO₂ used in the first and second studies were made the following way:

18.97 g of TiCl₄ was added dropwise to 23.04 g of ethanol while stirring on an ice bath. Another solution containing 13.44 g of ethanol, 0.21 g of water, 1.72 g of THF and 15.2 mg of Pluronic F127 block co-polymer was prepared under ambient conditions. 0.5 g of the first stock solution (TiCl₄/ethanol) was added into the second one. The final solution resulted in a TiO₂ film with the thickness of about 5 nm. Thicker films were prepared by increasing the molar ratio of TiCl₄ in the final solution while keeping the amounts of the other species constant. The molar ratios of the species in different sols used in study 1 and their corresponding names are given Table 1:

Table 1. Molar ratios of the sols to prepare dense TiO₂ layers with varying thickness.

Sol	TiCl ₄	EtOH	water	THF	Pluronic F127
[mol]					
TiCl ₄ -1	1.0	250.0	9.8	20.0	1.0·10 ⁻⁴
TiCl ₄ -2	2.0	250.0	9.8	20.0	1.0·10 ⁻⁴
TiCl ₄ -3	3.0	250.0	9.8	20.0	1.0·10 ⁻⁴
TiCl ₄ -5	5.0	250.0	9.8	20.0	1.0·10 ⁻⁴
TiCl ₄ -7	7.0	250.0	9.8	20.0	1.0·10 ⁻⁴

The TiCl_4 sol was used to produce the compact TiO_2 layer in study 2 and 3. The substrate were dip-coated with an 85 mm/min withdrawal speed at a relative humidity lower than 35%. In order to avoid film deposition on the back side of the substrate and in the anode region, these areas were marked with kapton tape. The substrates were then dried on the hot plate for 10 min at 120 °C and then transferred to an oven for calcination at 500 °C for 30 min.

The compact TiO_2 solutions used for the third study were slightly different in chemical composition and were prepared using a modified protocol reported by Ortel et al.²⁰² The commercially available poly (butadiene-b-ethylene oxide) di-block co-polymers were used as templates instead of the self-synthesized tri-block co-polymers described by Ortel et al.

10 g of TiCl_4 was added to 50 ml of ethanol while stirring on an ice bath. Furthermore, different solutions with or without the organic templates were prepared in a mixture of ethanol and water. This was done by dissolving the required amounts of P2952-PBdEO di-block co-polymers in the ethanol/water solution by stirring at 67 °C overnight. The required amounts of the first solution was then added dropwise into the second one to prepare sols for making the porous compact TiO_2 thin films (Tables 2). The goal was to tune the porosity while keeping the same thickness or to change the thickness while using the same porosity of TiO_2 films. By changing the P2952-PBdEO molar ratio with respect to the TiCl_4 precursor while keeping the same amount of other species in the final solution, we wanted to change the porosity of the TiO_2 film without changing other parameters (such as the film thickness). The solvent (ethanol/water) content was changed to tune the thickness. In this way, TiO_2 films with same porosity and different thickness were prepared. For the porosity series, the sol names were designated as Ti-x, where the values of x were the P2952_BdEO/ TiCl_4 molar ratios. For the thickness series, the sol names were designated as Ti-21-y, where y parameter indicates the relative amount of solvent (i.e., H_2O and ethanol) in comparison to the original Ti-21 sample.

Table 2. Molar compositions for dip coating sols for compact TiO_2 used in Study 3.

Sol/Sample	TiCl_4	EtOH	H_2O	P2952_BdEO
Porosity series				
Ti-0	1	32.5	8.4	0
Ti-6	1	36.6	9.5	5.88×10^{-6}
Ti-12	1	48.5	12.6	11.8×10^{-6}
Ti-21	1	67.9	17.6	21.2×10^{-6}
Thickness series				
Ti-21-0.8	1	56.2	14.6	21.2×10^{-6}
Ti-21-1	1	67.9	17.6	21.2×10^{-6}
Ti-21-2.5	1	169	43.7	21.2×10^{-6}

The dip coating was performed with the same withdrawal speed as before (i.e., 85 mm/min), but the relative humidity was lower (between 14% and 20%). Then the films were allowed to dry in the dip chamber at the same humidity range for 10 min before being transferred to the oven for calcination. The calcination was performed by first heating the films at 80 °C for 4 h followed by the temperature increase to 475 °C with 1 °C/min heating rate. The films were kept at 450 °C for 15 min before allowing them to cool down to 150 °C in the oven. The samples were then either immediately transferred to nitrogen containing glovebox for further processing such as device preparation or alternatively they were characterized to understand the structure of these nanostructured TiO₂ films.

In order to characterize the various compact TiO₂ films using x-ray reflectometry (XRR), the solutions mentioned in table 1 and 2 were dip-coated on the microscope glass substrates. For XRD, XPS and other characterization, films were deposited on FTO/glass substrates. This will be further discussed in section 4.5.

4.3.2. Mesoscopic TiO₂ scaffold

In the first and second study, thin film mesoscopic scaffolds with TiO₂ nanoparticles as building blocks were used. For this purpose, 30 NR-D paste was diluted in ethanol to make a 150 mg/ml dispersion. Thus, this is a suspension of 30 nm-sized TiO₂ nanoparticles in ethanol. The dispersion was deposited by spin coating at 4000 rpm for 10 s.²⁰³ Calcination was performed at 450 °C for 30 min according to the following heating protocol:

$\xrightarrow{20\text{ }^{\circ}\text{C/min}}$ **125 °C (5 min)** $\xrightarrow{13.3\text{ }^{\circ}\text{C/min}}$ **325 °C (5 min)** $\xrightarrow{10\text{ }^{\circ}\text{C/min}}$ **375 °C (5 min)** $\xrightarrow{15\text{ }^{\circ}\text{C/min}}$ **450 °C (30 min)**

Afterwards, these substrates were allowed to cool down to 150 °C inside the oven and then they were directly transferred to a nitrogen-filled glovebox. In the second study, where the surface activation of the mesoporous TiO₂ films was in focus, the samples were transferred to the glovebox after the plasma or UV light treatments.

Surface activation of particle-based 30 NRD mesoporous films prior to perovskite deposition (in study 2):

In the second study of this thesis, the effect of surface activation of the mesoporous TiO₂ scaffold layer on the device performance and on the quality of the perovskite layer prepared from 2-step sequential deposition method was investigated. The compact TiO₂ layer was prepared from the TiCl₄-5 sol mentioned in Table 1.

After annealing the mesoporous TiO₂ films, some of the samples were immediately transferred to the glovebox without any surface activation (denoted as “non-treated”). The rest of the samples were either exposed to plasma treatment or UV irradiation. The plasma treatment was performed for 5 min under low pressure using a Harrick PDC-32G plasma cleaner at medium level. For the UV activation, the samples were exposed to the UV light in air for 20 min (at a relative humidity of about 20%) using a Mineralight UVS-11E UV lamp with λ_{max} at 254 nm. Thereafter, the samples were transferred to the glovebox for perovskite deposition.

4.3.3. Organo-lead halide perovskite deposition

In this work, two different ways of fabricating the organo-lead halide perovskite light absorber layer were used.

a. 2-step sequential deposition (MAPbI₃)

In the two-step sequential deposition method, a PbI₂ (or any other Pb-based) precursor film is first deposited. After drying, the film is exposed to methylammonium iodide so that the PbI₂ reacts with MAI to form MAPbI₃. This is either done by dispensing MAI solution on top of the spinning PbI₂-coated substrate or by dipping the entire substrate into MAI solution followed by removal of excess amount of MAI.⁶⁹

In this work, a 1 M solution of PbI₂ in anhydrous DMF was prepared by stirring at 100 °C for at least 2 h to ensure complete dissolution. The solution was spin-coated on top of mesoporous TiO₂ substrates at 6000 rpm for 30 s with a spin acceleration of 6100 rpm/s. The substrates were then annealed at 100 °C for 30 min on a hot plate. The samples were then allowed to cool down to room temperature and then dipped in a 10 mg/mL solution of methylammonium iodide in anhydrous 2-propanol for 1 min. Immediately after dipping in the MAI solution, the yellow-colored PbI₂ film is converted into light brown color, which indicates the reaction of PbI₂ with MAI to form the MAPbI₃ perovskite. The samples were then rinsed in 2-propanol to remove excess MAI and then dried on a hot plate at 100 °C for 30 min. The mesoporous TiO₂ layer infiltrated with perovskite is about 150 nm thick, while the capping layer is expected to be about 70 nm thick.

The two-step sequential deposition was used in Studies 1 and 2. However, in our third and fourth studies, we switched to the 1-step mixed triple cation method.^{111, 120} The reasons for this will be discussed in the results and discussion section.

b. 1-step mixed ion perovskite via the anti-solvent approach

The mixed ion perovskite precursor solutions contain a mixture of FAI (1 M), MABr (0.2 M), PbI₂ (1.1 M), and PbBr₂ (0.2 M) in an anhydrous DMF:DMSO solvent mixture based on a 4:1 volume ratio. 5 vol-% of the perovskite solution was adjusted with pre-prepared 1.5 M CsI solution in DMSO to form triple cation perovskite. The CsI solution was not used in study 3 where the ordered mesoporous TiO₂ films were tested as scaffolds.

The perovskite solution was spin-coated at 1000 and 6000 rpm for 10 and 20 s, respectively. During the second step, 200 µL of chlorobenzene was pipetted on the spinning substrate 5 s prior to the end of the program. The films were then annealed at 100 °C for 30 min inside the glovebox.

Some of the samples were characterized by X-ray diffraction (XRD), Ultraviolet-Visible spectroscopy (UV-Vis), steady-state photoluminescence (SSPL), and time-resolved photoluminescence (TRPL), while others were converted to solar cells by depositing the HSL layer and the gold metal back contact on top of them.

4.3.4. Hole-selective layer

70 mM solution of spiro-OMeTAD was prepared in chlorobenzene followed by further dilution with 4-tert-butylpyridine (4-TBP) so that molar ratio between spiro-OMeTAD and 4-TBP is 1:3.3. Li-TFSI and FK 209 Cobalt (III) stock solutions were prepared in acetonitrile with 1.8 and 0.25 M concentrations, respectively. The required amount of these stock solutions were added into the spiro-OMeTAD solution to obtain a spiro-OMeTAD: Li-TFSI: FK 209 Co (III) TFSI: 4-TBP: chlorobenzene: acetonitrile molar composition of 1.0 : 0.5 : 2.5×10^{-2} : 3.3 : 131.5 : 7.2. The final solution was stirred to ensure complete dissolution and then spin-coated at a speed of 4000 rpm for 20 to 30 s.⁶⁹

4.3.5. Gold back contacts

A 60-80 nm gold film was deposited as a back contact on top of the spiro-OMeTAD layer. The evaporation was performed in vacuum at 2.5×10^{-5} bar with an evaporation rate of 0.1 \AA/s . Masks with a circular opening with a diameter of 6 m were used to produce the 0.28 cm^2 gold contacts. The evaporation chamber has been installed inside the glovebox. The base with feedthroughs of the evaporator has been purchased from JEOL, while rest of the setup has mostly been made in-house.

4.4. Characterization methods

PSCs comprise of several different layers as discussed in section 4.2. The most reliable and widely used method to characterize solar cells is to perform current-voltage scans; first in the dark and then under illumination. However, if the device does not perform as expected, it is difficult to determine which layer is causing the problem. Therefore, each layer must be carefully inspected before manufacturing the device. Secondly, if one layer is to be studied or optimized, then one must be confident about the rest of the layers. It is also possible that changing a parameter of the studied layer might influence the subsequent layer. For instance, in the second study, the activation of the mesoporous TiO_2 scaffold by plasma and UV light exposure affected the quality of the perovskite which had a direct influence on the device performance. Thus, a wide variety of characterization techniques have been employed to investigate the electron-selective layer and the quality of the subsequent organo-lead halide perovskite layer. These methods are explained below:

4.4.1. X-ray reflectometry

The working principle of x-ray reflectometry (XRR) is shown in Figure 15. X-rays are directed at a low angle onto the surface of the film, which is coated upon a very smooth substrate. Some of the x-rays are reflected from the surface of the film (air/film interface), while the rest of the x-rays are able to penetrate through and reach the film/substrate interface, where they again encounter a difference in refractive index, and are reflected. The x-rays reflected from the film/substrate interface combine with those being reflected from the surface of the film and undergo constructive and destructive interference at different Bragg angles as shown in Figure 15. The measured interference patterns are matched with simulated ones to determine different film parameters such as thickness, density and surface roughness.

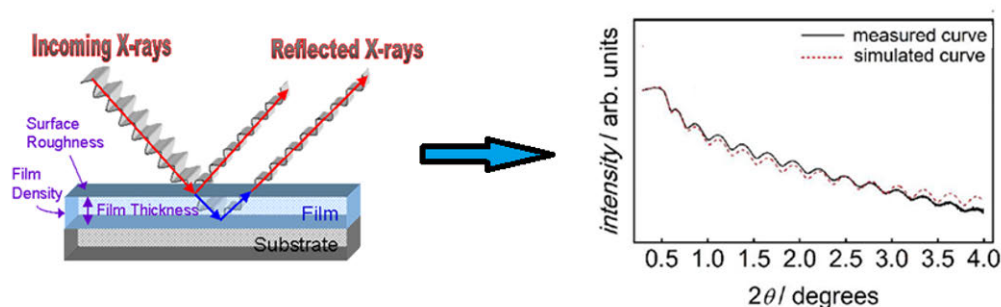


Fig 15. The working principle of XRR and the signals generated by the reflected x-rays giving rise to the alternating crests and troughs corresponding to constructive and destructive interference between the reflected x-rays from the upper surface of the film and its interface with the planar substrate.²⁰⁴

It is important that the film to be studied using XRR is coated on very smooth substrates such as silicon wafers or planar glass slides. If the substrate surface is very rough, no interference patterns will be observed because the x-rays will not be uniformly reflected. Furthermore, it is also important that the refractive index of the substrate is different from that of the film; otherwise no interference patterns will be observed.

4.4.2. Grazing incidence x-ray diffraction

The grazing-incidence x-ray diffract (GI-XRD) is used to determine structural features of a crystalline material such as atomic or molecular arrangement in specific crystallographic planes. The working principle of x-ray diffraction (or XRD) is based on Bragg's law:

$$n\lambda = 2d\sin\theta$$

where n is an integer, λ is the wavelength of incident x-rays, d is the distance between two parallel crystallographic planes, and θ is the angle of incidence of the x-rays.

The crystalline material is irradiated with a monochromatic x-ray beam at different Bragg's angles. X-rays reflected from crystallographic planes display constructive interference when irradiated at an angle satisfying Bragg's law.

Generally, XRD is used to measure distances between crystallographic planes in order to determine the crystal structure of an unknown material. It can be used to determine the orientation of a single crystal and measure the (approximate) size, shape and internal stress in small crystalline regions.

The grazing incidence x-Ray diffraction (GI-XRD) mode is used to study the crystallinity of thin films with thicknesses between 50 nm to 2 μm . Typically, the angle of incidence in GI-XRD ranges from 0.2 to a few degrees in order to determine the structure close to the film surface. In this work, both the XRR and GI-XRD measurements were performed with a Bruker D8 Discover instrument (Bruker-AXS, Karlsruhe, Germany) by using Cu K α radiation ($\lambda = 1.54184$ nm). The PDF-2 database (2010) was used to identify the crystalline phases.

4.4.3. X-ray photoelectron spectroscopy

The possible presence of pinholes in compact TiO₂ films of different thicknesses was investigated using x-ray photoelectron spectroscopy (XPS). XPS is a surface-sensitive technique with the probing depth of about 5 to 10 nm.^{205, 206}

Soft x-rays are produced by bombarding a metallic anode with high energy electrons. The sample is irradiated with these soft x-rays under ultra-high vacuum. The energy of the soft x-rays depends on the kind of metal anode used, magnesium (Mg K α , photon energy 1.2537 meV) or aluminum (Al K α , photon energy, 1.4866 meV). The interaction of the x-rays with the sample results in the emission of photoelectrons from the surface of the sample. The number and the kinetic energy of the emitted electrons are detected and converted into binding energy (BE) according to the following equation:

$$BE = h\nu - \phi_s$$

The $h\nu$ is the energy of the incident x-rays while ϕ_s is the work function (i.e. the energy difference between the Fermi level and the vacuum level) of the material under observation. The binding energy is characteristic for each element in the sampling volume.

The XPS analysis in this work was performed with a Physical Electronics Quantum 2000 scanning spectrometer with a monochromatic Al K α X-ray source (1.4866 meV). An electron flood gun and a low energy ion gun were used for charge compensation. The position of the detector was at a 45 ° angle with respect to the sample surface. The atomic percentage of elements was determined by calculating the area of the peaks and correcting for the sensitivity factors (using MultiPak v6. 1A from Physical Electronics).

4.4.4. Atomic force microscopy

An atomic force microscope (AFM) comprises of a probe based on a cantilever having a sharp tip at one of its ends. The radius of curvature of the tip is on the order of nanometers. When the tip approaches the sample surface, attractive and repulsive forces between the tip and surface results in the deflection of the cantilever. The deflection of the cantilever can be used to create a 3D image if it is carefully monitored. A laser beam is used to monitor this deflection with the help of a photodiode detector.

There are several imaging modes for AFM, including the contact, non-contact, and tapping modes. In the contact mode, the tip makes a direct contact with the surface under observation. However, it can damage the surface or the tip itself. In non-contact mode, the probe just moves over the sample without physically touching the surface such that the attractive and repulsive forces between the tip and the surface result in a deflection of the cantilever. Since the forces are much weaker than in the contact mode, there is some compromise in the image quality. On the other hand, the tapping mode is somehow a combination of the contact and non-contact modes. The oscillating tip makes a very brief contact with the surface and therefore high resolution images can be generated without damaging the surface or the tip.²⁰⁷

In this thesis, an NTEGRA Prima AFM instrument using tapping mode to study the surface roughness and topography of compact TiO₂ films coated on FTO glass substrates. The Scanning Probe Image Processor (SPIP, image Metrology, DK) software was used to analyze the topographical images and the surface roughness.

In this work, following roughness parameters were given prime importance to understand the texture of bare FTO substrate and subsequently the change in texture upon depositing compact TiO₂ layers of different thickness:

S_q = Root mean square (RMS) height which is the standard deviations of the height profiles

S_{dr} = Surface area contributed by the texture as compared to the planar surface

V_v = Void volume

4.4.5. Ultraviolet-visible light spectroscopy

Ultraviolet-visible light spectroscopy (abbreviated as UV-Vis) gives the measurement of light absorption due to electronic transitions within the sample. UV-vis spectroscopy is based on the principle of the Beer-Lambert law which states that the amount of light absorption by any given solution depends on its concentration and the path length. Therefore this method is primarily used for quantitative measurements of solution concentrations. The Beer-Lambert law is given by the following equation:

$$Abs = \log_{10} \left(\frac{I_0}{I} \right) = \epsilon cL$$

where Abs is the light absorption by the sample, I_0 is the intensity of the incident beam and I is the intensity of transmitted light beam. ϵ is a constant called molar absorptivity (or extinction coefficient), while c is the concentration of the solution and L is the path length. Besides measuring solutions, the same UV-vis technique can also be applied to thin film semiconductors to understand their optical characteristics.²⁰⁸ The intensity of the transmitted light can be plotted as a function of the wavelength of light. The optical properties of thin films are the combination of transmittance (T), reflectance (R), and absorptance (A) as follows:

$$T + R + A = I_0$$

When a light beam passes through a thin film, part of it is scattered and absorbed by the film and/or the substrate. If the surface of the film is very rough, the light is expected to reflect in all directions and therefore in some cases it would be better to consider absorptance (A) of the sample instead of absorption (Abs):

$$A = \frac{100 - T - R}{100}$$

In this work, the reflectivity was not taken into account, because the UV-vis absorption was performed only to determine the relative trends in the light absorption (in visible range) by perovskite and PbI_2 coated TiO_2 samples as a function of certain parameters (such as type of surface activation technique and porosity of ordered mesoporous TiO_2 substrates).

The UV-vis set up was also used to perform dye degradation test in Study 2. This test was performed to investigate the effective depth of surface activation performed (via oxygen plasma or UV light) upon mesoporous TiO_2 layers. The mesoscopic TiO_2 layers deposited on top of c- TiO_2 /FTO/glass substrates were loaded with ruthenium N719 dye. Thereafter, the samples were activated by UV light or oxygen plasma. The details about the surface activation protocol have been discussed in section 4.3.4.

4.4.6. Scanning electron microscopy

The light used in an optical microscope has a wavelength in the range of 400 to 700 nm,²⁰⁹ while electron microscopes utilize a high energy electron beams having a wavelength on the order of 0.05 nm.²¹⁰ Therefore, a much higher resolution can be achieved in the electron microscope to study very fine details in a sample.

The scanning electron microscopy (SEM) technique utilizes a high energy electron beam directed onto a conducting sample. The electrons in the high energy beam are called primary electrons (PE), which result in the production of secondary electrons being knocked out of the sample as a result of the Compton effect. These secondary electrons (SE) are collected by a detector and used to produce the image of the sample with a high resolution. Some of the primary electrons are reflected (or so called back scattered) out of the specimen interaction volume. These electrons are back-scattered as a result of elastic interactions of primary electrons with the specimen atoms. These electrons are called back-scattered electrons (BSE) which can be used to detect contrast between regions with different chemical compositions.²¹¹

In this work, all the samples were either semiconductors (such as TiO₂ or organolead halide films) or insulating PbI₂ over mesostructured TiO₂, therefore graphite was coated over the surfaces to make them conductive for the electron beam. The SEM used in these studies was a Leo 1530 Gemini (Zeiss, Germany).

4.4.7. Water contact angle measurements

Water contact angle measurements were carried out in order to investigate the effect of plasma and UV treatment on the wettability of mesoscopic TiO₂ film surface.

Fig 16 shows the contact angle θ_y and the respective interfacial tensions (γ) of a liquid droplet with respect to a given substrate. The relationship between the interfacial tensions and the contact angle is given by Young's equation:²¹²

$$\gamma_{SV} = \gamma_{LV} \cos \theta_y + \gamma_{SL}$$

γ_{SV} is the solid-vapor interfacial tension, γ_{LV} is the liquid-vapor interfacial tension, and γ_{SL} is the solid-liquid interfacial tension. The solid surface displays a high wettability if the γ_{SL} is high and/or θ_y is low.

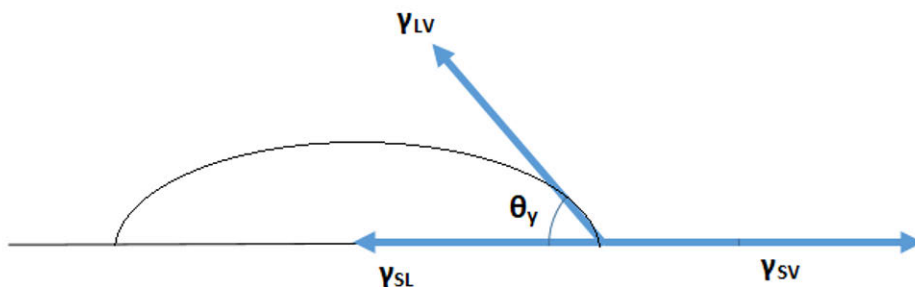


Fig 16. A liquid droplet on a solid surface with respective interfacial tensions.

The contact angle defines the wettability of a solid surface, i.e. lower contact angle θ_y means higher wettability and vice versa. TiO₂ is prone to the adsorption of organic species in the environment, which can reduce the wettability of its surface.

In this work, water contact angles were measured as a function of time using a KSV CAM 200 optical goniometer (KSV instruments Ltd., Helsinki, Finland). For each measurement, 2 μ L droplets of Milli-Q-purified water were deposited by a micro-syringe after different surface activation methods applied on mesoporous TiO₂ films. The measurements were repeated three times, which provided the statistical data for analysis.

4.4.8. Photoluminescence spectroscopy

The photoluminescence spectroscopy (PL) technique is a non-destructive evaluation technique to understand the electronic band structure of a material. Monochromatic light is directed onto a sample where it is absorbed by the material due to excitation of electrons to higher energy states. The absorbed energy is dissipated as emission of light from the same material. Photoluminescence can be of three different types:

a. Resonant radiation

The photon of a particular wavelength when directed on the sample is absorbed and then the photon of the same energy is immediately emitted with no significant internal energy transitions. This process is very fast and takes place within nanoseconds.

b. Fluorescence

The absorbed energy is dissipated in the form of some internal energy transitions like phonons and similar lattice vibrations. The rest of the energy is released in the form of a photon with lower energy than the incident photon. This process has a very short lifetime, i.e., it takes place within 10^{-8} to 10^{-4} s.

c. Phosphorescence

In phosphorescence, the energy absorbed by the material undergoes intersystem crossing into a state with different spin multiplicity, usually a triplet state. The lifetime of this process is relatively longer, i.e., ranging from 10^{-4} to 10^{-2} s, or even up to hours.²¹³

Organo-lead halides can be considered as fluorescent materials because they absorb photons of a certain energy and then release the photons at a higher wavelength, because part of the absorbed energy is released in the form of non-radiative phonon transitions.

Photoluminescence (PL) spectroscopy was performed on perovskite materials prepared by 2-step method to get a qualitative confirmation of the relative amounts of perovskite versus PbI_2 materials.

Steady-state photoluminescence (PL) spectroscopy was performed using FLS1000 spectrofluorometer (Edinburgh Instruments, UK), with 600 nm excitation wavelength. The scan was performed between 625 to 900 nm with a rate of 200 nm/min and the slit width of 3 nm.

The time-resolved PL decays were determined by using a time-correlated single photon counting (TCSPC) apparatus equipped with a PicoHarp 300 controller and a PDL 800-B driver for excitation and a Hamamatsu R3809U-50 microchannel plate photomultiplier for detection in 90° configuration. All the samples were measured by using a 648 nm excitation wavelength while exciting from perovskite film side. The PL decays were monitored at 765 nm.

4.4.9. Device characterization by current density versus voltage measurements

A photovoltaic cell is a device which absorbs photons upon solar irradiation due to electronic transitions within the light absorbing material (such as organo-lead halide perovskite or an organic dye). If the device is connected to an external circuit, the excited electrons might be transferred to the external circuit to generate a current. Figure 17 shows a typical current-voltage (I-V) curve for a solar cell. During irradiating the device with sunlight, the voltage is scanned while the generated current is monitored. First, the device is short-circuited, meaning that the device is in a similar situation as if its positive and negative terminals would be directly connected to each other via an external circuit or when the voltage is zero across the terminals. In this condition, the highest possible current (called the short-circuit current, I_{sc}) can pass through the external circuit. On the other hand, when the two terminals are disconnected or the so called open circuit condition, a zero current across the external circuit. This happens at the voltage called open circuit voltage (or V_{oc}). When the product of I and V (i.e., the power output) is plotted against the voltage, a maximum in power output can be found somewhere in between the short circuit and the open circuit conditions, which is called the maximum

power point. This maximum power point output, P_{\max} (which is the product of I_{MP} and V_{MP} , see Figure 17) can be used to calculate the efficiency of photovoltaic device according to the following equation:

$$\text{Device Efficiency} = \frac{\text{Maximum Power Output}}{\text{Solar irradiance (Power input)}} \times 100\%$$

The solar irradiance is the power input of the solar light being directed on to the photovoltaic device. The solar irradiance (or power density input) from the light source of a solar simulator is calibrated to be 100 mW/cm^2 , which is the standard lab-scale solar intensity for characterizing solar cells. The power output is generally given in the form of power density (in mW/cm^2), obtained by converting the current in amperes to current density (J) in mA/cm^2 .

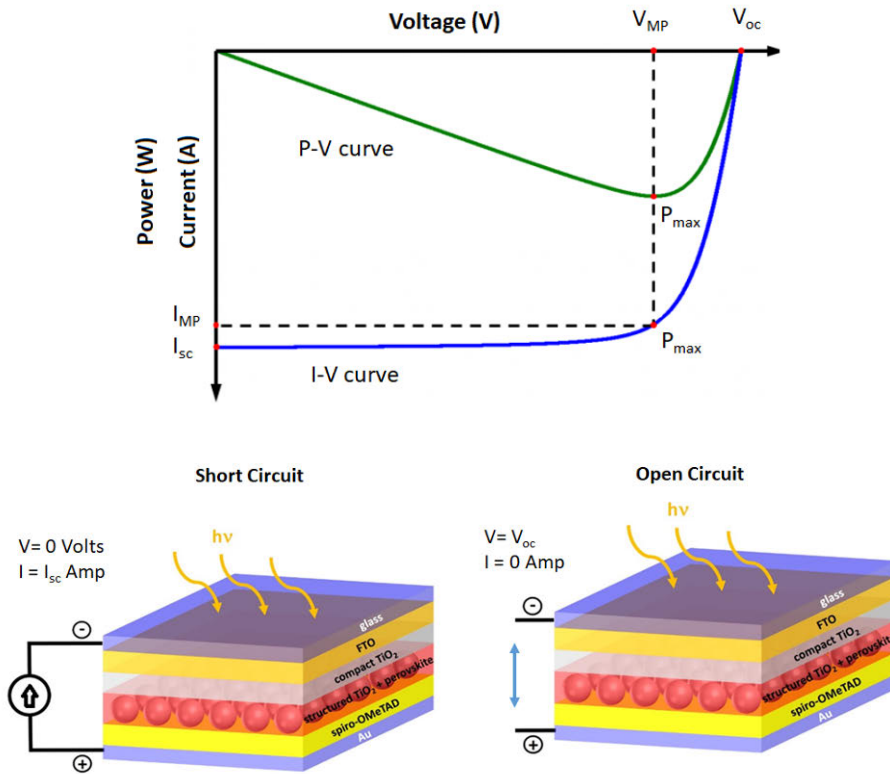


Fig 17. The I-V curve shown is a typical curve for a solar cell under 1 Sun illumination and indicates the different photovoltaic parameters, which can be used to quantify the performance of a photovoltaic cell. The short circuit and open circuit conditions are the two extreme conditions in between which a maximum power point lies, which determines the efficiency of the photovoltaic device.²¹⁴

Another important device parameter that is used to describe the photovoltaic performance is the fill factor (FF). The values of FF can be calculated using the following equation:

$$FF = \frac{\text{Maximum Power Output}}{(J_{sc} \times V_{oc})}$$

In very simple words, the fill factor is a measure of how close the experimental J-V curve (under illumination) is to a perfect rectangle having J_{SC} and V_{OC} as its coordinates. The value of FF for an Ideal J-V curve with a perfect rectangular shape would be equal to 1. Therefore, the values of FF lie between 0 and 1.

The solar cells were characterized by measuring the current density against voltage (J-V) curves using 2636 Series Source Meter (Keithley instruments) under simulated AM 1.5 sunlight close to 100 mW/cm² irradiance using an Oriel class ABB solar simulator (150 W, 2" × 2"). The devices were masked (with an aperture of 0.126 cm²) and scanned in forward and reverse sweep between -1 to 1.5 V (study 1) or -0.3 to 1.2 V (for studies 2, 3 and 4). The scan speed was 10 mV/s.

4.4.10. Surface recombination measurements using dark MIS CELIV

MIS-CELIV was performed to investigate the hole blocking ability of the compact and ordered mesoporous TiO₂ films used in the third study for this thesis. A possible reduced hole blocking ability could be an indication that the FTO conductive substrate protrudes through the TiO₂ film in some places.

The CELIV method (i.e., charge extraction by linearly increasing voltage) was first introduced by Juska et al²¹⁵ to evaluate the drift charge mobility and bulk conductivity for highly conductive materials such as microcrystalline hydrogenated silicon ($\mu\text{c-Si:H}$). Thus, highly conductive materials that do not follow the limitations imposed by time of flight (TOF) measurements can be evaluated by CELIV. MIS-CELIV²¹⁶ (i.e., metal-insulator-semiconductor-CELIV) has been used to selectively determine the hole or electron mobility in different materials. In photo-CELIV or MIM-CELIV, the identification of the sign of majority carriers is difficult in bi-polar semiconductor devices. In other words, it is not possible to distinguish whether the current peak in the CELIV current transient is due to holes or electrons and therefore it is not easy to assign the calculated charge transport properties such as charge mobility to any one type of the charge carrier.

Some research groups have investigated metal-insulator-semiconductor devices to selectively study the charge transport properties for electrons.^{216, 217} In this work, MIS-CELIV was utilized to understand the hole blocking ability of compact and ordered mesoporous TiO₂ films used in study 3.

Upon applying an offset voltage, holes are induced from the gold contact into Poly (3-hexylthiophene-2,5-diyl), (which is also called P3HT) organic semiconductor. If the compact TiO₂ layer is ideally blocking, then the magnitude of dark current is nearly zero. Subsequently, a linearly increasing voltage is applied. The polarity of the linearly increasing voltage is then reversed (see Figure 18b) to extract the free charges (which were originally induced by applying the offset voltage). The linearly increasing voltage creates a displacement current plateau (indicated as j_o in Figure 18 c). The extracted free charges appears as an additional current peak on top of the displacement current plateau. Charge transport properties such as hole mobility and conductivity depend upon the difference between j_{MAX} and j_o .

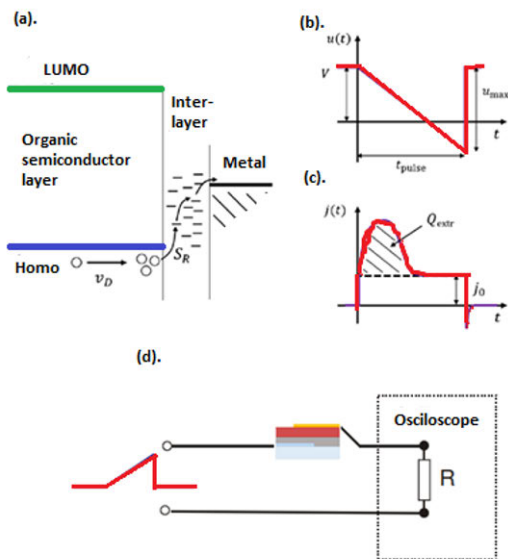


Fig 18. (a) Energy level diagram showing holes induced from one side of the organic conductor while they are being blocked from the other end. (b) Applied offset and linearly increasing voltage with reverse polarity. (c) The current transient as a result of the applied linearly increasing voltage in reverse bias. (d) The circuit used in this work to carry out the MIS-CELIV measurements.²¹⁸

The dark current in the current transient corresponds to the current through the device upon application of the offset voltage. The holes induced into the P3HT layer upon the application of the offset voltage reach the P3HT/TiO₂ interface under the influence of the built-in voltage. If the TiO₂ is capable of blocking the holes from reaching the FTO, then the magnitude of the dark current would be nearly zero. Upon further increase in the offset voltage, the increase in the dark current would not increase so significantly unless the TiO₂ layer contains pinholes (or exposed FTO patches through the TiO₂ film). In that case, the magnitude of the dark current is expected to drastically change due to the leakage through the compact layer. The pinholes will also reveal themselves in the form of leakage currents in the transient after some time.

5. Results and discussion

5.1. Optimization of ultrathin dip-coated compact TiO₂ film thickness by tuning the molar concentration of TiCl₄ precursor in the initial sol (Study 1)

In the first study of this thesis, the performance of mesoscopic PSCs utilizing ultrathin dip-coated compact TiO₂ layers was studied as a function of the layer thickness (between 5 to 50 nm). The aim was to determine the minimum thickness of the compact TiO₂ layer when pinholes are completely eliminated. Titanium tetrachloride (TiCl₄) was chosen as the TiO₂ precursor instead of the most widely used titanium iso-propoxide (TTIP), because it has previously been shown that TiCl₄-based compact TiO₂ ESLs have superior performance, less hysteresis, and a high stability.²⁰³ This is because the TiCl₄ precursor tends to form highly dense compact TiO₂ layers which is ultimately beneficial for efficient extraction of the photo-generated electrons from the perovskite active layer. The produced compact TiO₂ films were thoroughly studied using XRD, XRR, AFM and XPS. These results were found to be very useful to understand the trends in device performance when the compact TiO₂ layers of different thickness were incorporated into solar cells.

Before moving on to the results, it is worth reminding some details mentioned in section 4.3.2; the precursor sols for compact TiO₂ films are named on the basis of the TiCl₄ molar concentration, for example TiCl₄-1, TiCl₄-2, and so on (where 1 and 2 are the molar concentrations of TiCl₄ precursor in the sols). The corresponding compact TiO₂ films after calcination are named as TiO₂-1, TiO₂-2, and so on. The reference samples or devices without any compact TiO₂ layers are labelled TiO₂-0.

5.1.1. Crystal structure, thickness and densities of compact TiO₂ films

Figure 19 (a) shows the XRR interference patterns for TiO₂ films prepared from sols with different molar concentration of TiCl₄ precursor. The films for XRR analysis were prepared on top of planar microscope glass substrates. The number of interference patterns increases while the distance between each node decreases with increase in the TiCl₄ precursor concentration. The information obtained from the XRR measurements is summarized in Figure 19 (c). With a gradual seven-fold increase of the TiCl₄ concentration, the thickness of the compact TiO₂ film increases almost linearly from 5 to 48 nm. The slight deviation from linearity is likely due to the higher viscosity of the dip coating solutions with higher precursor concentration. It is worth mentioning that the thicknesses of the corresponding compact TiO₂ films prepared on top of FTO substrates might be slightly less uniform due to the higher surface roughness compared to glass substrates. This will be discussed in section 5.1.2 where the topographical AFM images of TiO₂ films coated on FTO glass are discussed in detail. Furthermore, upon increase in TiO₂ film thickness, the film density decreases from 3.73 g/cm³ to 3.36 g/cm³. The values are lower in comparison to the ideal bulk density of TiO₂ anatase which is 3.79 g cm⁻³.²¹⁹ This could be due to defects (such as pores, structural disorder, or vacancies) that are generated due to thermal shrinkage during the calcination or due to the nanocrystalline nature of TiO₂ structure.²²⁰ Interestingly, TiO₂ films prepared from TiCl₄ precursor are generally denser than films prepared from other precursors¹²³ which can be beneficial to fabricate pinhole-free TiO₂ films and, thus, good performing PSCs can be prepared with ultrathin TiO₂ ESL.

Figure 19 (b) shows the grazing incidence X-ray diffraction (GI-XRD) diffractograms of FTO substrates coated with TiO₂ layers with different thicknesses. The FTO substrate without TiO₂ film (TiO₂-0) shows

4 reflections, which can be matched to tetragonal SnO_2 (JCPDS 072-1147). Similar diffractograms can be observed for FTO substrates coated with thin compact TiO_2 films (i.e., TiO_2 -1, TiO_2 -2, and TiO_2 -3). As no additional reflections have appeared, this suggests an amorphous nature of the thinner compact TiO_2 films. However, a diffraction peak at 25.5° starts to appear for the TiO_2 -5 sample. For the TiO_2 -7 sample, the intensity of this reflection is even higher. This peak corresponds to the (101) reflection plane in tetragonal anatase TiO_2 (JCPDS 03-065-5714). Thus, some critical film thickness must be reached before crystalline TiO_2 starts to form. The crystallite size was calculated from the full-width half-maximum of the (101) peak using the Scherrer equation, which reveals that the crystallite size is about 20 nm for both the TiO_2 -5 and TiO_2 -7 samples.

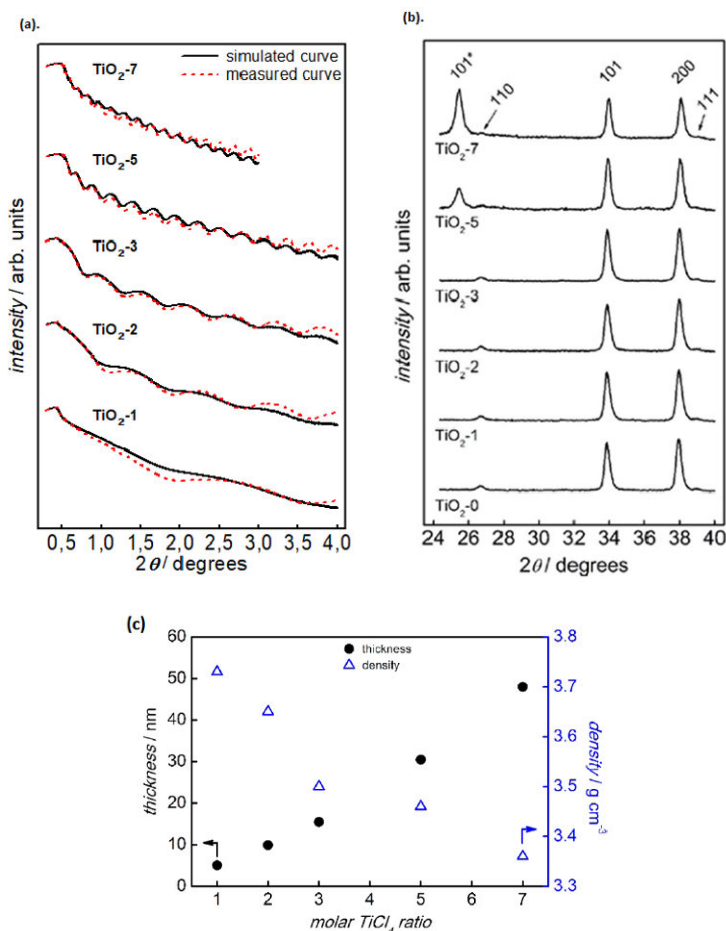


Fig 19. (a) X-ray reflectometry (XRR) interference patterns for TiO_2 films prepared on glass substrates by using different TiCl_4 molar ratios. **(b)** Grazing incidence X-ray diffraction patterns for corresponding TiO_2 films on FTO substrates. **(c)** Thickness and the density of compact TiO_2 films (on glass substrates) as a function of molar concentration of TiCl_4 precursor. (reproduced from Study 1)

5.1.2. Topographical features of FTO substrates with and without compact TiO₂ layers of different thicknesses

AFM characterization was performed to understand the surface structure of the compact TiO₂ layers on FTO substrates. The three-dimensional AFM topographical images and corresponding height profiles of FTO substrates coated with compact TiO₂ films of different thickness are shown in Figure 20. Surface roughness parameters were calculated from the AFM images and are summarized in Table 3. The film thickness, density and crystallite size calculated using the XRR and GI-XRD measurements are also listed in the same table.

Table 3. Thickness, density, crystallite size and surface roughness parameters of compact TiO₂ layers coated on top of the FTO substrate as a function of TiCl₄ molar concentration.

Sample	Thickness [nm]	Density [g cm ⁻³]	Crystallite size* [nm]	S _q [nm]	S _{dr} [%]	V _v [μm ³]
TiO ₂ -0	-	-	-	34	39	3.5
TiO ₂ -1	5	3.73	-	36	45	3.6
TiO ₂ -2	10	3.68	-	32	28	3.5
TiO ₂ -3	16	3.50	-	30	27	3.6
TiO ₂ -5	31	3.47	20	30	20	3.0
TiO ₂ -7	48	3.36	22	19	8	0.7

*The crystallite size was measured using the Scherrer's equation from (101) reflection in the GI-XRD diffractogram.

The bare FTO substrate (i.e. TiO₂-0 sample) exhibits a high surface roughness with a root-mean-square roughness (S_q, i.e., standard deviation of height) of 34 nm and a surface area ratio (S_{dr}) of 39%. The void volume (V_v) is 3.5 μm³, which is relatively large. The TiO₂-1 sample (i.e. FTO substrate with a 5 nm TiO₂ film on top) shows a slight increase in all the roughness parameters. S_q increases by 7% and S_{dr} by 14% and V_v by 2%. With further increase in the thickness of the compact TiO₂ layer, the roughness parameters gradually decrease down to S_q = 19 nm and S_{dr} = 8% for the TiO₂-7 sample. It is interesting to note that the void volume remains nearly constant (i.e., between 3.5 to 3.6 μm³) up to the TiO₂-3 sample. Then it drastically decreases to 3.0 μm³ for TiO₂-5 and 0.7 μm³ for TiO₂-7. The AFM measurements clearly show that the TiO₂ films cover the rough FTO substrates very well. Slight reduction in roughness parameters for samples prepared from lower TiCl₄ concentrations shows that TiO₂ is very evenly distributed on the rough substrate. However, at higher concentrations (i.e. for samples corresponding to TiCl₄-5 and TiCl₄-7), the surface smoothens out by filling the voids with TiO₂. In other words, this means that the thickness of the compact TiO₂ films varies locally depending on the texture of the rough FTO substrates. The films are thicker in the valleys, while they are thinner on top of the peaks of the FTO crystals. All of these observations are well supported by AFM height profiles shown in Figure 20 and the corresponding surface roughness parameters listed in Table 3. Furthermore, it is interesting to note that the crystallization of TiO₂ seems to start just after the void volume starts to decrease significantly (i.e. for sample TiO₂-5 and beyond). It can thus be stated that some critical volume within the voids needs to be filled with TiO₂ before the crystallization can start.

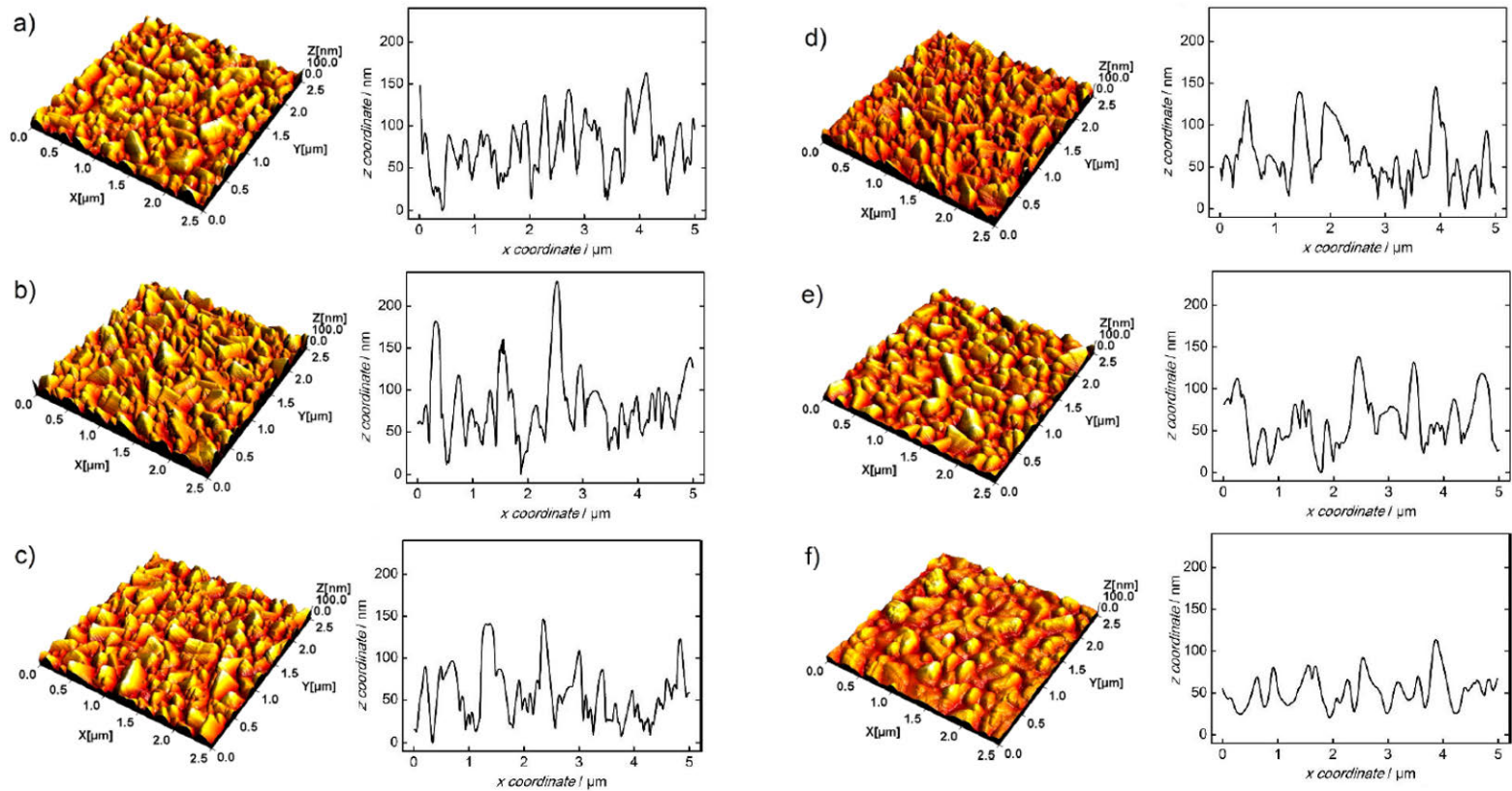


Fig 20. 3-D AFM topographical images and corresponding height profile of FTO substrates with increasing thickness of the TiO_2 film: (a) TiO_2 -0, (b) TiO_2 -1, (c) TiO_2 -2, (d) TiO_2 -3, (e) TiO_2 -5, and (f) TiO_2 -7. (reproduced from Study 1)

5.1.3. Detection of pinholes through compact TiO₂ films on top of FTO substrates

The detection of pinholes through compact TiO₂ films on top of FTO substrates is schematically explained in Figure 21. The compact TiO₂ film with optimal thickness completely covers the underlying FTO substrate, such that no FTO crystals protrude through the titania film. This was investigated using XPS which is known to determine the chemical composition of surfaces with high level of precision. The compact TiO₂ film of optimal thickness on top of FTO substrate is expected to give no Sn signal which originates from FTO crystals.

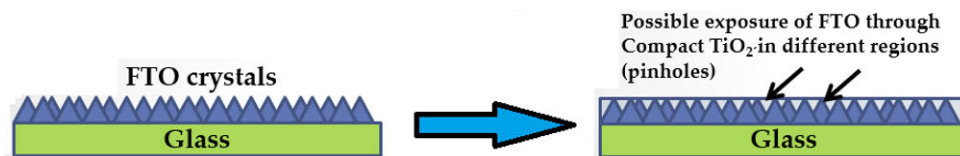


Fig 21. When the FTO substrate is covered with a compact TiO₂ film, FTO crystals might be exposed through the TiO₂ layer. The exposed FTO can be observed through XPS measurements.

Figure 22 (a) and (b) show the XPS spectra which are quantitatively summarized in Figure 22 (c) and listed in Table 4. Figure 22(a) shows the characteristic 3d^{5/2} and 3d^{3/2} peaks of Sn observed at 486 and 495 eV binding energies, respectively. It shows that the intensities of the Sn signals decrease significantly from 17.5 atom % for TiO₂-0 sample (i.e., the bare FTO substrate) down to 1.24 atom % for the TiO₂-3 sample. No Sn signals could be detected from the surface of the TiO₂-5 sample. This can be explained by a continuous reduction of exposed FTO crystals with the increase in compact TiO₂ film thickness until completely covered in the TiO₂-5 sample.

On the other hand, Figure 22(b) shows 2p^{1/2} and 2p^{3/2} peaks of Ti at 464 and 486 eV respectively. The figure shows that the atomic percentage of Ti increases gradually from zero for the TiO₂-0 sample to 18.6 atom-% for the TiO₂-5 sample, reflecting the increase in TiO₂ film thickness.

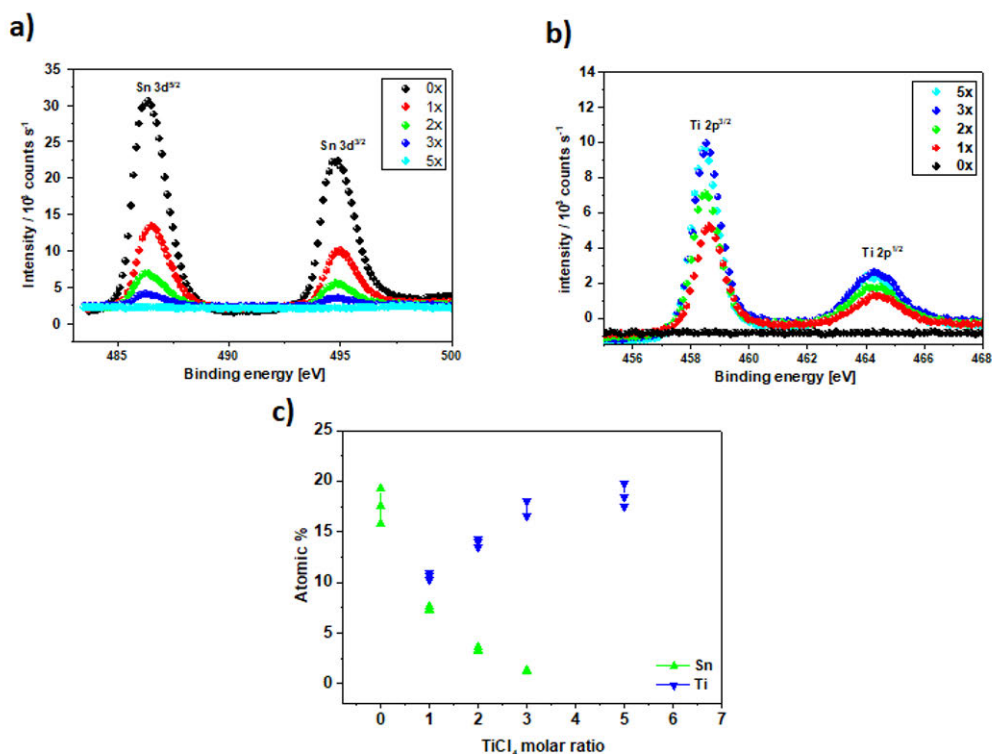


Fig 22. High resolution XPS spectra representing characteristic binding energy peaks for (a) Sn and (b) Ti for bare FTO (TiO_2 -0) and the FTO substrates coated with TiO_2 film prepared from different molar ratios of TiCl_4 precursor. (reproduced from Study 1)

Table 4. Atomic concentration of the elements detected using XPS spectra. The values shown here are the average values of the atomic percentage measured at three different points of the samples.

Sample	Concentration			
	Sn	Ti	O	C
	[at-%]			
TiO_2 -0	17.5 ± 1.8	0.0 ± 0.0	48.3 ± 1.6	34.2 ± 3.3
TiO_2 -1	7.4 ± 0.2	10.6 ± 0.4	50.4 ± 1.5	31.5 ± 2.0
TiO_2 -2	3.4 ± 0.2	13.9 ± 0.4	50.4 ± 0.6	32.3 ± 1.1
TiO_2 -3	1.2 ± 0.1	17.6 ± 0.9	52.4 ± 3.0	28.7 ± 3.8
TiO_2 -5	0.0 ± 0.0	18.6 ± 1.2	51.2 ± 2.1	30.1 ± 3.2

Since the probing depth of XPS is 5 to 10 nm, it is still possible that a complete surface coverage of TiO_2 is already achieved for the TiO_2 -3 sample and the small intensities of Sn signals might be coming through the thin TiO_2 layer.

5.1.4. Device performance versus compact TiO₂ film thickness

Figure 23 shows light J-V curves of representative devices based on compact TiO₂ layers prepared from different TiCl₄ precursor concentrations. The photovoltaic parameters and the standard deviations for all the devices are summarized in Table 5. The measurements were performed between -1.0 to 1.5 V in both forward and reverse sweep with a scan rate of 10 mV/s. The hysteresis between the forward and reverse scan was very low, hence only the reverse scan is shown in Figure 23. The low hysteresis could be attributed to restricted ion movement due to the mesoscopic TiO₂ scaffold layer. Furthermore, most of the photocurrents are generated within the perovskite embedded in the TiO₂ nanostructure, which allows for an efficient electron extraction with minor charge build-up at the interface. This could also be a potential reason behind the low hysteresis. Therefore, my discussion will be based on the results from the reverse sweep, which are not far different from the photovoltaic parameters derived from the forward sweep.

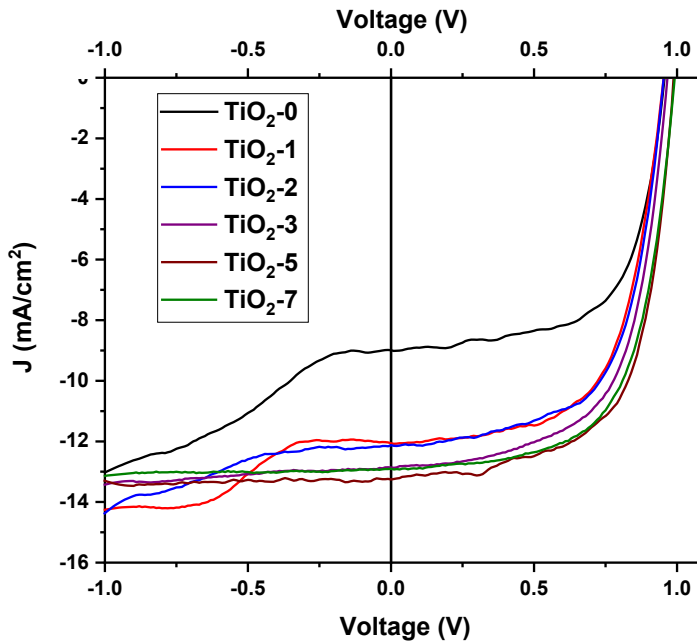


Fig 23. The light J-V curves for the reverse sweep from 1.5 to -1.0 V for devices without compact TiO₂ (TiO₂-0) and for devices with an increasing compact TiO₂ film thickness. (reproduced from Study 1)

Table 5. Photovoltaic parameters for devices without compact TiO₂ (TiO₂-0) and for devices based on compact TiO₂ layer of different thickness, determined from light J-V curves for the forward and reverse sweep between -1.0 and 1.5 V.

Sample	N ^a		J _{sc} ^b [mA cm ⁻²]	V _{oc} ^c [V]	FF ^d	PCE ^e [%]
TiO ₂ -0	10	fwd:	9.4±0.9	0.91±0.03	0.56±0.05	4.7±0.6
		rev:	9.5±0.9	0.93±0.03	0.62±0.03	5.5±0.8
TiO ₂ -1	6	fwd:	12.7±1.3	0.95±0.01	0.57±0.06	7.0±1.3
		rev:	12.5±1.2	0.95±0.02	0.62±0.04	7.4±1.1
TiO ₂ -2	12	fwd:	12.4±1.0	0.96±0.02	0.60±0.02	7.1±0.7
		rev:	12.4±0.8	0.96±0.02	0.63±0.01	7.5±0.6
TiO ₂ -3	9	fwd:	13.4±0.4	0.95±0.03	0.62±0.02	7.9±0.5
		rev:	13.3±0.4	0.94±0.03	0.61±0.03	7.8±0.6
TiO ₂ -5	12	fwd:	13.2±0.7	0.98±0.02	0.63±0.01	8.2±0.5
		rev:	13.2±0.7	0.97±0.02	0.67±0.02	8.6±0.4
TiO ₂ -7	4	fwd:	13.5±0.5	0.99±0.01	0.61±0.04	8.2±0.6
		rev:	13.2±0.4	0.98±0.03	0.62±0.05	8.0±0.7

^a Number of measured devices. ^b Short-circuit current density. ^c Open-circuit voltage. ^d Fill factor. ^e Power conversion efficiency

The J_{sc} increases from 9.5 mA/cm² for devices without compact TiO₂ layer (i.e., for the TiO₂-0 sample) up to 13.2 mA/cm² for the TiO₂-7 sample. Similarly, the V_{oc} also increases from 0.93 to 0.98 V with increase in the thickness of compact TiO₂ layer while the fill factor remains nearly constant (i.e., about 0.62). The power conversion efficiencies (PCEs) increase from 5.5% for TiO₂-0 to 8.6% for the TiO₂-5 compact layer. The PCE is primarily enhanced due to increase in J_{sc} while other photovoltaic parameters either do not change so significantly or they remain nearly constant with increase in compact layer thickness. The values for J_{sc} and V_{oc} significantly increase until the TiO₂-5 sample, while their values remain similar for devices made from TiO₂-7 compact layers. Therefore, it can be concluded that a complete surface coverage of TiO₂ on top of the FTO substrate is already achieved with the TiO₂-5 compact layer. A further increase in the c-TiO₂ thickness is not beneficial for additionally improving the photovoltaic performance of the device. This is consistent with the GI-XRD and XPS results.

The V_{oc} is still quite high even for devices without compact TiO₂, which suggests that the surface recombination at FTO contact is low even when there is no compact TiO₂ layer.²²¹ For the TiO₂-0 sample, the FTO is exposed at the bottom of mesostructured TiO₂ layer due to the absence of compact TiO₂ layer. Thus, the low surface recombination without compact TiO₂ layer could be attributed to the presence of a substantial amount of unreacted PbI₂ (which has hole blocking properties) between the perovskite and FTO.^{222, 223} The effect of unreacted PbI₂ will be further discussed in study 2. In this case, the V_{oc} cannot be used to draw conclusions about the presence of pinholes in the thinner compact TiO₂ layers. However, the J-V curves of samples TiO₂-0, TiO₂-1, and TiO₂-2 show strong s-shaped behavior in the negative voltage regime (between -0.70 and -0.25 V), which significantly contribute

to the lower J_{SC} values for these samples. On the basis of some numerical calculations performed by Sandberg et al.,²²⁴ the distinct s-shaped feature in the J-V curves for the devices with or without thin compact TiO_2 layers can be attributed to the presence of negatively charged immobile ions at the interface between the perovskite and exposed FTO (i.e., the pinholes). These negatively charged immobile ions screen the built-in potential of the device at low positive voltages (i.e. between 0 and 1 V). This suppresses the extraction of photo-generated electrons, which results in lower J_{SC} values for samples TiO_2 -0 to TiO_2 -3. On the other hand, these electrons are fully extracted in the negative voltage regime, which is evident from the fact that the current is almost the same for all the devices at -1 Volts (about -13 mA/cm²). There is a strong correlation between the magnitudes of the s-shaped features in the J-V curves (shown in Figure 23) and the exposed FTO (confirmed by the XPS measurements in Figure 21). Thus, it appears that the trapped ions at the poorly defined interface between the perovskite and FTO is the main cause for this phenomenon. This effect diminishes upon incorporating a thicker compact TiO_2 layer, i.e., for the TiO_2 -5 and TiO_2 -7 samples.

5.1.5. Conclusions from Study 1:

This study highlights the importance of having a uniform and thick enough compact TiO_2 layer (even if the solar cell contains mesoscopic layer). It is shown that too thin compact TiO_2 layers (< 30 nm) display pinholes as evidenced by XPS and AFM measurements. Although the devices made from these layer still work (with high V_{OC}), they still suffer from s-shaped features at higher negative voltages due to the presence of negatively charged immobile ions within the pinholes (i.e., where the underlying FTO substrate is exposed). This indicates that large amount of photogenerated electrons in the perovskite cannot be extracted in the positive voltage regime thus these devices exhibit lower J_{SC} values. Therefore, the devices comprising of thinner compact TiO_2 layers (<30 nm) show relatively low PCEs. However, when the compact TiO_2 layer is thick enough (i.e., ≥ 30 nm), the devices perform optimally because then, the pinholes are expected to be completely eliminated from the compact TiO_2 layer.

5.2. Effect of surface activation of mesoscopic TiO_2 scaffold (Study 2)

In conventional mesoscopic PSCs, the mesoscopic layer (comprising of TiO_2 nanoparticles) is coated on top of the compact TiO_2 layer. This mesostructured layer acts as a scaffold to support crystallization of the perovskite, which is partially embedded within the nanostructure, while the perovskite capping layer on top isolates the TiO_2 from the hole-selective layer (HSL).

When the perovskite is prepared via the 2-step sequential deposition method, the PbI_2 crystallizes within the nanostructure in the form of well-dispersed nanocrystals. These PbI_2 nanocrystals within the mesostructured TiO_2 are more accessible for the MAI solution than when the PbI_2 is crystallized in the form of a dense film on top of a planar compact TiO_2 layer. Therefore, better conversion efficiency of PbI_2 to $MAPbI_3$ is expected when a mesostructured TiO_2 scaffold is used.²²⁵ However, the processing conditions and surface properties of mesostructured TiO_2 layer can also influence the crystallization of PbI_2 within the nanostructure and its subsequent conversion to $MAPbI_3$, which ultimately affects the performance of PSCs. For instance, if the mesostructured substrate is stored for a long time prior to the deposition of PbI_2 in ambient atmosphere, the wettability of its internal and exterior surfaces can be significantly be reduced due to the adsorption of volatile organic compounds. If an efficient surface activation protocol is applied to remove such organic constituents, the surface wettability can even become higher than required. Then, the subsequently deposited PbI_2 will most likely crystallize densely and hinder its conversion to $MAPbI_3$ upon immersion in MAI solution. Thus, an incomplete conversion

to perovskite means a lower amount of photoactive layer to generate photocurrents upon illumination.

In this study, the mesoporous TiO_2 scaffold was exposed to two different surface activation methods; UV light and oxygen plasma treatment. Both of the two different surface activation protocols were found to differently influence the crystallization of PbI_2 within the nanostructure and its conversion to MAPbI_3 . Therefore, the devices prepared using two different surface activation methods were found to perform differently from one another.

5.2.1. Characterization of PbI_2 -coated mesoporous TiO_2 and corresponding perovskite after conversion

Mesoscopic TiO_2 layers coated on top of compact $\text{TiO}_2/\text{FTO}/\text{glass}$ substrates were activated by UV-light (for 17 min under ambient conditions) or oxygen plasma treatment (for 5 min) prior to the deposition of PbI_2 by spin coating (using the protocol mentioned in section 4.3.5.). Non-surface treated substrates were also coated with PbI_2 as a reference. The PbI_2 -coated substrates were subsequently converted to MAPbI_3 by dipping in MAI solution (as discussed in section 4.3.5).

The first goal was to determine how different surface treatments of the mesoporous TiO_2 layer influence the formation of PbI_2 and its subsequent conversion to perovskite. For this, GI-XRD was performed on the substrates using three different grazing incidence angles. The reflections at 12.6° and 14.1° are associated with the (001) reflection of PbI_2 and (110) reflection of MAPbI_3 phases, respectively. Incomplete reaction of PbI_2 to perovskite is manifested by the presence of the (001) PbI_2 reflection with significantly high intensities for all the samples in Figure 24. In other words, all samples contain both PbI_2 and MAPbI_3 phases. The XRD diffractograms can be used to estimate the PbI_2 to MAPbI_3 conversion efficiency as a function of different surface treatment methods and different grazing incidence angles. A higher area percentage of the perovskite reflection indicates a better conversion. The area percentages of perovskite reflections as a function of different surface activation methods and grazing incidence angles are shown in Table 5. At a grazing incidence angle of 1° , the area percentage of perovskite reflection peak is 68.8% for the non-treated sample. The UV-treated and plasma-treated samples give perovskite area percentages of 65.7% and 38.1%, respectively. This means that the conversion efficiency for UV treated sample is slightly lower than the non-treated sample, while it is highly suppressed for the plasma treated sample. The original amount of PbI_2 is expected to be same for all the samples where better conversion would generate more perovskite in absolute amount. Performing XRD at higher grazing incidence angles gives information about the composition deeper inside the layer. Thus, deeper into the composite film, the conversion of PbI_2 to perovskite appears to be less efficient. A possible reason for this is that the conversion is more efficient at the top of the PbI_2 layer and once the perovskite is formed, it obstructs the diffusion of MA^+ cations into underlying PbI_2 . This is the main cause behind incomplete conversion at moderate MAI concentrations (such as 10 mg/mL used in this study).²²⁶

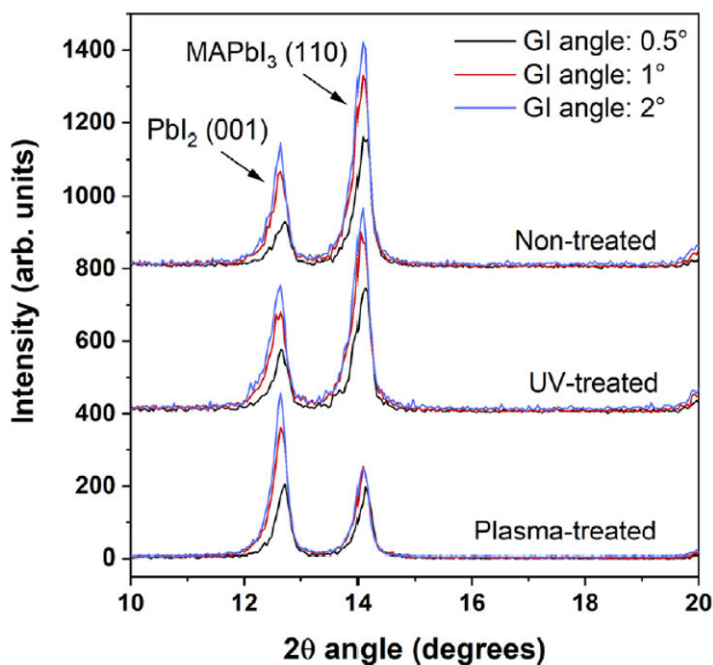


Fig 24. XRD patterns for perovskite films prepared on top of mesoscopic TiO_2 films activated by different surface treatments at different grazing incidence (GI) angles. (reproduced from Study 2)

Figure 25 shows UV-vis absorption spectra for PbI_2 layers coated on differently surface-treated mesoporous TiO_2 films and for the corresponding perovskite formed after reaction with MAI. According to the UV-vis absorption spectra, different surface activation methods do not alter the amount of PbI_2 . Differences in the UV-vis spectra appear only after conversion of PbI_2 to the perovskite. The UV-treated and non-treated samples show quite similar absorption between 500 to 750 nm wavelength range. At 700 nm, 38.1% and 38.6% transmittance were observed for UV-treated and non-treated samples, respectively. On the contrary, the plasma-treated sample shows the highest transmittance of 46.1% at 700 nm. Thus, it can be concluded that the highest amount of perovskite is obtained for the UV-treated and non-treated samples, while it is the lowest for the plasma-treated sample, which follows the same trend observed in the XRD diffractograms.

Table 5: Summary of the grazing incidence X-ray diffraction results: (a) the percentage of perovskite phase as a function of different surface treatment methods and grazing incidence angles, (b) UV-vis transmittance values at 700 nm.

Sample	Perovskite peak area at different GI angles			Transmittance at 700 nm
	0.5°	1°	2°	
Non-treated	77.2%	68.8%	67.9%	38.6%
UV-treated	67.5%	65.7%	61.5%	38.1%
Plasma-treated	48.3%	38.1%	34.3%	46.1%

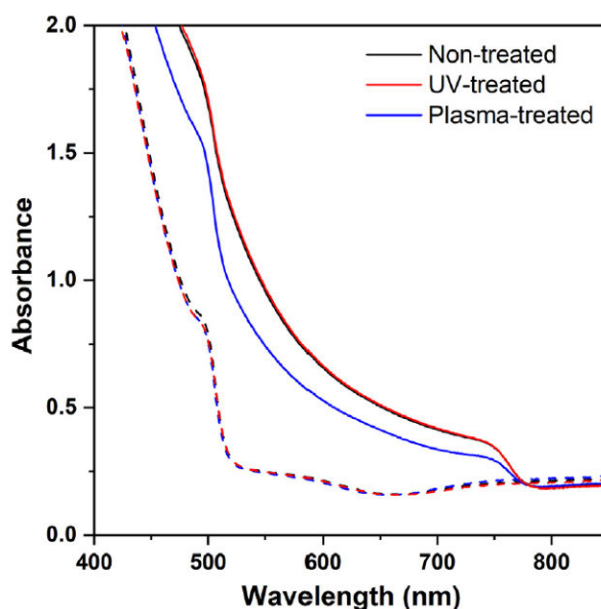


Fig 25. UV-vis absorption spectra for PbI_2 films (dashed lines) deposited on mesostructured TiO_2 films after various surface treatments and the corresponding perovskite formed after reaction with MAI. (reproduced from Study 2)

PbI_2 coated on differently surface-treated mesoporous TiO_2 layers and the corresponding perovskite capping layers were subjected to top-view SEM analysis (shown in Figure 26). Starting from PbI_2 films shown in Figure 26(a-c), it can be seen that the mesoporous TiO_2 films are covered with moderately open capping layers of perovskite. Unfortunately, it is not possible to investigate the PbI_2 structure inside the pores. A more open PbI_2 capping layer would be beneficial for MA^+ cations to reach the PbI_2 inside the mesostructure to ensure efficient conversion to perovskite. This also depends on the denseness of the PbI_2 inside the porous structure. After converting these films to perovskite by dipping them in MAI solution, the resulting perovskite capping layers still contain some pinholes. It is important to realize that these pinholes may go through all the way to the underlying mesoscopic TiO_2 , which can

possibly result in the formation of parallel shunts due to the establishment of Spiro-OMETAD/TiO₂ interface. However, there is no evidence to prove this at the moment. Interestingly, the number of pinholes seem to decrease when going from non-treated to UV-treated and then to plasma-treated samples. This can potentially influence the device performance (especially the open circuit voltage, V_{oc}), which will be discussed in section 5.2.2.

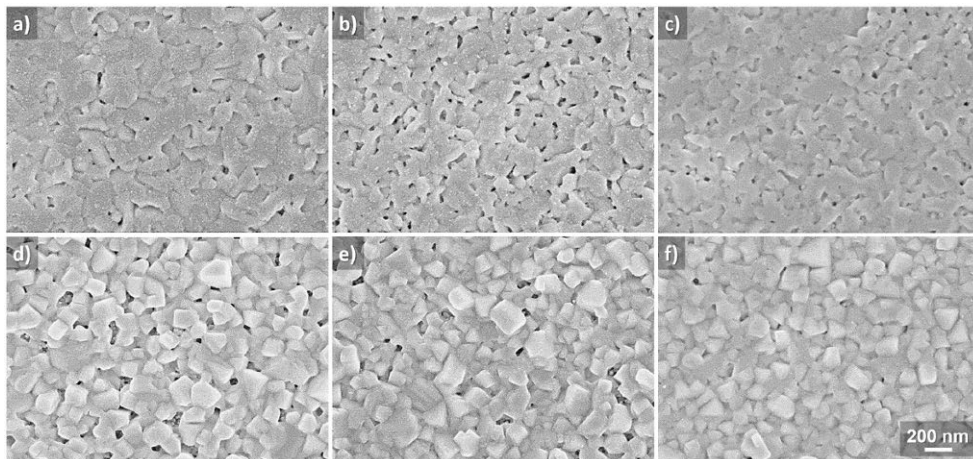


Fig 26. Top-view SEM images of PbI_2 coated on mesoporous TiO_2 films activated by different methods: (a). Non-treated, (b). UV-treated, (c). Plasma-treated. The corresponding perovskite capping layers after conversion: (d). Non-treated, (e). UV-treated, and (f). Plasma-treated. (reproduced from Study 2)

5.2.2. Device performance

Figure 27 shows J-V curves under illumination for representative devices prepared on top of differently surface-treated mesoscopic TiO_2 layers. The mean and standard deviation for all the photovoltaic parameters (4 to 6 devices per surface treatment) are summarized in Table 6. The devices prepared on non-treated mesoporous TiO_2 substrates show good photovoltaic performance with a J_{sc} of about 13.7 mA/cm², V_{oc} of 0.91 V, and FF of 0.62 in the forward sweep. This results in a PCE of about 7.6%, which is lower than for devices of a similar type reported earlier.^{69, 197} The reason behind this could be the slightly thinner PbI_2 /mp- TiO_2 composite layer, relatively large area of device, or relatively lower conversion of PbI_2 to the perovskite. It is also good to know that all the devices show low hysteresis (i.e., hysteresis index below 1%), which is consistent with the device performance shown in the first study for this thesis.

Surprisingly, the overall PCE is enhanced to 9.3% for the UV-treated sample, which is an improvement by more than 20% in comparison to the samples without any surface activation of the mesoscopic layer. On the other hand, the plasma-treated samples show considerably lower efficiencies (i.e., average PCE of about 5.6%). Thus, the device efficiency is less than 75% of the efficiency of non-treated samples. These results highlight the importance of surface activation as the device efficiencies can vary between 5.6% and 9.3% by just applying different surface activation protocols.

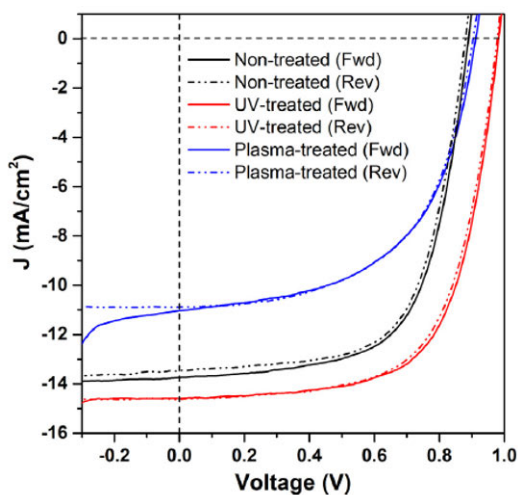


Fig 27. J-V curves measured under illumination for representative devices prepared after applying different surface activation protocols on the mesoporous TiO₂ scaffold. (reproduced from Study 2)

Table 6. Mean photovoltaic parameters and the corresponding standard deviations (for 4 to 6 devices) for the different surface activation methods.

	J_{sc} (mA/cm ²)	V_{oc} (V)	FF	PCE (%)
<i>Forward Sweep</i>				
Non-treated	13.7 ± 0.3	0.91 ± 0.02	0.62 ± 0.02	7.6 ± 0.3
UV-treated	14.4 ± 0.3	0.96 ± 0.02	0.66 ± 0.01	9.3 ± 0.3
Plasma-treated	10.8 ± 1.0	0.91 ± 0.02	0.57 ± 0.02	5.6 ± 0.5
<i>Reverse Sweep</i>				
Non-treated	13.3 ± 0.4	0.90 ± 0.03	0.62 ± 0.02	7.4 ± 0.3
UV-treated	14.4 ± 0.3	0.96 ± 0.02	0.65 ± 0.02	9.0 ± 0.4
Plasma-treated	10.7 ± 0.9	0.87 ± 0.08	0.55 ± 0.08	5.2 ± 1.2

The trends in the J_{sc} values correlate well with the relative amounts of the perovskite observed from the XRD and UV-vis measurements (as summarized in Table 5). Since the plasma-treated sample contains the lowest fraction of perovskite, it also has the lowest light absorption ability to generate photocurrent. Thus, a more complete conversion of the PbI₂ to the perovskite should lead to higher J_{sc} and thus higher PCEs. The slight enhancement in the J_{sc} for the UV-treated sample could be due to less electron-hole recombination as a consequence of a lower number of pinholes in the perovskite capping layer. Furthermore, the variations in area fractions of the pinholes in the perovskite capping layers (shown in Figure 28) can also explain the differences in the V_{oc} and the FF between the various surface activation protocols.²²⁷ Pinholes in the perovskite capping layer can form shunt pathways between the spiro-OMeTAD HSL and the TiO₂ ESL, which can ultimately result in a reduced V_{oc} and FF. However, on the basis of Table 6, the V_{oc} values for the devices based on plasma-treated mesoscopic layer and the non-treated ones are nearly similar. This could be partially due to the lower number of pinholes in the

perovskite capping layers for the plasma-treated samples in comparison to the non-treated ones. The UV-treated samples show a lower number of pinholes in the perovskite capping layer in comparison to the non-treated sample. But, it is much larger than the plasma-treated sample. Higher V_{OC} for UV-treated samples in comparison to non-treated ones could be due to the better capping layer (with less density of pinholes). On the other hand, its higher V_{OC} in comparison to that for plasma-treated sample could be related to relatively efficient conversion of PbI_2 to the perovskite.

5.2.3. Proposed mechanism for the PbI_2 formation and its conversion to perovskite

The device performance is found to be significantly influenced by different ways to activate the surface of mesoporous TiO_2 layers. Thus, the processing conditions during device manufacturing must be carefully controlled to avoid variations in the performance of solar cells.

Different surface activation methods for the mesoscopic TiO_2 layer prior to the deposition of PbI_2 can alter the wettability of the nanostructured substrate. The differences in substrate wettability can thus influence the final structure of the perovskite. In this section, a mechanism is proposed that explains the main differences in the device performance when the mesoporous TiO_2 layer is activated by different methods prior to the PbI_2 deposition. This mechanism is schematically explained in Figure 28.

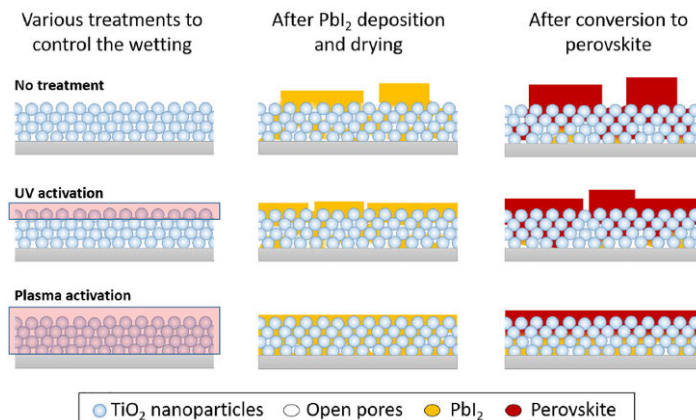


Fig 28. Proposed PbI_2 formation and its conversion to perovskite as a function of different surface activation protocols. (reproduced from Study 2)

Since TiO_2 is photoactive in the UV region, the UV treatment generally activates the top-most part of the mesoporous TiO_2 film. Wahl et al suggested that the penetration depth of UV light (with a wavelength of 300 nm) is not more than 30 nm for similar mesoscopic TiO_2 structure.²²⁸ However, the charges produced as a result of illumination with UV light, might diffuse throughout the TiO_2 layer and form reactive surface groups also deeper inside the mesostructured film. Thus, it would be more realistic to say that the activation level by UV light is gradually decreasing with increasing depth of the mesostructured TiO_2 film. On the other hand, the plasma treatment activates the entire mesostructured TiO_2 layer (which includes both interior and exterior surfaces).

Water contact angle measurements were performed on the surface of mesoporous TiO_2 layers after applying different surface treatments. These measurements are shown in Figure 29. This was done in order to investigate the trends in the wettability of the surface of mesoscopic layer as a function of different surface activation protocols. The non-treated sample is wetted by the water droplet quite

well with a contact angle of about 9°. It would be worth to mention here that the surface roughness strongly influences the wettability and therefore, the porous surface could be more hydrophilic than a planar surface of similar chemistry.²²⁹ Upon placing the water droplet on the UV- and plasma-activated mesoporous TiO₂ layers, the contact angle reached zero almost immediately. Comparable results have also been reported earlier for UV- and plasma-activated TiO₂ thin films.^{229, 230}

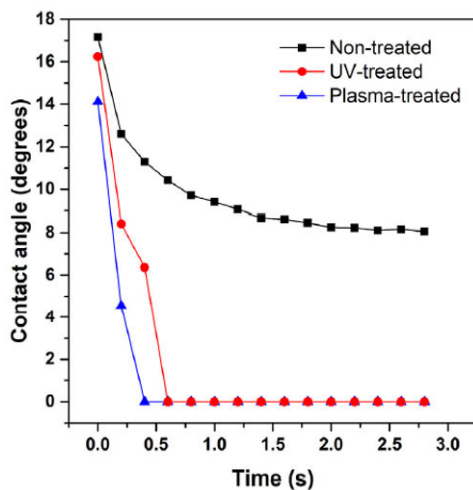


Fig 29. Time-dependent water contact angle measurements of differently surface-treated mesoporous TiO₂ films. (reproduced from Study 2)

In order to understand the differences in the conversion efficiencies of PbI₂ to the perovskite and the device performance as a function of surface activation methods, it is important to understand the effective depth of activation when using different types of surface treatments. From the water contact angle measurements, it is difficult to deduce the extent of activation within the interior surfaces of mesostructured TiO₂ layers. Thus, an additional experiment was performed to determine the effect of UV and plasma activation on the degradation of N719 dye embedded within the mesostructured TiO₂ layers. UV-vis measurements were performed to determine the amount of dye left within the nanostructured TiO₂ thin films after applying two different surface activation protocols on the surface. The measurements are shown in Figure 30. The UV-Vis spectra for the dye loaded mesostructured substrates remained almost unchanged even after UV irradiation while the absorption was significantly reduced after plasma treatment. This indicates that UV irradiation for 20 min was only able to remove small fraction of dye molecules, while the plasma treatment for only 5 min degraded almost all the N719 dye loaded within the nanostructured TiO₂ film.

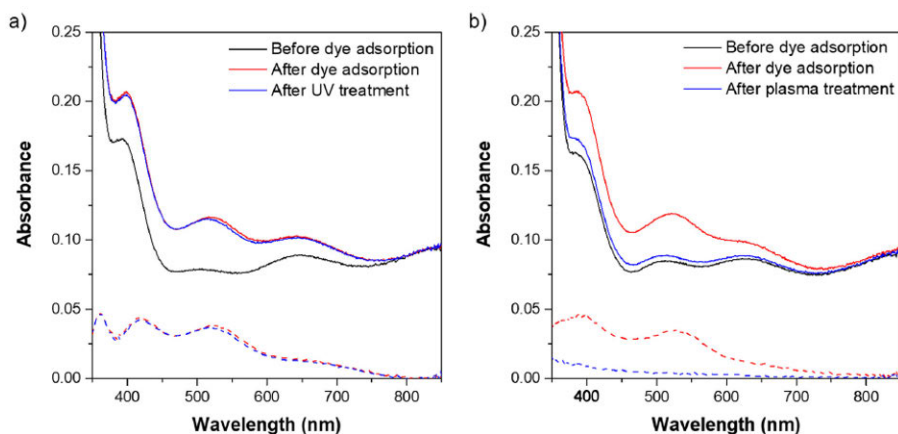


Fig 30. UV-vis spectra for mesoscopic TiO_2 films before and after adsorption of N719 dye as well as after surface treatment with (a) UV light, and (b) plasma. The dashed lines represent the absorption spectra after subtracting the spectra of the non-dyed substrates. (reproduced from Study 2)

By combining the results from the water contact angle and the dye-degradation tests, one can conclude that the plasma activation is highly effective throughout the entire mesostructured TiO_2 layers, while the UV treatment is only able to activate the upper most surface. The enhanced wettability of the interior surfaces of mesostructured TiO_2 results in good infiltration of PbI_2 within the pores (see Figure 28). Regrettably, the dense packing of PbI_2 within the porous structure makes its conversion to the perovskite more difficult due to the inability of MAI solution to reach down to the PbI_2 in the bottom parts of the mesostructured films. Secondly, the pore channels and their entrances can be blocked as a result of the large volume expansion associated with the conversion of PbI_2 to the perovskite. This would further hinder the transportation of MAI solution to reach the PbI_2 deeper inside the TiO_2 structure.

On the other hand, due to the lower activation efficiency inside the TiO_2 pores, the packing of the PbI_2 crystals within the non-activated and the UV-activated samples is expected to be less dense. This would result in open pathways for MAI reactant to reach the bottom parts of the mesostructured films, which supports a more complete conversion of PbI_2 to perovskite. This is evident from the XRD, UV-vis and J-V results previously discussed.

Some similar improvement in the device performance have been previously shown by changing the thickness and porosity of mesoscopic layer in order to alter the amount of PbI_2 loaded within the nanostructured TiO_2 .^{69, 142, 231} However, this does not explain the better performance of the devices containing UV-treated mesoscopic TiO_2 layers. The improved wettability of the top-most surface of the mesoscopic scaffold could result in an improved perovskite capping layer, which could give a pinhole-free perovskite capping layer or a capping layer with reduced number of pinholes. The reduction in the number of pinholes in the capping layer results in a higher V_{OC} (i.e., lower shunt resistance and surface recombination).²²¹ Since the UV treatment only activates the top-most part of the mesoscopic TiO_2 layer, PbI_2 crystallizes sparsely within the nanostructure (which supports a good conversion to perovskite within the nanostructure just like when the scaffold is non-treated) while a good capping layer of the perovskite is formed on top of the mesostructure containing a low number of pinholes.

5.2.4. Conclusions from Study 2

In this study, two different surface treatment methods were applied on the surfaces of mesoscopic TiO_2 layers, which were to be later incorporated into PSCs produced by the two-step sequential deposition route. This study revealed that the type of surface treatment method for mesoscopic scaffolds significantly influences the device performance. Although both the UV and plasma treatment enhance the wettability of the surface of the mesoscopic TiO_2 layer, the penetration depth of the two different surface activation methods is quite different (as revealed by the dye degradation test). UV irradiation for about 20 min only activates the top-most surface of the mesoscopic TiO_2 layer, while oxygen plasma treatment for 5 min activates the entire scaffold. Since the plasma treatment enhanced the wettability of the entire scaffold, the PbI_2 tends to crystallize densely within the nanostructure, which hampers its conversion to the perovskite upon immersing the substrate into MAI solution. On the contrary, UV irradiation did not result in a dense packing of PbI_2 crystals since it only activates the upper-most surface of the scaffold. Thus, the conversion of PbI_2 to the perovskite is not hampered as significantly. Since the upper-most surface of the mesoscopic layer is activated, the capping layer of the perovskite is improved and it contains a lower number of pinholes compared to when no additional surface treatment is applied. Upon incorporating differently surface-treated mesoscopic TiO_2 layers into the devices, higher J_{SC} values were observed with the UV-treated scaffolds, while lower values were obtained for devices based on the plasma-treated scaffolds. The large deviations in the device performance as a result of using two different surface activation methods can be explained by the differences in PbI_2 to perovskite conversion efficiencies as well as the number of pinholes in the perovskite capping layers. This study identifies that poorly controlled processing conditions can result in significant variations in device performance. If the processing parameters (such as storage and handling conditions) are not carefully addressed, the device performance may vary from one batch to another. There is a high possibility that the differences in the processing conditions such as the surface activation method and its treatment time, may result in the large variations in the device performance when fabricated by different manufacturers.

5.3. Ordered mesoporous TiO_2 films as a model for compact TiO_2 containing well-defined pinholes for planar heterojunction perovskite solar cells (Study 3)

Morphological defects (such as pinholes) in the electron-selective layer (ESL) are known to deteriorate the performance of PSCs due to increased rate of surface recombination if the perovskite comes in contact with the fluorine-doped tin oxide (FTO) substrate via pinholes. Since the nature of such morphological defects can vary substantially (in the literature as irregular and randomly occurring pinholes), it is difficult to systematically study their possible effects on the performance of PSCs. However, the morphology of the ordered mesoporous TiO_2 films such as those studied by Ortel et al.²⁰² seem to be very well defined, thus such porous films could be used to model pinholes containing compact TiO_2 layers in the planar heterojunction PSCs. The porous network could be modelled as “induced” pinholes provided that it reaches down to the underlying FTO substrate. Therefore, in this study, the block co-polymers templated ordered mesoporous TiO_2 films were synthesized using the colloidal solutions listed in Table 2 in section 4.3.2. The pore size was about 13 to 15 nm. The pores were modeled as nanoscale pinholes which were evenly distributed throughout 50 to 70 nm thick TiO_2 films. The focal point of this study was to investigate the influence of these so called “induced” pinholes in the compact TiO_2 layer on the photovoltaic performance of planar heterojunction PSCs. The effect

of porosity and thickness were studied where the porosity was tuned to simulate a large number of pinholes in a single compact TiO₂ layer.

The influence of induced pinholes on the device performance was found to be very small. Even the devices based on highly porous TiO₂ layers performed very well. This shows that narrow pinholes in the ESL are not detrimental to the device performance provided that the thickness of compact TiO₂ is high enough. However, in case of ultrathin porous layers (around 20 nm), there seems to be a high possibility that the perovskite can reach the conductive FTO substrate via pores and reduce the device performance. This implies that variations in the densities of TiO₂ layers as a result of different deposition methods or rates are of little significance as long as the ESL completely covers the FTO substrate.

The details about the molar composition of the dip coating solutions to synthesize these porous films are shown in Table 2 in section 4.3.2. The names of the porous films with increasing film porosity are as follows: **Ti-0** (without any pores, i.e., compact TiO₂ film), **Ti-6**, **Ti-12** and **Ti-21** where the numbers 0, 6, 12 and 21 corresponds to the molar ratio of the block co-polymers and thus the porosity (i.e., higher the molar ratio of the block co-polymer, higher the porosity). Furthermore, the relative amount of solvent in the dip coating solution was changed for Ti-21 to change the film thickness while maintaining constant film porosity. Thus, the names given to the films were **Ti-21-0.8**, **Ti-21-1** and **Ti-21-2.5**. The numbers 0.8, 1 and 2.5 correspond to the solvent molar ratios. Therefore, the increasing trend in this number corresponds to a decrease in film thickness.

In this study, the ordered mesoporous TiO₂ layers were characterized using grazing incidence x-ray diffraction (GI-XRD), x-ray reflectometry (XRR), field-emission scanning electron microscopy (FE-SEM), and MIS-CELIV measurements. The MIS-CELIV measurements were used as a tool to investigate whether the porous channels reach down to the underlying conductive FTO substrates. If this were not the case, the pores could not be regarded as pinholes.

5.3.1. Structural properties of the ordered mesoporous TiO₂ thin films

Grazing incidence X-ray diffraction (GI-XRD) was performed on TiO₂ thin films coated on top of FTO substrates to investigate the effect of block co-polymer content in the dip coating sols on the final crystal structure. Figure 31 shows the XRD diffractogram for TiO₂ films with increase in block co-polymer content. All films display the anatase crystal structure regardless of the amount of block co-polymer content. However, the intensity of the (101) reflection decreases, while the peaks become broader with an increase in block co-polymer content. Based on Scherrer analysis, the anatase crystallite size decreases with increase in the film porosity (see Table 7). The reflections at 34.0° and 38.1° originate from the underlying FTO substrate.

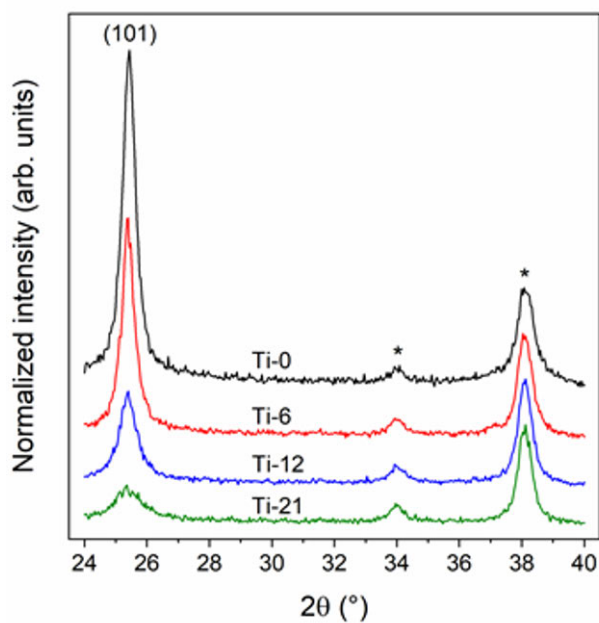


Fig 31. XRD diffractograms of TiO₂ films with different porosity. The reflections coming from the underlying FTO substrates are labelled with asterisks (*). The diffractograms have been normalized with respect to the intensity of the FTO reflection peak at 38.1° as well as offset for clarity. (reproduced from Study 3)

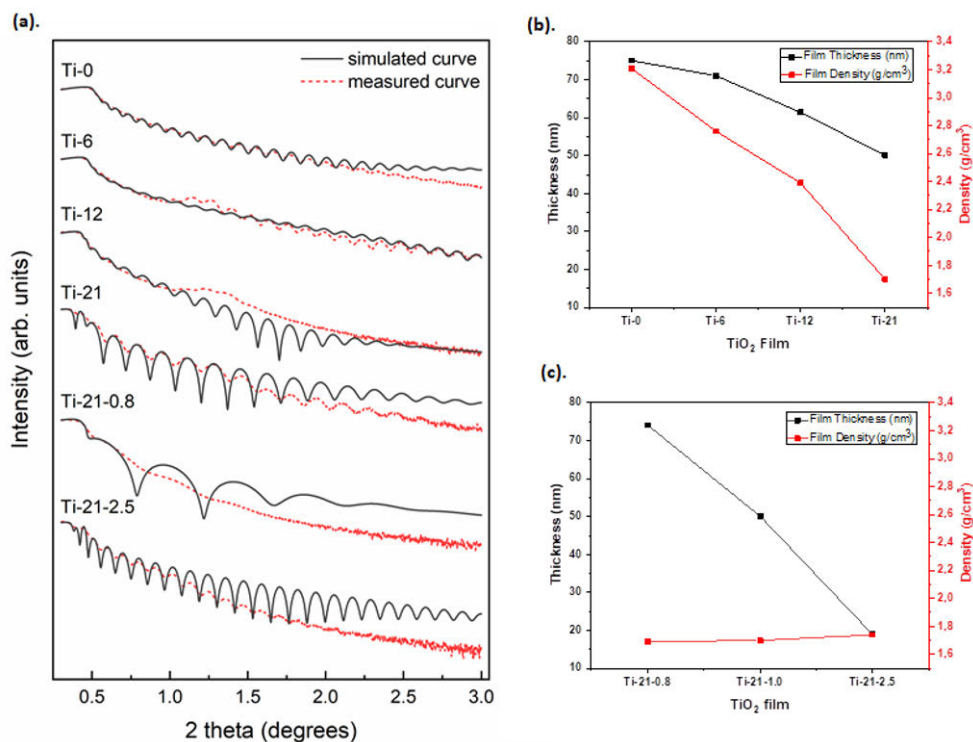


Fig 32. (a). X-ray reflection (XRR) interference patterns of various TiO_2 thin films deposited on glass. Trends in TiO_2 film thickness and density by (b) increasing the block co-polymer content with respect to TiCl_4 precursor, and by (c) increasing the amount of solvent while keeping the same molar ratio between the block co-polymer and the TiCl_4 precursor as shown in Table 2 in section 4.3.2. (reproduced from Study 3)

Table 7. Effect of an increase in the block co-polymer content on the characteristics of the TiO_2 films as evaluated based on the XRD and XRR data.

Sample	Crystallite size (nm)	Thickness (nm)	Density (g/cm^3)	Porosity (%) ¹
Ti-0	20	75	3.21	0
Ti-6	21	71	2.76	14.0
Ti-12	14	61	2.39	25.5
Ti-21	7	50	1.70	47.0

¹The porosity values are calculated for the block co-polymer-templated films by relating their densities to the compact Ti-0 reference sample.

X-ray reflectometry was performed on TiO₂ films dip-coated on top of planar glass substrates to determine the density (i.e., indirectly the porosity) and the film thickness. Figure 32 (a) shows the XRR interference patterns for the TiO₂ films with different porosity. The trends in the film density and thickness as a function of block co-polymer content in the dip coating solution is shown in Figure 32(b) and listed in Table 7. The density of the compact Ti-0 film is lower than values reported in the literature for crystalline anatase TiO₂ (3.79 g/cm³).²¹⁹ However, there is always a possibility that nanocrystalline thin TiO₂ anatase films may possess lower densities. The density of the films decreases with an increase in the block co-polymer content due to the increase in porosity. The film porosity increases up to 47% for the Ti-21 sample. We tried to keep the film thickness constant at around 75 nm in order to correlate changes in the device performance with the film porosity. However, initial experiments by simply increasing the block co-polymer amount resulted in a sharp increase in film thickness as a result of the increase in viscosity of the colloidal solution. The solutions were further diluted with H₂O and ethanol for higher block co-polymers to TiCl₄ ratios (see details in Table 2 in section 4.3.2). In spite of making adjustments by dilution, slight variations in the film thickness was still observed for the samples starting from Ti-0 (75 nm) to Ti-21 (50 nm) sample. Therefore, it is important to separately investigate the effect of film thickness with a constant porosity. In order to produce the thinnest sample, 2.5 times more solvent (ethanol and water) was added in comparison to the Ti-21 sample to produce the dipping sol (sample Ti-21-2.5). On the other hand, the thickest sample (Ti-21-0.8) was produced by using 80% of the solvent used for Ti-21 sample. The XRR measurements shown in Figure 39 (a) and (c) show that the film thickness for Ti-21-2.5 sample is about 20 nm while it is 75 nm for Ti-21-0.8 sample. The density of these films was found to be about 1.7 g/cm³, which is the same for original 50 nm thick Ti-21-1.0 sample.

Figure 33 shows top-view SEM images of films coated on top of FTO substrates. The Ti-0 sample displays a smooth granular surface with 10 to 20 nm grains, which correlates well with the GI-XRD analysis. However, the block co-polymer-templated films (from Ti-6 to Ti-21) show pseudo-ordered mesoporous structures. The SEM images show that the pore wall thickness is reduced from 27 to 15 nm upon increase in the block co-polymer content in the dip coating solutions, while the diameters of the pore openings remain nearly constant between 13 to 15 nm. At the bottom of some of the pores such as those highlighted in the dashed area in Figure 33 c, relatively dark spots can be observed. These spots indicate the presence of a second row of pores deeper in the TiO₂ films. In the EISA process, the final pore structure depends on the arrangement and interconnection between the spherical block co-polymer micelles.²⁰¹ I would expect that the pores are arranged in a body centered cubic (bcc) form with shrinkage perpendicular to the substrate²⁰² forming an ellipsoidal pore geometry. The pores are interconnected via narrow channels through which the combusted block co-polymer escaped during the calcination process. This results in the formation of tortuous pathway down to the underlying substrate. On the basis of the information obtained from GI-XRD, XRR, and SEM, a 2-D cross-sectional diagram of the porous films can be constructed as shown in Figure 34.

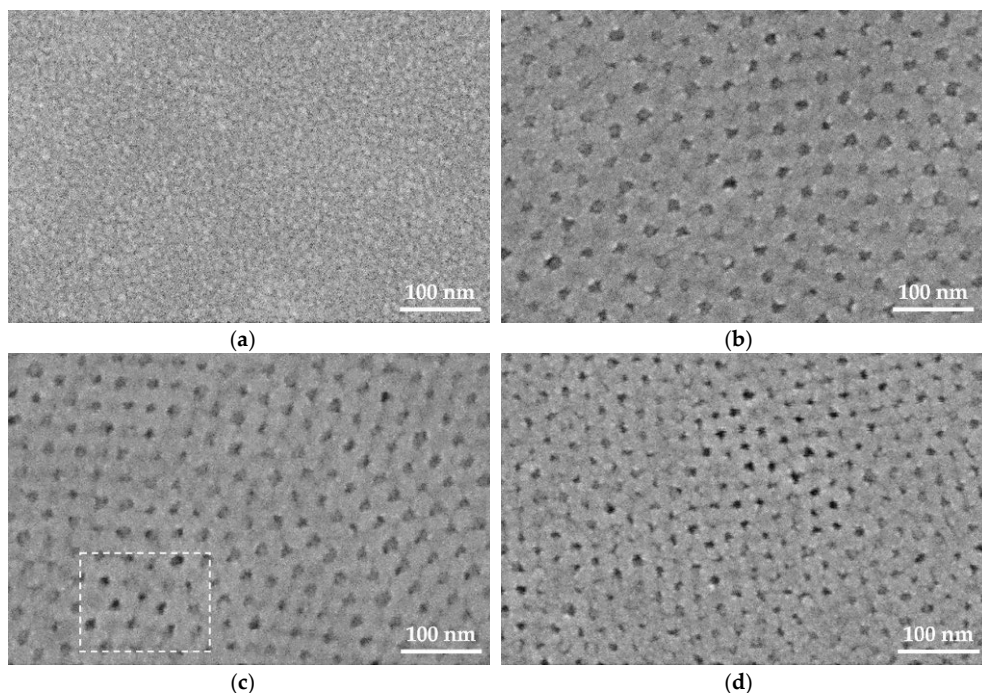


Figure 33. Top-view SEM images of the (a) Ti-0, (b) Ti-6, (c) Ti-12, and (d) Ti-21 samples. (reproduced from Study 3)

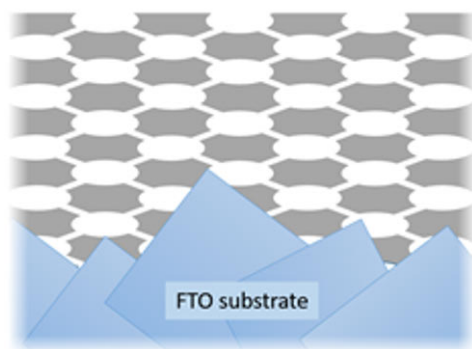


Fig 34. A schematic 2-D representation of a typical porous TiO_2 thin film deposited on top of a rough FTO substrate (note that the dimensions are not to scale). (reproduced from Study 3)

Before incorporating these films into devices, it is essential to verify the accessibility of the FTO substrate via pores from the top of TiO_2 films. For this purpose, the surface recombination velocity of holes at TiO_2 /FTO interface was determined in model devices where the p-type polymeric semiconductor, P3HT was coated on top of TiO_2 films with different porosities. P3HT was used because it is known to efficiently fill porous structures in comparison to the perovskite.^{232, 233, 234} A gold contact was then evaporated on top of the P3HT to form a hole-Ohmic contact. It was expected that greater the amount of P3HT forming a direct contact with underlying FTO, greater would be the rate of surface

recombination, since FTO does not block holes. MIS-CELIV measurements were performed on these samples to determine the surface recombination velocity of holes as a result of direct contact between P3HT and the underlying conductive FTO.²¹⁸ The calculated surface recombination velocities (S_R) for compact and porous TiO_2 films are shown in Figure 35. $S_R = 10^{-5}$ cm/s was obtained for Ti-0 sample which is slightly higher than previously reported values.²¹⁸ Furthermore, it was found that the S_R increases with an increase in the porosity. The Ti-6 sample was found to have a S_R value one order of magnitude higher than Ti-0 sample and when the porosity was further increased to Ti-21 sample, S_R increased by another order of magnitude. Such a drastic increase in S_R values can be attributed to P3HT reaching all the way through the porous channels in TiO_2 films down to the underlying FTO where recombination of holes is much faster than at the TiO_2 /P3HT interface. The sudden increase in S_R even at low porosity indicate the high possibility of P3HT coming in direct contact with the underlying FTO. With a further increase in porosity, there is a subsequent increase in number of the pathways down to the underlying FTO, which is seen as an increase in the S_R . This leaves us with the conclusion that the FTO substrate is accessible from the top of the porous TiO_2 films. The accessibility of the substrate through thinner block co-polymer-templated porous TiO_2 films has been studied earlier.^{235, 236} Thus, I believe that the ordered mesoporous TiO_2 films can be treated as model systems to study TiO_2 ESLs with narrow and well-defined pinholes.

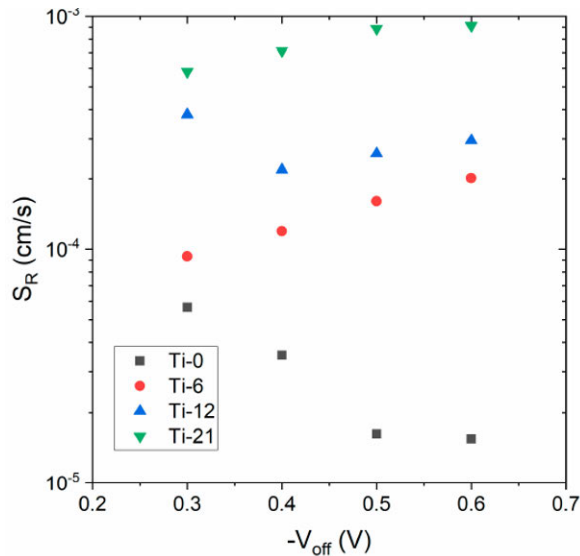


Fig 35. Calculated surface recombination velocities S_R for holes at the TiO_2 /P3HT interface from the MIS-CELIV data. S_R is given by $\frac{2\epsilon\epsilon_0 kT}{qQ_{\text{extr}}^2} J_D(V_{\text{off}})$, where $Q_{\text{extr}} = \int_0^{t_{\text{ext}}} j(t) - j_0 - J_D dt$, j_0 is the capacitive response and J_D the steady-state dark current before the voltage pulse. (reproduced from Study 3)

5.3.2. Shifting from 2-step sequential deposition of the perovskite to 1-step mixed ion perovskite via anti-solvent approach

The perovskite was deposited on Ti-12 mesoscopic layers using via 2-step sequential deposition method. Thereafter, the GI-XRD was performed at two different grazing incidence angles (0.5° and 1°) to qualitatively investigate the differences in the amount of unreacted PbI_2 at different depths of the

perovskite/TiO₂ composite film. The XRD diffractograms performed at two different grazing incidence angles are shown in Figure 36. For this sample, the peak intensities for (100) PbI₂ and (110) perovskite at 0.5° are nearly equal. The same thing was not observed for the perovskite deposited on particle-based 30 NRD mesoporous TiO₂ films (non-treated sample) discussed in Study 2 (see Figure 24 for comparison in section 5.2.1).

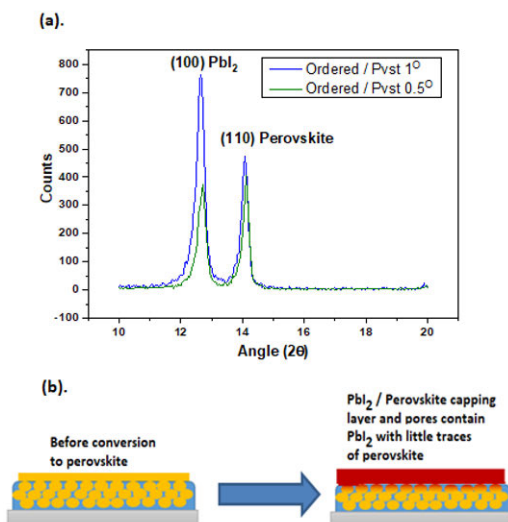


Fig 36. (a). XRD performed on 2-step perovskite coated on a 30-P2326 TiO₂ film at 1 and 0.5° grazing incident angle, to demonstrate the differences in PbI₂ content in the perovskite/TiO₂ composite. (b) Schematic explanation of the XRD data to show that there are only small amounts of the perovskite within the pores.

The peak intensity for the PbI₂ is nearly double in comparison to the intensity of the peak corresponding to the perovskite when the grazing incidence angle was increased to 1°. Thus, it is most likely that the upper-most portion of the thick capping layer of PbI₂ is converted to the perovskite, while a large portion of the underlying PbI₂ within the capping layer and the pores is left unconverted. It is evident from these results that the PbI₂-to-perovskite conversion is more efficient when using particle-based mesoporous TiO₂ film (which was used as a scaffold in Studies 1 and 2). This is probably because its structure is far more porous and open than the block co-polymer-templated ordered mesoporous films. Its high porosity supports the transportation of MAI solution to reach PbI₂ in large portion of the porous structure, while this is not the case for the ordered mesoporous films which are more compact and less porous.

The superficial conversion of PbI₂ to the perovskite is expected to give lower PCEs if the 2-step method is used to fabricate the solar cells. Furthermore, the large amount of residual PbI₂ can potentially create an additional barrier for the extraction of photogenerated electrons to the TiO₂ ESL. Therefore, perovskite deposition via the 2-step sequential deposition method is not suitable for making devices with ordered mesoporous TiO₂ layers. Thus, I decided to shift to a 1-step mixed cation/anion perovskite prepared via anti-solvent approach.¹¹¹

5.3.3. Device performance and discussion

In the next step, the non-porous TiO₂ reference sample and the ordered mesoporous TiO₂ films with different porosities were incorporated as ESLs in planar heterojunction PSCs. Theoretically, the pinholes in ESL can potentially allow the formation of parallel shunt pathways due to the creation of perovskite/FTO interfaces. Thus, the introduction of leakage currents into the device and non-geminate recombination at the perovskite/FTO interface result in reducing all photovoltaic parameters (i.e., J_{SC} , V_{OC} , and FF).²³⁷

The overall device structure is schematically shown in Figure 37 (a). Representative J-V curves under illumination for devices based on TiO₂ ESLs with different porosities are shown in Figure 37 (b). There were no large differences in the J-V curves as a function of film porosity. The values of PCE (in reverse sweep) as a function of porosity are plotted in Figure 37 (c) and summarized in Table 8. The devices based on dense compact TiO₂ (Ti-0) perform well with a PCE of $13.1 \pm 0.7\%$, which is slightly lower than the previously reported values for planar heterojunction PSCs.²³⁸ This could be attributed to the larger active area (about 0.126 cm²) and substrate size which can potentially increase the series resistance of the device. However, the reproducibility of the device performance is still very good, which is very important for this study.

The PCE remained almost unchanged upon increasing the porosity of the TiO₂ films. Unexpectedly, the highest average PCE ($13.8 \pm 0.7\%$) was achieved with the devices comprising of TiO₂ films with the highest porosity (Ti-21). The ordered porous network is expected to percolate through the entire film down to the underlying FTO substrate (which is evident from the MIS-CELIV measurements discussed in section 5.3.1.). If the perovskite is able to form a direct contact with the FTO by going through the porous structure, then this could potentially result in shunt pathways and deteriorate the device performance.²³⁹ However, it seems that the formation of detrimental pathways of the perovskite down to the FTO is being prevented by the narrow porous channels. It is quite well understood that the application of the anti-solvent (such as chlorobenzene or toluene) brings the perovskite precursor solution into a supersaturated state, which causes a rapid crystallization of perovskite. It can be hypothesized that the crystallization starts from the top of porous TiO₂ structure. Upon solvent evaporation, the initially crystallized perovskite potentially obstructs the pore opening so that the further infiltration of the perovskite precursor solution is not possible. It only tends to contribute to the perovskite capping layer on the top. The precursor solution which is initially able to enter the pores would later crystallize to the perovskite upon annealing. The resulting perovskite material is expected to only occupy 15-20 vol-% of the total volume of precursor solution (where solvent occupies the rest of the volume). This poorly crystallized perovskite in the porous channels is not enough to form percolating networks down to the underlying FTO and it will form isolated crystals of perovskite within the porous system (marked as 1 and 3 in Figure 38). However, there might be some regions such as the one marked as number 2 in Figure 44 where there is a good interconnection between the perovskite crystals reaching down to the FTO substrate. On the other hand, the nanoparticle-based mesoscopic TiO₂ layers (such as 30-NRD films which were used as scaffold in the previous studies for this thesis), the porous network within the film is highly accessible for the precursor solution and the anti-solvent, which would allow higher degree of pore filling by the continuous network of perovskite crystals reaching down to the bottom of the nanostructured film. In that case, an additional compact TiO₂ layer would be required to prevent the formation of direct shunt pathways between the perovskite and FTO.²⁴⁰

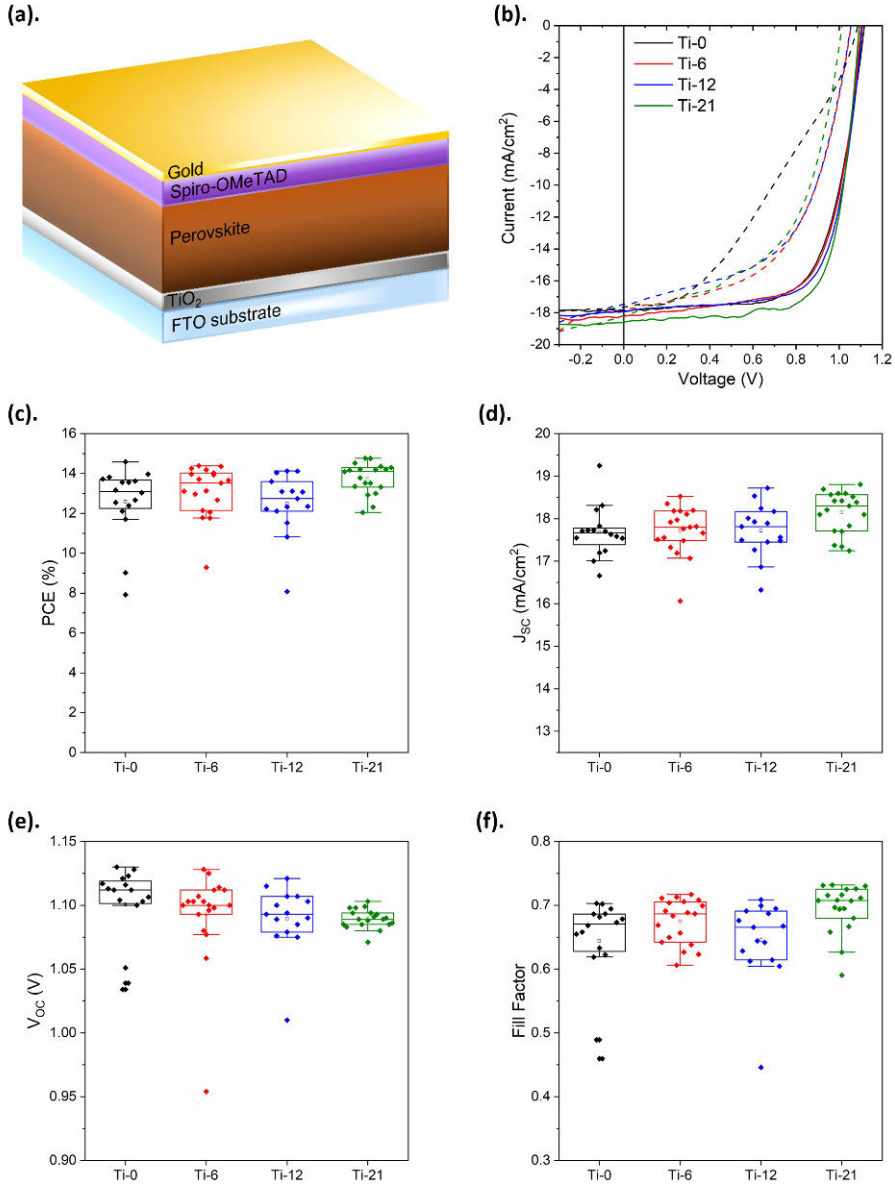


Fig 37. (a). Schematic illustration of the investigated device structures, where the TiO_2 ESL is either dense or porous. (b) Representative J-V curves in forward (dashed lines) and reverse (solid lines) sweep for devices with increasing porosity in the TiO_2 layer. Changes in (c) device efficiencies, (d) J_{sc} , (e) V_{oc} , and (f) FF for devices measured in reverse sweep with increase in porosity in the TiO_2 layer. (reproduced from Study 3)

Table 8. Mean values and standard deviations of photovoltaic parameters measured in reverse sweep of all type of devices.

Sample	No of devices	J_{sc} (mA/cm ²)	V_{oc} (V)	FF	PCE (%)
Ti-0	13	17.6 ± 0.4	1.11 ± 0.02	0.67 ± 0.03	13.1 ± 0.7
Ti-6	18	17.8 ± 0.4	1.10 ± 0.02	0.68 ± 0.03	13.3 ± 0.9
Ti-12	13	17.8 ± 0.5	1.10 ± 0.01	0.66 ± 0.03	13.0 ± 0.8
Ti-21	19	18.1 ± 0.5	1.09 ± 0.01	0.70 ± 0.03	13.8 ± 0.7
Ti-21-0.8	8	17.8 ± 0.3	1.05 ± 0.01	0.69 ± 0.02	12.9 ± 0.4
Ti-21-1.0	6	18.1 ± 0.1	1.08 ± 0.01	0.72 ± 0.004	14.1 ± 0.2
Ti-21-20	7	17.2 ± 2.0	1.01 ± 0.09	0.63 ± 0.11	11.0 ± 2.9

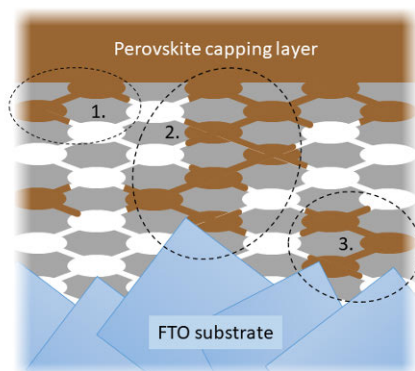


Fig 38. Suggested pore filling behavior of the perovskite inside the porous TiO₂ matrix. (reproduced from Study 3)

In the reverse sweep, a slight increase in J_{sc} with increase in porosity (from 17.5 mA/cm² to 18.5 mA/cm² for Ti-0 and Ti-21, respectively) can be observed. On the other hand, there is a marginal decrease in V_{oc} from 1.11 V down to 1.09 V for the same set of samples. The opposing trend in J_{sc} and V_{oc} seems to be the main reason behind the rather constant PCE for the devices with TiO₂ ESLs with different porosities. The increase in J_{sc} goes along with the increase in porosity and is probably related to an increase in the amount of perovskite accommodated in the porous films, such as the perovskite labelled “1” in Figure 38. However, no charges can be extracted from the isolated islands of perovskite such as the one labelled as “3”, and they are not expected to contribute to the short-circuit current

density. On the other hand, a considerable increase in the number of shunt pathways can be expected with an increase in the porosity (labelled “2” in Figure 38) which could possibly be the reason behind decrease in V_{oc} . Such perovskite pathways are expected to form in thinner regions of TiO_2 layer, which is caused by high surface roughness of the FTO substrate.

The influence of TiO_2 porosity on the electron injection from the conduction band (CB) of the perovskite to the CB of the TiO_2 layer was evaluated by performing the steady-state photoluminescence measurements on perovskite/glass and perovskite/ TiO_2 /glass samples (with different porosities of the TiO_2 layer). Figure 39 (a) shows the steady-state photoluminescence spectra for all the samples. The intensities of PL spectra for the perovskite-coated TiO_2 films are significantly lower in comparison to the spectrum for the perovskite-coated glass substrate. This shows a PL quenching effect of the perovskite coated on TiO_2 films in comparison to the reference perovskite on glass. The PL quenching efficiency (PLQE, also known as the electron-injection yield) was calculated as a function of TiO_2 porosity. The PLQE values increase with a decrease in porosity of the TiO_2 layer (see Figure 39 (a)). Thus, a lower porosity is favorable for an efficient electron-injection process.

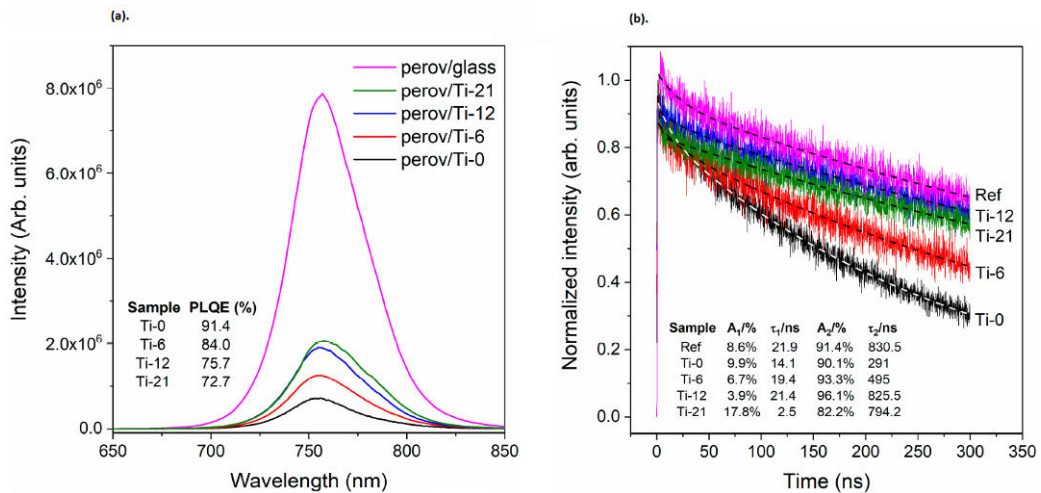


Fig 39. (a) Steady-state photoluminescence (PL) spectra of glass/perovskite and glass/ TiO_2 /perovskite with different porosities of the TiO_2 layer. The excitation wavelength was kept at 600 nm for all the samples. (b) Normalized time-resolved photoluminescence (TR-PL) decays on glass/perovskite (as reference) and glass/ TiO_2 /perovskite samples with different porosities of the TiO_2 layer. The bi-exponential fits of the original data are represented as dashed lines. The table summarizes the bi-exponential fittings of the photoluminescence decay based on the equation: $I(t) = A_1 \cdot e^{-t/\tau_1} + A_2 \cdot e^{-t/\tau_2}$. (reproduced from Study 3).

Thereafter, the charge transfer dynamics were assessed at the perovskite/ TiO_2 interface as a function of porosity. This was done by performing time-resolved photoluminescence measurements (TR-PL) on perovskite with and without TiO_2 films with different porosities. Figure 39(b) shows the bi-exponential fitted data of the PL decays for the perovskite/glass and perovskite/ TiO_2 /glass samples with different porosities of TiO_2 films. All PL decays of the perovskite/ TiO_2 /glass samples show an acceleration compared to the pristine perovskite coated on glass (which is the reference sample). This means that the interfacial electron-injection has occurred for all the samples where the perovskite is coated on TiO_2 /glass substrates which is also consistent with the steady-state PL measurements shown in Figure

39 (a). The deceleration of the decay profiles can be clearly observed with increase in porosity. However, the decay lifetimes for the samples with highest porosities (Ti-12 and Ti-21) are almost identical. Based on the global analysis methods,^{241, 242} the first component (A_1 , T_1) can be attributed to trap-state-mediated recombination and the second component (A_2 , T_2) to nongeminate free carrier recombination and the electron injection process from the CB of the perovskite to that of the TiO_2 film. The fittings suggest that the second component dominates the overall decay process, suggesting that a low porosity helps to suppress the charge recombination at perovskite/ TiO_2 interface which is manifested by enhanced V_{OC} .²⁴³ Another possible reason behind change in V_{OC} is that increased porosity can generate more traps on the TiO_2 structure which ultimately ends up in deepening of TiO_2 CB, which could intrinsically lower the V_{OC} .^{244, 245}

The fill factor (FF) values in the reverse sweep remains quite similar (in between 0.67 to 0.70) (Figure 37 (f)) and seems to be independent of porosity. However, larger differences can be observed when comparing the device hysteresis. As shown in Figure 37(b), an s-shaped feature can be observed in the forward sweep for dense compact TiO_2 layer (i.e. Ti-0 sample) while this feature does not appear in the reverse sweep. This results in a high hysteresis index of about 12% for Ti-0 samples. The s-shape and high hysteresis index are commonly reported in planar heterojunction PSCs with TiO_2 as an ESL.^{56, 239} Upon introducing pores in the TiO_2 layer, the s-shape feature in the forward sweep disappears and the fill factor is improved. However, the hysteresis index between the forward and reverse sweep still remain between 8 to 10%. This is also evident from the time-dependent current density measurements which were performed under illumination close to the maximum power point (MPP). These measurements are shown in Figure 40. More time is required for the device comprising of dense TiO_2 films to stabilize close to the MPP, while the devices based on porous TiO_2 films stabilize much faster and the current density values are also slightly enhanced at the MPP. This correlates very well with the J-V curves shown in Figure 43 (b) as the J_{SC} is slightly improved upon increasing the porosity of TiO_2 films.

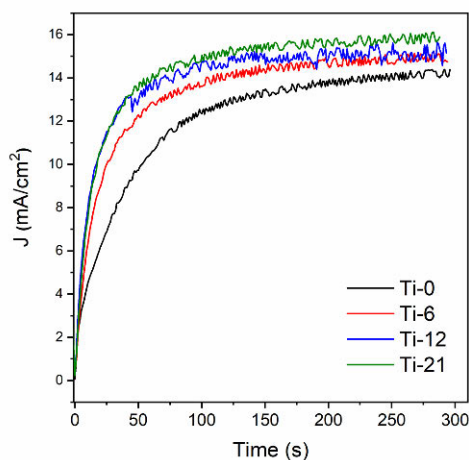


Fig 40. Time-dependent current density measurements performed close to the maximum power point (MPP) under illumination for the devices based on TiO_2 films with different porosities. (reproduced from Study 3)

As mentioned earlier, the increase in porosity resulted in a slight decrease in the TiO_2 film thickness, i.e., the Ti-0 sample is 75 nm thick, while the Ti-21 sample is 50 nm thick. Thus, in order to verify whether the observed changes in the device performance are an effect of porosity and not the change in film thickness, another series was made where the thickness of TiO_2 ESL was varied while keeping the block co-polymer to TiCl_4 ratio constant for Ti-21 sample. J-V curves for the devices with TiO_2 films of different thickness and similar porosity are shown in Figure 41 (a). The trends in the efficiencies are shown as a box chart in Figure 41 (b). All the devices based on different thickness of porous TiO_2 layer display fairly decent average device performance. The average device performance with 75 nm porous TiO_2 film (Ti-21-0.8) was slightly inferior (PCE = 12.9%) to that of the devices with 50 nm mesoporous TiO_2 layer (Ti-21-1.0) with a PCE of 14.1%. It is interesting to note that the devices with the 20 nm thickness also perform quite well with an average PCE of 11 %. However, on the basis of scattered data points in the box chart in Figure 41(b)) and the large standard deviations shown in Table 8, the thinnest sample undoubtedly suffer from poor reproducibility. This suggests that small variations in the TiO_2 film thickness can significantly influence the performance for this device structure.

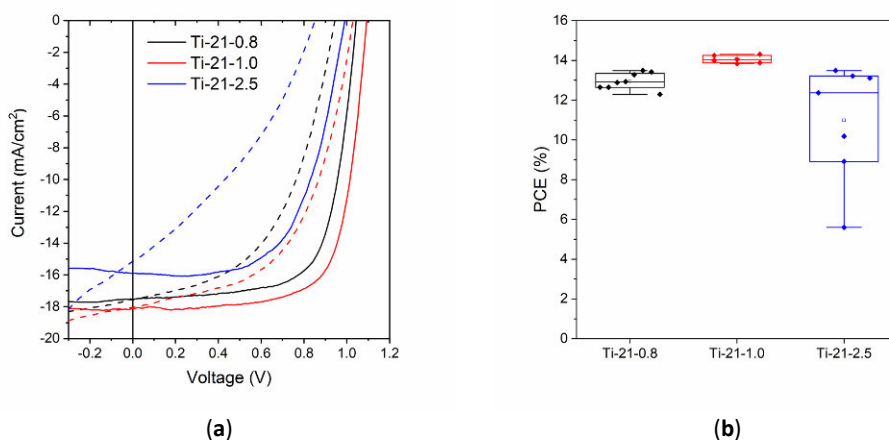


Fig 41. (a) J-V curves for representative devices based on TiO_2 ESLs with the highest porosity with different thicknesses; (b) Box chart for the efficiencies calculated from reverse sweep. (reproduced from Study 3)

For the thickness series, the porosity is roughly the same, and thus a similar interconnectivity of the perovskite inside the pores is expected. The extraction of electrons is relatively more difficult for thicker ESL like 75 nm Ti-21-0.8 film than the thinner one such as 50 nm Ti-21-1.0 sample.²³⁹ Too thick ESL layer can also reduce the light transmittance due to light scattering and absorption of photons with energies greater than the band gap of ESL material. This results in the reduction of number of photons to be absorbed by the active layer.^{180, 246} However, when the mesoporous TiO_2 film becomes too thin like 20 nm (Ti-21-2.5), more number of shunt pathways are to be expected because the pore channels become shallower perpendicular to FTO substrate. Some devices still perform well due to the high interfacial contact area at the perovskite/ESL interface and short distance for the transportation of electrons through the ESL. On the other hand, some devices suffer from direct shunt pathways which are formed by direct contact between the perovskite and FTO. Such bare patches are illustrated in Figure 38 and labelled as “2”. This results in large scattering of the data points and relatively larger standard deviations in the photovoltaic parameters. I have already reported in our first study for this

thesis that TiO_2 layers prepared via dip coating route should have a thickness of at least 30 nm for the optimal performance of mesoscopic PSCs. However, for the planar heterojunction PSCs, the TiO_2 layer need to be slightly thicker (around 50 nm) to avoid such pinholes which can potentially result in shunt pathways and deteriorate the device performance.

5.3.4. Conclusions from Study 3

In this study, a model system for pinholes was introduced containing compact TiO_2 ESLs where block co-polymers were used as templates to induce well-defined pores, which were expected to behave like pinholes in the ESL. It was observed that these so-called “induced” pinholes have a very small impact on the overall device performance, which is believed to be due to very few direct pathways of perovskite being able to reach the underlying FTO substrate via the ordered porous channels. Upon increasing the porosity, a slight increase in the J_{SC} with a decrease in V_{OC} was observed, which resulted in nearly constant PCE values. More interconnected perovskite pathways are expected to form when the porosity is higher, which could be the possible reason behind decrease in V_{OC} . For the 20 nm ultrathin TiO_2 films with highest porosity, there are large number of shallow regions of interconnected porous channels which facilitate the formation of large number of direct pathways of the perovskite to reach down to the FTO substrate.

6. Conclusions

The electron-selective layer is one of the key components of the PSCs, which allows the photo-generated electrons to be selectively extracted from the perovskite active layer. TiO_2 is one of the most commonly used ESL material due to its high chemical stability, transparency, tailorability in terms of its electronic properties, and compatibility in terms of its energy levels with the perovskite active layer. In this work, TiO_2 ESLs in both the mesoscopic as well as the planar heterojunction device architectures were studied. This thesis comprises of three different studies in which first two were based on the 2-step deposition method of the perovskite with a MAPbI_3 composition, while in the final study, a mixed ion perovskite was deposited using 1-step deposition via the anti-solvent approach.

In the **first study**, ultrathin compact TiO_2 layers were prepared and the minimum thickness when morphological defects such as pinholes disappear was determined. I learned that the thickness of the compact TiO_2 layer can be easily controlled by adjusting the concentration of TiCl_4 precursor in the dip coating sol. AFM measurements showed that the compact TiO_2 films cover the underlying rough FTO substrates quite well. With an increase in the precursor concentration, the compact TiO_2 layer starts to fill up the voids and subsequently tends to smoothen out the surface. This apparently coincides with the transformation from an amorphous to a crystalline anatase TiO_2 phase (according to the GI-XRD results). Sn signals in the XPS measurements can be correlated with pinholes in the thinnest compact TiO_2 layers. Devices without or with thin compact TiO_2 layers show s-shaped features in the negative voltage regime. This study supports the fact that immobile ions present at the exposed FTO surface are responsible for this s-shaped behavior. This means that not all of the photo-generated electrons in perovskite layer can be extracted in the positive voltage regime, which results in a lower J_{SC} and PCE of these devices. This study shows that a critical thickness of the compact TiO_2 layer must be reached in order to avoid pinholes. Nonetheless, these mesoscopic devices can still function relatively well even without a compact TiO_2 layer. However, by introducing a pinhole-free compact TiO_2 layer, the PCE increases from 5.5% to 8.6%.

Focal point of the **second study** was the subsequent mesoscopic layer based on TiO_2 nanoparticles. The TiO_2 mesoscopic layers were subjected to two different surface activation methods, which were found to significantly influence the performance of mesoscopic PSCs. The UV and plasma treatments tend to improve the wettability of the uppermost surface of mesoscopic TiO_2 layer, however the dye degradation test revealed that the penetration depth of different activation methods was quite diverse. Plasma treatment of the mesoscopic layer for only 5 min effectively activated all the interior and exterior surfaces of the mesoscopic layer. The irradiation of the TiO_2 mesoscopic layer with UV light (of $\lambda = 254$ nm) for 20 min only activated the top-most region of the porous films. The enhanced wettability upon plasma treatment resulted in a denser PbI_2 crystallization throughout the nanostructured TiO_2 film. This hampered the conversion of PbI_2 to the perovskite upon immersing the sample in the MAI solution. On the other hand, the UV irradiation only activated the top-most surface of the mesoscopic scaffold, thus the PbI_2 crystallized sparsely within the nanostructured TiO_2 layer. Therefore, the conversion of PbI_2 to the perovskite was not hampered upon immersion in MAI solution, while a good capping layer of the perovskite was formed on top of the activated mesostructured TiO_2 layer due to good wettability at its top-most surface. When incorporated into the devices, the PSCs based on plasma-treated scaffolds displayed much lower J_{SC} compared to non-treated samples, while J_{SC} was clearly enhanced for the samples prepared from UV-treated mesoporous TiO_2 films. Large differences in the J_{SC} could be attributed to the differences in PbI_2 -to-perovskite conversion efficiency

and partly to charge recombination. Furthermore, the V_{oc} increased from 0.91 to 0.96 V upon irradiating the mesoporous substrate with UV-light for 20 min. This effect can be attributed to an improved capping layer of the perovskite with less pinholes. These findings clearly illustrate the importance of processing parameters such as different surface activation methods and time as well as various storage and handling conditions.

In the **third study**, I synthesized the block co-polymer template ordered mesoporous TiO_2 films to use them as a model system for compact TiO_2 layers containing well-defined pinholes. The change in porosity was used to model the change in number of “induced” pinholes. The TiO_2 films with different porosities were incorporated into planar heterojunction PSCs to investigate the effect of film porosity on the device performance, which came out to be very small for thickness above 50 nm. This is most likely because of very few direct pathways of the perovskite reach the FTO substrate through the porous system. A slight increase in J_{sc} as well as decrease in V_{oc} was observed with increasing porosity; thus overall the PCE remained nearly the same. An increase in interconnected perovskite pathways down to the underlying FTO with an increase in porosity can explain both of these effects. However, the device reproducibility is affected for the sample with the highest porosity when its thickness is reduced to 20 nm. It can be speculated that upon reducing the thickness of highly porous films, there are more interconnected perovskite pathways reaching down to the FTO substrate. This is because there are bare patches in addition to the porous channels which facilitate the establishment of a large amount of such perovskite pathways reaching down to the FTO and causing excessive recombination at the perovskite/FTO interface.

7. References

1. Solar tube wells and solar water pumps. <https://www.premiereenergy.com.pk/solar-tubewell-in-pakistan/>, (accessed on 15.03.2020).
2. John Perlin Passive Solar History. <http://californiasolarcenter.org/history-pv/>, (accessed on 15.03.2020).
3. Lira-Cantu, M., Ed.; *The Future of Semiconductor Oxides in Next-Generation Solar Cells*; Korotcenkov, G., Ed.; Metal Oxide Series; Elsevier: 2017;.
4. How Round is the Sun. https://science.nasa.gov/science-news/science-at-nasa/2008/02oct_oblatesun/. (accessed on 15.03.2020)
5. First Ever STEREO Images of the Entire Sun. https://science.nasa.gov/science-news/science-at-nasa/2011/06feb_fullsun/. (accessed on 15.03.2020).
6. Rawat, P.; Performance Analysis of 300W Solar Photovoltaic Module under Varying Wavelength of solar Radiation. *International Journal for Research in Applied Science & Engineering Technology* **2017**, 5. (accessed on 15.03.2020)
7. Claus, F.; Lean, J.; Solar radiative output and its variability: evidence and mechanisms. *The Astronomy and Astrophysics review*, **2004**, 12, 273–320.
8. Loster, M.; Total Primary Energy Supply — From Sunlight. https://www.ez2c.de/ml/solar_land_area/. (accessed on 29.03.2020)
9. Schmalensee, R.; Bulovic, V.; Armstrong, R.; Batlle, C.; Brown, P.; Deutch, J.; Jacoby, H.; Jaffe, R.; Jean, J.; Miller, R.; O'Sullivan, F.; Parsons, J.; Perez-Arriga, I. J.; Seifkar, N.; Stoner, R.; Vergara, C.; The Future of Solar Energy: An interdisciplinary MIT Study. *Massachusetts Institute of Technology, MIT Energy Initiative*, **2015**.
10. Conibeer, G. J.; Willoghby, A. *Solar Cell Materials: Developing Technologies*. John Wiley & Sons, Ltd.; Chichester, UK, 2014; .
11. Krc, J.; Lipovsek, B.; Topic, M.; Light Management in thin-film solar cell. In *Next Generation of Photovoltaics*; Cristobal, L., Ana Belen, Vega, A. M. and Lopez, A. L., Eds.; Springer: 2012; pp 95-130.
12. Kirchartz, T.; Bisquert, J.; Mora-Sero, I.; Garcia-Belmonte, G.; Classification of solar cells according to mechanisms of charge separation and charge collection. *Physical chemistry chemical physics: PCCP*, **2015**, 17, 4007-4014.
13. Ibn-Mohammed, T.; Koh, S. C. L.; Reaney, I. M.; Acquaye, A.; Schileo, G.; Mustapha, K. B.; Greenough, R. Perovskite solar cells: An integrated hybrid lifecycle assessment and review in comparison with other photovoltaic technologies. *Renewable and Sustainable Energy Reviews*, **2017**, 80, 1321-1344.

14. Philipps, S.; ISE, F.; Warmuth, W. Photovoltaic Report. <https://www.ise.fraunhofer.de/content/dam/ise/de/documents/publications/studies/Photovoltaics-Report.pdf>. (accessed on 15.03.2020)
15. Vegad, M.; Bhatt, N. M.; Review of some Aspects of Single Crystal Growth Using Czochralski Crystal Growth Technique. *Procedia Technology*, **2014**, *14*, 438-446.
16. Goodrich, A.; Hacke, P.; Wang, Q.; Sopori, B.; Margolis, R.; James, T. L.; Woodhouse, M.; A wafer-based monocrystalline silicon photovoltaics road map: Utilizing known technology improvement opportunities for further reductions in manufacturing costs. *Solar Energy Materials and Solar Cells*, **2013**, *114*, 110-135.
17. Card, H. C.; Yang, E. S.; Electronic processes at grain boundaries in polycrystalline semiconductors under optical illumination. *TED*, **1977**, *24*, 397-402.
18. Best Research-Cell Efficiency Chart. <https://www.nrel.gov/pv/cell-efficiency.html>. (accessed on 20.03.2020)
19. Goldstein, M.; Watanabe, M.; 450 mm silicon wafers challenges – wafer thickness scaling. *ECS Transaction*, **2008**, *16*, 3-13.
20. Moon, S.; Kim, K.; Kim, Y.; Heo, J.; Lee, J.; Highly efficient single-junction GaAs thin-film solar cell on flexible substrate. *Scientific reports*, **2016**, *6*, 30107.
21. Bauhuis, G. J.; Mulder, P.; Haverkamp, E. J.; Huijben, J. C. C. M.; Schermer, J. J.; 26.1% thin-film GaAs solar cell using epitaxial lift-off. *Solar Energy Materials and Solar Cells*, **2009**, *93*, 1488-1491.
22. Green, M. A.; Hishikawa, Y.; Dunlop, E. D.; Levi, D. H.; Hohl-Ebinger, J.; Yoshita, M.; Ho-Baillie, A.; Solar cell efficiency tables (Version 53). *Progress in Photovoltaic: Research and Application.*, **2019**, *27*, 3-12.
23. Lorenz, P.; Pinner, D.; Seitz, T. The economics of solar power. *Energy, Resources, Materials*, **2008**.
24. Shah, A. V.; Schade, H.; Vanecek, M.; Meier, J.; Vallat-Sauvain, E.; Wyrsh, N.; Kroll, U.; Droz, C.; Bailat, J.; Thin-film silicon solar cell technology. *Progress in Photovoltaics: Research and Application.*, **2004**, *12*, 113-142.
25. Crandall, R. S.; Defect relaxation in amorphous silicon: Stretched exponentials, the Meyer-Neldel rule, and the Staebler-Wronski effect. *Physical Review B*, **1991**, *43*, 4057-4070.
26. McCandless, B. E.; Sites, J. R.; Cadmium Telluride Solar Cells. *Handbook of Photovoltaic Science and Engineering*, **2003**, 617-662.
27. Martin, R.; First Solar's Cells Break Efficiency Record, MIT Technology Review. <https://www.technologyreview.com/s/600922/first-solars-cells-break-efficiency-record/>. (accessed on 13.03.2020).
28. Green, M.; Thin-film solar cells: review of materials, technologies and commercial status. *Journal of Materials Science: Materials in Electronics*, **2007**, *18*, 15-19.

29. Romeo, A.; Terheggen, M.; Abou-Ras, D.; Bätzner, D. L.; Haug, F. -.; Kälin, M.; Rudmann, D.; Tiwari, A. N.; Development of thin-film Cu(In,Ga)Se₂ and CdTe solar cells. *Progress in Photovoltaics: Research and Application.*, **2004**, *12*, 93-111.
30. CIGS Thin-Film Photovoltaics. <https://cigs-pv.net/why-invest-in-cigs-thin-film-technology/02-applications/>. (accessed on 14.03.2020)
31. Conibeer, G.; Third-generation photovoltaics. *Materials Today*, **2007**, *10*, 42-50.
32. Asim, N.; Sopian, K.; Ahmadi, S.; Saeedfar, K.; Alghoul, M. A.; Saadatian, O.; Zaidi, S. H.; A review on the role of materials science in solar cells. *Renewable and Sustainable Energy Reviews*, **2012**, *16*, 5834-5847.
33. Shin, B.; Gunawan, O.; Zhu, Y.; Bojarczuk, N. A.; Chey, S. J.; Guha, S.; Thin film solar cell with 8.4% power conversion efficiency using an earth-abundant Cu₂ZnSnS₄ absorber. *Progress in Photovoltaics: Research and Application.*, **2013**, *21*, 72-76.
34. Todorov, T. K.; Reuter, K. B.; Mitzi, D. B.; High-Efficiency Solar Cell with Earth-Abundant Liquid-Processed Absorber. *Advanced Materials*, **2010**, *22*, E156-E159.
35. Kippelen, B.; Bredas, J.; Organic Photovoltaics. *Energy & Environmental Science*, **2009**, *2*, 251-261.
36. Brabec, C.; Scherf, U.; Dyakonov, V., Eds.; In *Organic Photovoltaics: Materials, Device Physics, and Manufacturing technologies*; Wiley-VCH Verlag GmbH & Co. KGaA, Weinheim: 2008; .
37. Zhan, X.; Zhu, D.; Conjugated polymers for high-efficiency organic photovoltaics. *Polymer Chemistry*, **2010**, *1*, 49-419.
38. Zhou, Y.; Fuentes-Hernandez, C.; Khan, T. M.; Liu, J.; Hsu, J.; Shim, J. W.; Dindar, A.; Youngblood, J. P.; Moon, R. J.; Kippelen, B.; Recyclable organic solar cells on cellulose nanocrystal substrates. *Scientific reports*, **2013**, *3*, 1536.
39. Carey, G. H.; Abdelhady, A. L.; Ning, Z.; Thon, S. M.; Bakr, O. M.; Sargent, E. H.; Colloidal Quantum Dot Solar Cells. *Chemical Reviews*, **2015**, *115*, 12732-12763.
40. Kamat, P. V.; Quantum Dot Solar Cells. Semiconductor Nanocrystals as Light Harvesters. *The Journal of Physical Chemistry C*, **2008**, *112*, 18737-18753.
41. Luque, A.; Martí, A.; Nozik, A. J.; Solar Cells Based on Quantum Dots: Multiple Exciton Generation and Intermediate Bands. *MRS Bull*, **2007**, *32*, 236-241.
42. Duan, J.; Zhang, H.; Tang, Q.; He, B.; Yu, L.; Recent advances in critical materials for quantum dot-sensitized solar cells: a review. *Journal of Materials Chemistry A*, **2015**, *3*, 17497-1751.
43. Hardin, B. E.; Snaith, H. J.; McGehee, M. D.; The Renaissance of Dye Sensitized Solar Cells. *Nature Photonics*, **2012**, *6*, 162-169.
44. Sugathan, V.; John, E.; Sudhakar, K.; Recent improvements in dye sensitized solar cells: A review. *Renewable and Sustainable Energy Reviews*, **2015**, *52*, 54-64.

45. Lee, C.; Li, C.; Ho, K.; Use of organic materials in dye-sensitized solar cells. *Materials Today*, **2017**, *20*, 267-283.
46. Moia, D.; Cappel, U. B.; Leijtens, T.; Li, X.; Telford, A. M.; Snaith, H. J.; O'Regan, B. C.; Nelson, J.; Barnes, P.; The role of hole transport between dyes in solid-state dye-sensitized solar cells. *Journal of Physical Chemistry C*, **2015**, *119*, 33, 18975-18985.
47. Hagfeldt, A.; Boschloo, G.; Sun, L.; Kloo, L.; Pettersson, H.; Dye-Sensitized Solar Cells. *Chemical Reviews*, **2010**, *110*, 6595-6663.
48. Shen, H.; Wu, Y.; Peng, J.; Duong, T.; Fu, X.; Barugkin, C.; White, T. P.; Weber, K.; Catchpole, K. R.; improved reproducibility for perovskite solar cells with 1 cm² active area by a modified two-step process. *ACS Applied Materials & Interfaces*, **2017**, *9*, 5974-5981.
49. Ramirez, D.; Velilla, E.; Montoya, J. F.; Jaramillo, F.; Mitigating scalability issues of perovskite photovoltaic technology through a p-i-n meso-superstructured solar cell architecture. *Solar Energy Materials and Solar Cells*, **2019**, *195*, 191-197.
50. Meng, L.; You, J.; Yang, Y.; Addressing the stability issue of perovskite solar cells for commercial applications. *Nature communications*, **2018**, *9*, 5265-4.
51. Kojima, A.; Teshima, K.; Shirai, Y.; Miyasaka, T.; Organometal Halide Perovskites as Visible-Light Sensitizers for Photovoltaic Cells. *Journal of the American Chemical Society*, **2009**, *131*, 6050-6051.
52. Saliba, M.; Correa-Baena, J.; Grätzel, M.; Hagfeldt, A.; Abate, A. Perovskite Solar Cells: From the atomic level to film quality and device performance. *Angew. Chem. Int. Ed.*, **2018**, *57*, 2554-2569.
53. Mahmood, K.; Sarwar, S.; Mehran, M. T.; Current status of electron transport layers in perovskite solar cells: materials and properties. *RSC Advances*, **2017**, *7*, 1744-1762.
54. Kajal, P.; Ghosh, K.; Powar, S.; Ed.; In *Manufacturing Techniques of Perovskite Solar Cells*; Tyagi, H.; Agarwal, A.; Chakraborty, P.; Powar, S.; Eds.; Applications of Solar Energy. Energy, Environment, and Sustainability; Springer: Singapore, 2018; , pp 341-364.
55. Calió, L.; Kazim, S.; Grätzel, M.; Ahmad, S.; Hole-Transport Materials for Perovskite Solar Cells. *Angew. Chem. Int. Ed.* **2016**, *55*, 14522-14545.
56. Correa Baena, J. P.; Steier, L.; Tress, W.; Saliba, M.; Neutzner, S.; Matsui, T.; Giordano, F.; Jacobsson, T. J.; Srimath Kandada, A. R.; Zakeeruddin, S. M.; Petrozza, A.; Abate, A.; Nazeeruddin, M. K.; Grätzel, M.; Hagfeldt, A.; Highly efficient planar perovskite solar cells through band alignment engineering. *Energy & Environmental Science*, **2015**, *8*, 2928-2934.
57. Liu, M.; Johnston, M. B.; Snaith, H. J.; Efficient planar heterojunction perovskite solar cells by vapour deposition. *Nature*, **2013**, *501*, 395-398.
58. Stranks, S.D.; Eperon, G.E.; Grancini, G.; Menelaou, C.; Alcocer, M.J.P.; Leijtens, T.; Herz, L.M.; Petrozza, A.; Snaith, H. J.; Electron-hole diffusion lengths exceeding 1 micrometer in an organometal trihalide perovskite absorber. *Science*, **2013**, *342*, 341-344.

59. Xing, G.; Mathews, N.; Sun, S.; Sien Lim, S.; Lam, Y.M.; Grätzel, M.; Mhaisalkar, S.; Sum, T.C.; Long-range balanced electron-and hole-transport lengths in organic-inorganic $\text{CH}_3\text{NH}_3\text{PbI}_3$. *Science*, **2013**, *342*, 344-347.
60. Meyer, J.; Kahn, A.; Electronic structure of molybdenum-oxide films and associated charge injection mechanisms in organic devices. *Journal of Photonics for Energy*, **2011**, *1*, 11109.
61. Greiner, M. T.; Chai, L.; Helander, M. G.; Tang, W.; Lu, Z.; Transition Metal Oxide Work Functions: The Influence of Cation Oxidation State and Oxygen Vacancies. *Advanced Functional Materials*, **2012**, *22*, 4557-4568.
62. Schulz, P.; Tiepelt, J. O.; Christians, J. A.; Levine, I.; Edri, E.; Sanehira, E. M.; Hodes, G.; Cahen, D.; Kahn, A.; High work function Molybdenum Oxide hole extraction contacts in hybrid organic-inorganic Perovskite solar cells. *ACS Applied Materials & Interfaces*, **2016**, *8*, 31491–31499.
63. Stranks, S. D.; Snaith, H. J.; Metal-halide perovskites for photovoltaic and light-emitting devices. *Nature nanotechnology*, **2015**, *10*, 391-402.
64. Zhu, B.; Huang, Y.; Fan, L.; Ma, Y.; Wang, B.; Xia, C.; Afzal, M.; Zhang, B.; Dong, W.; Wang, H.; Lund, P. D.; Novel fuel cell with nanocomposite functional layer designed by perovskite solar cell principle. *Nano Energy*, **2016**, *19*, 156-164.
65. Im, J.; Lee, C.; Lee, J.; Park, S.; Park, N.; 6.5% efficient perovskite quantum-dot-sensitized solar cell. *Nanoscale*, **2011**, *3*, 4088-4093.
66. Kim, H.; Lee, C.; Im, J.; Lee, K.; Moehl, T.; Marchioro, A.; Moon, S.; Humphry-Baker, R.; Yum, J.; Moser, J. E.; Grätzel, M.; Park, N.; Lead Iodide Perovskite Sensitized All-Solid-State Submicron Thin Film Mesoscopic Solar Cell with Efficiency Exceeding 9. *Scientific reports*, **2012**, *2*, 591.
67. Lee, M.M.; Teuscher, J.; Miyasaka, T.; Murakami, T.N.; Snaith, H.J.; Efficient Hybrid Solar Cells Based on Meso-Superstructured Organometal Halide Perovskites. *Science*, **2012**, *338*, 643-647.
68. Heo, J. H.; Im, S. H.; Noh, J. H.; Mandal, T. N.; Lim, C.; Chang, J. A.; Lee, Y. H.; Kim, H.; Sarkar, A.; Nazeeruddin, M. K.; Grätzel, M.; Seok, S. I.; Efficient inorganic–organic hybrid heterojunction solar cells containing perovskite compound and polymeric hole conductors. *Nature Photonics*, **2013**, *7*.
69. Burschka, J.; Pellet, N.; Moon, S.; Humphry-Baker, R.; Gao, P.; Nazeeruddin, M. K.; Grätzel, M.; Sequential deposition as a route to high-performance perovskite-sensitized solar cells. *Nature*, **2013**, *499*, 316-319.
70. Liu, M.; Johnston, M.B.; Snaith, H.J.; Efficient planar heterojunction perovskite solar cells by vapour deposition. *Nature*, **2013**, *501*, 395-398.
71. Park, N.; Perovskite solar cells: an emerging photovoltaic technology. *Materials Today* **2015**, *18*, 65-72.
72. Stoumpos, C. C.; Malliakas, C. D.; Kanatzidis, M. G.; Semiconducting tin and lead iodide perovskites with organic cations: phase transitions, high mobilities, and near-infrared photoluminescent properties. *Inorganic chemistry*, **2013**, *52*, 9019-9038.

73. Ogomi, Y.; Morita, A.; Tsukamoto, S.; Saitho, T.; Fujikawa, N.; Shen, Q.; Toyoda, T.; Yoshino, K.; Pandey, S. S.; Ma, T.; Hayase, S. $\text{CH}_3\text{NH}_3\text{Sn}_x\text{Pb}_{(1-x)}\text{I}_3$ Perovskite Solar Cells Covering up to 1060 nm. *Journal of Physical Chemistry Letter*, **2014**, *5*, 1004-1011.
74. Yamada, Y.; Nakamura, T.; Endo, M.; Wakamiya, A.; Kanemitsu, Y.; Photocarrier Recombination Dynamics in Perovskite $\text{CH}_3\text{NH}_3\text{PbI}_3$ for Solar Cell Applications. *Journal of the American Chemical Society*, **2014**, *136*, 11610-11613.
75. Singh, S. P.; Nagarjuna, P.; Organometal halide perovskites as useful materials in sensitized solar cells. *Dalton Transactions*, **2014**, *43*, 5247-5251.
76. Umari, P.; Mosconi, E.; De Angelis, F.; Relativistic GW calculations on $\text{CH}_3\text{NH}_3\text{PbI}_3$ and $\text{CH}_3\text{NH}_3\text{SnI}_3$ Perovskites for Solar Cell Applications. *Scientific Reports*, **2014**, *Open access*, 4:4467.
77. Sum, T. C.; Mathews, N.; Xing, G.; Lim, S. S.; Chong, W. K.; Giovanni, D.; Dewi, H. A.; Spectral Features and Charge Dynamics of Lead Halide Perovskites: Origins and Interpretations. *Accounts of chemical research*, **2016**, *49*, 294-302.
78. Slavney, A. H.; Leppert, L.; Bartesaghi, D.; Gold-Parker, A.; Toney, M. F.; Savenije, T. J.; Neaton, J. B.; Karunadasa, H. I.; Defect-Induced Band-Edge Reconstruction of a Bismuth-Halide Double Perovskite for Visible-Light Absorption. *Journal of the American Chemical Society*, **2017**, *139*, 5015-5018.
79. Li, M.; Zhao, C.; Wang, Z.; Zhang, C.; Lee, H. K. H.; Pockett, A.; Barbé, J.; Tsoi, W. C.; Yang, Y.; Carnie, M. J.; Gao, X.; Yang, W.; Durrant, J. R.; Liao, L.; Jain, S. M.; Interface Modification by Ionic Liquid: A Promising Candidate for Indoor Light Harvesting and Stability Improvement of Planar Perovskite Solar Cells. *Advanced Energy Materials*, **2018**, *8*, 1801509.
80. Liu, D.; Kelly, T. L.; Perovskite solar cells with a planar heterojunction structure prepared using room-temperature solution processing techniques. *Nature Photonics*, **2014**, *8*, 133-138.
81. Jung, J. W.; Chueh, C.; Jen, A. K.; A Low-Temperature, Solution-Processable, Cu-Doped Nickel Oxide Hole-Transporting Layer via the Combustion Method for High-Performance Thin-Film Perovskite Solar Cells. *Advanced Materials*, **2015**, *27*, 7874-7880.
82. Johansson, M.; Lemmens, P.; Crystallography and Chemistry of Perovskites. In: Handbook of magnetism and advanced magnetic materials, **2007**.
83. Chemical Structure, <https://chemicalstructure.net/portfolio/perovskite/>. (accessed on 04.12.2019).
84. Mitzi, D. B.; Feild, C. A.; Harrison, W. T. A.; Guloy, A. M.; Conducting tin halides with a layered organic-based perovskite structure. *Nature*, **1994**, *369*, 467-469.
85. Mitzi, D. B.; Templating and structural engineering in organic-inorganic perovskites. *Journal of the Chemical Society, Dalton Transactions*, **2001**, 1-12.
86. Frost, J. M.; Butler, K. T.; Brivio, F.; Hendon, C. H.; Schilfgaarde, M. van.; Walsh, A.; Atomistic origins of high-performance in hybrid halide perovskite solar cells. *Nano letters*, **2014**, *14*, 2584-2590.

87. Li, W.; Zhang, Z.; Bithell, E. G.; Batsanov, A. S.; Barton, P. T.; Saines, P. J.; Jain, P.; Howard, C. J.; Carpenter, M. A.; Cheetham, A. K.; Ferroelasticity in a metal–organic framework perovskite; towards a new class of multiferroics. *Acta Materialia*, **2013**, *61*, 4928-4938.
88. Cairns, A. B.; Goodwin, A. L.; Structural disorder in molecular framework materials. *Chemical Society Reviews*, **2013**, *42*, 4881-4893.
89. Weber, D.; $\text{CH}_3\text{NH}_3\text{PbX}_3$, ein Pb(II)-System mit kubischer Perowskitstruktur. *Z. Naturforsch*, **1978**, *33b*, 1443-1445.
90. Jeon, N. J.; Noh, J. H.; Kim, Y. C.; Yan, W. S.; Ryu, S.; Seok, S. I.; Solvent engineering for high-performance inorganic-organic hybrid perovskite solar cells. *Nature Materials*, **2014**, *13*, 897-903.
91. Baikie, T.; Fang, Y.; Kadro, J. M.; Schreyer, M.; Wei, F.; Mhaisalkar, S. G.; Graetzel, M.; White, T. J.; Synthesis and crystal chemistry of the hybrid perovskite $(\text{CH}_3\text{NH}_3)\text{PbI}_3$ for solid-state sensitized solar cell applications. *Journal of Materials Chemistry A*, **2013**, *1*, 5628-5641.
92. Yang, C.; El-Demellawi, J. K.; Yin, J.; Velusamy, D. B.; Emwas, A. M.; El-Zohry, A. M.; Gereige, I.; AlSaggaf, A.; Bakr, O. M.; Alshareef, H. N.; Mohammed, O. F.; MAPbI_3 Single Crystals Free from Hole-Trapping Centers for Enhanced Photodetectivity. *ACS Energy Letters*, **2019**, *4*, 2579-2584.
93. Liu, C.; Hu, M.; Zhou, X.; Wu, J.; Zhang, L.; Kong, W.; Li, X.; Zhao, X.; Dai, S.; Xu, B.; Cheng, C.; Efficiency and stability enhancement of perovskite solar cells by introducing CsPbI_3 quantum dots as an interface engineering layer. *NPG Asia Materials* **2018**, *10*, 552-561.
94. Yang, H.; Zhang, J.; Zhang, C.; Chang, J.; Lin, Z.; Chen, D.; Xi, H.; Hao, Y. Effects of Annealing Conditions on Mixed Lead Halide Perovskite Solar Cells and Their Thermal Stability Investigation. *Materials (Basel, Switzerland)*, **2017**, *10*, 837.
95. Wu, M.; Kuo, C.; Jhuang, L.; Chen, P.; Lai, Y.; Chen, F.; Bandgap Engineering Enhances the Performance of Mixed-Cation Perovskite Materials for Indoor Photovoltaic Applications. *Advanced Energy Materials*, **2019**, *9*, 1901863.
96. Arora, N.; Dar, M. I.; Hinderhofer, A.; Pellet, N.; Schreiber, F.; Zakeeruddin, S. M.; Grätzel, M.; Perovskite solar cells with CuSCN hole extraction layers yield stabilized efficiencies greater than 20. *Science (New York, N.Y.)*, **2017**, *358*, 768-771.
97. Yang, G.; Chen, C.; Yao, F.; Chen, Z.; Zhang, Q.; Zheng, X.; Ma, J.; Lei, H.; Qin, P.; Xiong, L.; Ke, W.; Li, G.; Yan, Y.; Fang, G.; Effective Carrier-Concentration Tuning of SnO_2 Quantum Dot Electron-Selective Layers for High-Performance Planar Perovskite Solar Cells. *Advanced Materials*, **2018**, *30*, 1706023.
98. Goldschmidt, V. M. Die Gesetze Der Krystallochemie (The Laws of Crystallochemistry). *Naturwissenschaften*, **1926**, *14*, 477-485.
99. Li, Z.; Yang, M.; Park, J.; Wei, S.; Berry, J. J.; Zhu, K.; Stabilizing perovskite structures by tuning tolerance factor: formation of formamidinium and cesium lead iodide solid-state alloys. *Chemistry of Materials*, **2016**, *28*, 284-292.
100. Dong, C.; Wang, Z.; Liao, L. Progress of Triple Cation Organometal Halide Perovskite Solar Cells. *Energy Technology*, **2019**, *n/a*, 1900804.

101. Pellet, N.; Gao, P.; Gregori, G.; Yang, T.; Nazeeruddin, M. K.; Maier, J.; Grätzel, M.; Mixed-Organic-Cation Perovskite Photovoltaics for Enhanced Solar-Light Harvesting. *Angew. Chem. Int. Ed.*, **2014**, *53*, 3151-3157.
102. Han, Y.; Meyer, S.; Dkhissi, Y.; Weber, K.; Pringle, J. M.; Bach, U.; Spiccia, L.; Cheng, Y.; Degradation observations of encapsulated planar CH₃NH₃PbI₃ perovskite solar cells at high temperatures and humidity. *Journal of Materials Chemistry A*, **2015**, *3*, 8139-8147.
103. Conings, B.; Drijkoningen, J.; Gauquelin, N.; Babayigit, A.; D'Haen, J.; D'Olieslaeger, L.; Ethirajan, A.; Verbeeck, J.; Manca, J.; Mosconi, E.; Angelis, F. D.; Boyen, H.; Intrinsic Thermal Instability of Methylammonium Lead Trihalide Perovskite. *Advanced Energy Materials*, **2015**, *5*, 1500477.
104. Aristidou, N.; Sanchez-Molina, I.; Chotchuangchutchaval, T.; Brown, M.; Martinez, L.; Rath, T.; Haque, S. A.; The Role of Oxygen in the Degradation of Methylammonium Lead Trihalide Perovskite Photoactive Layers. *Angewandte Chemie*, **2015**, *127*, 8326-8330.
105. Jung, M.; Shin, T. J.; Seo, J.; Kim, G.; Seok, S. I.; Structural features and their functions in surfactant-armed methylammonium lead iodide perovskites for highly efficient and stable solar cells. *Energy & Environmental Science*, **2018**, *11*, 2188-2197.
106. Anh, N.; Kwak, K.; Jang, M.S.; Yoon, H.; Lee, B. Y.; Lee, J.-k.; Pikhitsa, P.V.; Byun, J.; Choi, M.; Trapped charge-driven degradation of perovskite solar cells. *Nature Communications*, **2016**, *7*, 13422.
107. Merdasa, A.; Bag, M.; Tian, Y.; Källman, E.; Dobrovolsky, A.; Scheblykin, I. G.; Super-Resolution Luminescence Microspectroscopy Reveals the Mechanism of Photoinduced Degradation in CH₃NH₃PbI₃ Perovskite Nanocrystals. *The Journal of Physical Chemistry C*, **2016**, *120*, 10711-10719.
108. Christians, J. A.; Miranda Herrera, P. A.; Kamat, P. V.; Transformation of the excited state and photovoltaic efficiency of CH₃NH₃PbI₃ perovskite upon controlled exposure to humidified air. *Journal of the American Chemical Society*, **2015**, *137*, 1530-1538.
109. Bella, F.; Renzi, P.; Cavallo, C.; Gerbaldi, C.; Caesium for Perovskite Solar Cells: An Overview. *Chemistry European Journal*, **2018**, *24*, 12183-12205.
110. Zheng, X.; Wu, C.; Jha, S. K.; Li, Z.; Zhu, K.; Priya, S.; Improved Phase Stability of Formamidinium Lead Triiodide Perovskite by Strain Relaxation. *ACS Energy Letters* **2016**, *1*, 1014-1020.
111. Saliba, M.; Matsui, T.; Seo, J.; Domanski, K.; Correa-Baena, J.; Nazeeruddin, M. K.; Zakeeruddin, S. M.; Tress, W.; Abate, A.; Hagfeldt, A.; Grätzel, M. Cesium-containing triple cation perovskite solar cells: improved stability, reproducibility and high efficiency. *Energy & Environmental Science*, **2016**, *9*, 1989-1997.
112. Svane, K. L.; Forse, A. C.; Grey, C. P.; Kieslich, G.; Cheetham, A. K.; Walsh, A.; Butler, K. T. How Strong Is the Hydrogen Bond in Hybrid Perovskites? *The journal of physical chemistry letters*, **2017**, *8*, 6154-6159.
113. Noh, J. H.; Hyuk Im, Sang, Hyuck Heo, Jin; Mandal, T. N.; Seok, S. I.; Chemical Management for Colorful, Efficient, and Stable Inorganic-Organic Hybrid Nanostructured Solar Cells. *Nano Letters*, **2013**, *13*, 1764-1769.

114. Umebayashi, T.; Asai, K.; Kondo, T.; Nakao, A.; Electronic structures of lead iodide based low-dimensional crystals. *Physical Review B*, **2003**, 67, 155405.
115. Chen, K.; Wu, P.; Yang, W.; Su, R.; Luo, D.; Yang, X.; Tu, Y.; Zhu, R.; Gong, Q. Low-dimensional perovskite interlayer for highly efficient lead-free formamidinium tin iodide perovskite solar cells. *Nano Energy*, **2018**, 49, 411-418.
116. Giustino, F.; Snaith, H. J.; Toward Lead-Free Perovskite Solar Cells. *ACS Energy Letters*, **2016**, 1, 1233–1240.
117. Zhao, Z.; Gu, F.; Li, Y.; Sun, W.; Ye, S.; Rao, H.; Liu, Z.; Bian, Z.; Huang, C. Mixed-Organic-Cation Tin Iodide for Lead-Free Perovskite Solar Cells with an Efficiency of 8.12%. *Advanced Science*, **2017**, 4, 1700204.
118. Noel, N. K.; Stranks, S. D.; Abate, A.; Wehrenfenning, C.; Guarnera, S.; Haghighirad, A.; Sadhanala, A.; Eperon, G. E.; Pathak, S. K.; Johnston, M. B.; Petrozza, A.; Herz, L. M.; Snaith, H. J.; Lead-free organic–inorganic tin halide perovskites for photovoltaic applications. *RSC Energy & Environmental Science*, **2014**, 7, 3061-3068.
119. Zheng, Y.; Su, R.; Xu, Z.; Luo, D.; Dong, H.; Jiao, B.; Wu, Z.; Gong, Q.; Zhu, R.; Perovskite solar cell towards lower toxicity: a theoretical study of physical lead reduction strategy. *Science Bulletin*, **2019**, 64, 1255-1261.
120. Saliba, M.; Correa-Baena, J.; Wolff, C. M.; Stolterfoht, M.; Phung, N.; Albrecht, S.; Neher, D.; Abate, A.; How to Make over 20% Efficient Perovskite Solar Cells in Regular (n–i–p) and Inverted (p–i–n) Architectures. *Chemistry of Materials*, **2018**, 30, 4193-4201.
121. Ameen, S.; Akhtar, M. S.; Shin, H.; Nazeeruddin, M. K.; Charge-Transporting Materials for Perovskite Solar Cells. In *Advances in inorganic Chemistry, Materials for sustainable energy*; Eldik, R. V., Macyk, W., Eds.; Elsevier Academic Press (AP): 2018; pp 185-246.
122. Barbé, J.; Tietze, M. L.; Neophytou, M.; Murali, B.; Alarousu, E.; Labban, A. E.; Abulikemu, M.; Yue, W.; Mohammed, O. F.; McCulloch, I.; Amassian, A.; Del Gobbo, S.; Amorphous Tin Oxide as a Low-Temperature-Processed Electron-Transport Layer for Organic and Hybrid Perovskite Solar Cells. *ACS Applied Materials & Interfaces*, **2017**, 9, 11828-11836.
123. Ke, W.; Fang, G.; Wang, J.; Qin, P.; Tao, H.; Lei, H.; Liu, Q.; Dai, X.; Zhao, X.; Perovskite Solar Cell with an Efficient TiO₂ Compact Film. *ACS applied materials & interfaces*, **2014**, 6, 15959-15965.
124. Chen, S.; Hou, Y.; Chen, H.; Richter, M.; Guo, F.; Kahmann, S.; Tang, X.; Stubhan, T.; Zhang, H.; Li, N.; Gasparini, N.; Quiroz, C. O. R.; Khanzada, L. S.; Matt, G. J.; Osvet, A.; Brabec, C. J.; Exploring the Limiting Open-Circuit Voltage and the Voltage Loss Mechanism in Planar CH₃NH₃PbBr₃ Perovskite Solar Cells. *Advanced Energy Materials*, **2016**, 6, 1600132.
125. Elumalai, N. K.; Uddin, A.; Open circuit voltage of organic solar cells: an in-depth review. *Energy & Environmental Science*, **2016**, 9, 391-41.
126. Shao, Y.; Yuan, Y.; Huang, J.; Correlation of energy disorder and open-circuit voltage in hybrid perovskite solar cells. *Nature Energy*, **2016**, 1, 15001.

127. Zhang, M.; Chen, T.; Wang, Y.; Insights into TiO₂ polymorphs: highly selective synthesis, phase transition, and their polymorph-dependent properties. *RSC Advances*, **2017**, *7*, 52755-52761.
128. Roose, B.; Wang, Q.; Abate, A.; The Role of Charge Selective Contacts in Perovskite Solar Cell Stability. *Advanced Energy Materials*, **2019**, *9*, 1803140.
129. Li, J.; Ishigaki, T.; Sun, X.; Anatase, Brookite, and Rutile Nanocrystals via Redox Reactions under Mild Hydrothermal Conditions: Phase-Selective Synthesis and Physicochemical Properties. *Journal of Physical Chemistry C*, **2007**, *111*, 4969-4976.
130. Shahiduzzaman, M.; Visal, S.; Kuniyoshi, M.; Kaneko, T.; Umezu, S.; Katsumata, T.; Iwamori, S.; Kakihana, M.; Taima, T.; Isomura, M.; Tomita, K.; Low-Temperature-Processed Brookite-Based TiO₂ Heterophase Junction Enhances Performance of Planar Perovskite Solar Cells. *Nano Letters*, **2019**, *19*, 598-604.
131. Lee, J.; Lee, T.; Yoo, P. J.; Grätzel, M.; Mhaisalkar, S.; Park, N.; Rutile TiO₂-based perovskite solar cells. *Journal of Materials Chemistry A*, **2014**, *2*, 9251-9259.
132. Xu, J.; Wu, S.; Ri, J. H.; Jin, J.; Peng, T.; Bilayer film electrode of brookite TiO₂ particles with different morphology to improve the performance of pure brookite-based dye-sensitized solar cells. *Journal of Power Sources*, **2016**, *327*, 77-85.
133. Jeong, E.; Bae, S.; Park, J. B.; Yu, S. M.; Kim, D.; Lee, H.; Rha, J.; Cho, Y.; Yun, J.; Pinhole-free TiO₂/Ag(O)/ZnO configuration for flexible perovskite solar cells with ultralow optoelectrical loss. *RSC Advances*, **2019**, *9*, 9160-9170.
134. Lan, F.; Jiang, M.; Li, G.; The characterization of defects states and charge injection barriers in perovskite solar cells. *2017 IEEE 17th International Conference on Nanotechnology (IEEE-NANO)*, **2017**, 379-382.
135. Yang, G.; Tao, H.; Qin, P.; Ke, W.; Fang, G.; Recent progress in electron transport layers for efficient perovskite solar cells. *Journal of Materials Chemistry A*, **2016**, *4*, 3970-3990.
136. Ren, H.; Zou, X.; Cheng, J.; Ling, T.; Bai, X.; Chen, D.; Facile Solution Spin-Coating SnO₂ Thin Film Covering Cracks of TiO₂ Hole Blocking Layer for Perovskite Solar Cells. *Coatings*, **2018**, *8*, 314.
137. Byrannvand, M. M.; Kim, T.; Song, S.; Kang, G.; Ryu, S. U.; Park, T.; p-Type CuI Islands on TiO₂ Electron Transport Layer for a Highly Efficient Planar-Perovskite Solar Cell with Negligible Hysteresis. *Advanced Energy Materials*, **2018**, *8*, 1702235.
138. McDonald, C.; Ni, C.; Maguire, P.; Connor, P.; Irvine, J.; Mariotti, D.; Svrcek, V.; Nanostructured Perovskite Solar Cells. *Nanomaterials*, **2019**, *9*, 1481.
139. Byrannvand, M. M.; Song, S.; Pyeon, L.; Kang, G.; Lee, G.; Park, T.; Simple post annealing-free method for fabricating uniform, large grain-sized, and highly crystalline perovskite films. *Nano Energy*, **2017**, *34*, 181-187.
140. Rapsomanikis, A.; Karageorgopoulos, D.; Lianos, P.; Stathatos, E.; High performance perovskite solar cells with functional highly porous TiO₂ thin films constructed in ambient air. *Solar Energy Materials Solar Cells*, **2016**, *151*, 36-43.

141. Chung, C.; Lee, C. S.; Jokar, E.; Kim, J. H.; Diau, E. W. Well-Organized Mesoporous TiO₂ Photoanode by Using Amphiphilic Graft Copolymer for Efficient Perovskite Solar Cells. *Journal of Physical Chemistry C*, **2016**, 120, 9619-9627.
142. Sun, X.; Xu, J.; Xiao, L.; Chen, J.; Zhang, B.; Yao, J.; Dai, S.; Influence of the Porosity of the TiO₂ Film on the Performance of the Perovskite Solar Cell. *International Journal of Photoenergy*, **2017**, 2017, 1-10.
143. Shao, J.; Yang, S.; Lei, L.; Cao, Q.; Yu, Y.; Liu, Y.; Pore Size Dependent Hysteresis Elimination in Perovskite Solar Cells Based on Highly Porous TiO₂ Films with Widely Tunable Pores of 15–34 nm. *Chemistry of Materials*, **2016**, 28, 7134-7144.
144. Seyed-Talebi, S.; Kazeminezhad, I.; Shahbazi, S.; Diau, E. W.; Efficiency and Stability Enhancement of Fully Ambient Air Processed Perovskite Solar Cells Using TiO₂ Paste with Tunable Pore Structure. *Advanced Materials & Interfaces*, **2019**, 1900939.
145. Sarkar, A.; Jeon, N. J.; Noh, J. H.; Seok, S. I.; Well-Organized Mesoporous TiO₂ Photoelectrodes by Block Copolymer-Induced Sol–Gel Assembly for Inorganic–Organic Hybrid Perovskite Solar Cells. *The Journal of Physical Chemistry C*, **2014**, 118, 16688-16693.
146. Giordano, F.; Abate, A.; Correa Baena, J. P.; Saliba, M.; Matsui, T.; Im, S. H.; Zakeeruddin, S. M.; Nazeeruddin, M. K.; Hagfeldt, A.; Graetzel, M.; Enhanced electronic properties in mesoporous TiO₂ via lithium doping for high-efficiency perovskite solar cells. *Nature communications*, **2016**, 7, 10379.
147. Macdonald, T. J.; Batmunkh, M.; Lin, C.; Kim, J.; Tune, D. D.; Ambroz, F.; Li, X.; Xu, S.; Sol, C.; Papakonstantinou, I.; McLachlan, M. A.; Parkin, I. P.; Shapter, J. G.; Durrant, J. R.; Origin of Performance Enhancement in TiO₂-Carbon Nanotube Composite Perovskite Solar Cells. *Small Methods*, **2019**, 3, 1900164.
148. Yang, D.; Zhou, X.; Yang, R.; Yang, Z.; Yu, W.; Wang, X.; Li, C.; Liu, S.; Chang, R. P. H.; Surface optimization to eliminate hysteresis for record efficiency planar perovskite solar cells. *Energy & Environmental Science*, **2016**, 9, 3071-3078.
149. Xing, G.; Wu, B.; Chen, S.; Chua, J.; Yantara, N.; Mhaisalkar, S.; Mathews, N.; Sum, T. C.; Interfacial Electron Transfer Barrier at Compact TiO₂/CH₃NH₃PbI₃ Heterojunction. *Small*, **2015**, 11, 3606-3613.
150. Wojciechowski, K.; Stranks, S. D.; Abate, A.; Sadoughi, G.; Sadhanala, A.; Kopidakis, N.; Rumbles, G.; Li, C.; Friend, R. H.; Jen, A. K.; Snaith, H. J.; Heterojunction Modification for Highly Efficient Organic–Inorganic Perovskite Solar Cells. *ACS Nano*, **2014**, 8, 12701-12709.
151. Li, Y.; Zhao, Y.; Chen, Q.; Yang, Y. (.; Liu, Y.; Hong, Z.; Liu, Z.; Hsieh, Y.; Meng, L.; Li, Y.; Yang, Y.; Multifunctional Fullerene Derivative for Interface Engineering in Perovskite Solar Cells. *Journal of the American Chemical Society*, **2015**, 137, 15540-15547.
152. Tao, C.; Neutzner, S.; Colella, L.; Marras, S.; Srimath Kandada, A. R.; Gandini, M.; Bastiani, M. D.; Pace, G.; Manna, L.; Caironi, M.; Bertarelli, C.; Petrozza, A.; 17.6% stabilized efficiency in low-temperature processed planar perovskite solar cells. *Energy & Environmental Science*, **2015**, 8, 2365-2370.

153. Cojocaru, L.; Uchida, S.; Jayaweera, P. V. V.; Kaneko, S.; Wang, H.; Nakazaki, J.; Kubo, T.; Segawa, H.; Cover Feature: Effect of TiO₂ Surface Treatment on the Current–Voltage Hysteresis of Planar-Structure Perovskite Solar Cells Prepared on Rough and Flat Fluorine-Doped Tin Oxide Substrates (Energy Technol. 10/2017). *Energy Technology*, **2017**, 5, 1729.
154. Xu, Y.; Gao, C.; Tang, S.; Zhang, J.; Chen, Y.; Zhu, Y.; Hu, Z. Comprehensive understanding of TiCl₄ treatment on the compact TiO₂ layer in planar perovskite solar cells with efficiencies over 20%. *Journal of Alloys and Compounds* **2019**, 787, 1082-1088.
155. Sun, W.; Choy, K.; Wang, M.; The Role of Thickness Control and Interface Modification in Assembling Efficient Planar Perovskite Solar Cells. *Molecules*, **2019**, 24, 3466.
156. Adli, H. K.; Harada, T.; Nakanishi, S.; Ikeda, S.; Effects of TiCl₄ treatment on the structural and electrochemical properties of a porous TiO₂ layer in CH₃NH₃PbI₃ perovskite solar cells. *Physical chemistry chemical physics: PCCP*, **2017**, 19, 26898.
157. Wang, Z.; Fang, J.; Mi, Y.; Zhu, X.; Ren, H.; Liu, X.; Yan, Y.; Enhanced performance of perovskite solar cells by ultraviolet-ozone treatment of mesoporous TiO₂. *Applied Surface Science*, **2018**, 436, 596-602.
158. Huang, F.; Pascoe, A. R.; Wu, W.; Ku, Z.; Peng, Y.; Zhong, J.; Caruso, R. A.; Cheng, Y.; Effect of the Microstructure of the Functional Layers on the Efficiency of Perovskite Solar Cells. *Advanced Materials*, **2017**, 29, 1601715.
159. Yang, Y.; Ma, J.; Qin, Q.; Zhai, X.; Degradation of nitrobenzene by nano-TiO₂ catalyzed ozonation. *Journal of Molecular Catalysis A: Chemical*, **2007**, 267, 41-48.
160. Kim, Y.; Yoo, B. J.; Vittal, R.; Lee, Y.; Park, N.; Kim, K.; Low-temperature oxygen plasma treatment of TiO₂ film for enhanced performance of dye-sensitized solar cells. *Journal of Power Sources*, **2008**, 175, 914-919.
161. Ball, J. M.; Lee, M. M.; Hey, A.; Snaith, H. J.; Low-temperature processed meso-superstructured to thin-film perovskite solar cells. *Energy & Environmental Science*, **2013**, 6, 1739-1743.
162. Bi, D.; Moon, S.; Hägman, L.; Boschloo, G.; Yang, L.; Johansson, E. M. J.; Nazeeruddin, M. K.; Grätzel, M.; Hagfeldt, A.; Using a two-step deposition technique to prepare perovskite (CH₃NH₃PbI₃) for thin film solar cells based on ZrO₂ and TiO₂ mesostructures. *RSC Advances*, **2016**, 3, 18762-18766.
163. Han, G. S.; Chung, H. S.; Kim, B. J.; Kim, D. H.; Lee, J. W.; Swain, B. S.; Mahmood, K.; Yoo, J. S.; Park, N.; Lee, J. H.; Jung, H. S.; Retarding charge recombination in perovskite solar cells using ultrathin MgO-coated TiO₂ nanoparticulate films. *Journal of Materials Chemistry A*, **2015**, 3, 9160-9164.
164. Liu, Z.; Chen, Q.; Hong, Z.; Zhou, H.; Xu, X.; De Marco, N.; Sun, P.; Zhao, Z.; Cheng, Y.; Yang, Y. Low-Temperature TiO_x Compact Layer for Planar Heterojunction Perovskite Solar Cells. *ACS Applied Materials & Interfaces*, **2016**, 8, 11076-11083.
165. Tan, H.; Jain, A.; Voznyy, O.; Lan, X.; García de Arquer, F. Pelayo; Fan, J. Z.; Quintero-Bermudez, R.; Yuan, M.; Zhang, B.; Zhao, Y.; Fan, F.; Li, P.; Quan, L. N.; Zhao, Y.; Lu, Z.; Yang, Z.; Hoogland, S.; Sargent, E. H.; Efficient and stable solution-processed planar perovskite solar cells via contact passivation. *Science*, **2017**, 355, 722-726.

166. Zhou, Z.; Pang, S.; Liu, Z.; Xu, H.; Cui, G.; Interface engineering for high-performance perovskite hybrid solar cells. *Journal of Materials Chemistry A*, **2015**, *3*, 19205-19217.
167. Carnio, M.; Watson, T.; Worsley, D.; UV Filtering of Dye-Sensitized Solar Cells: The Effects of Varying the UV Cut-Off upon Cell Performance and Incident Photon-to-Electron Conversion Efficiency. *International Journal of Photoenergy*, **2012**, *2012*, 1.
168. Leijtens, T.; Eperon, G. E.; Pathak, S.; Abate, A.; Lee, M. M.; Snaith, H. J.; Overcoming ultraviolet light instability of sensitized TiO₂ with meso-superstructured organometal tri-halide perovskite solar cells. *Nature Communications*, **2013**, *4*:2885.
169. Wu, Y.; Yang, X.; Chen, H.; Zhang, K.; Qin, C.; Liu, J.; Peng, W.; Islam, A.; Bi, E. B.; Ye, F.; Yin, M.; Zhang, P.; Han, L.; Highly compact TiO₂ layer for efficient hole-blocking in perovskite solar cells. *Applied Physics Express*, **2014**, *7*, 052301.
170. Zhang, H.; Wang, H.; Ma, M.; Wu, Y.; Dong, S.; Xu, Q.; Application of Compact TiO₂ Layer Fabricated by Pulsed Laser Deposition in Organometal Trihalide Perovskite Solar Cells. *Solar RRL* **2018**, *2*, 1800097.
171. Yang, B.; Mahjouri-Samani, M.; Rouleau, C. M.; Geohegan, D. B.; Xiao, K.; Low temperature synthesis of hierarchical TiO₂ nanostructures for high performance perovskite solar cells by pulsed laser deposition. *Physical Chemistry Chemical Physics*, **2016**, *18*, 27067-27072.
172. Cong, C.; Cheng, Y.; Dai, Q.; Song, H.; Radio Frequency Magnetron Sputtering Deposition of TiO₂ Thin Films and Their Perovskite Solar Cell Applications. *Scientific Reports*, **2015**, *5*, 17684.
173. Seo, S.; Jeong, S.; Park, H.; Shin, H.; Park, N.; Atomic layer deposition for efficient and stable perovskite solar cells. *RSC Chemical Communications*, **2019**, *55*, 2403-2416.
174. Huckaba, A. J.; Lee, Y.; Xia, R.; Paek, S.; Bassetto, V. C.; Oveisi, E.; Lesch, A.; Kinge, S.; Dyson, P. J.; Girault, H.; Nazeeruddin, M. K.; Inkjet-Printed Mesoporous TiO₂ and Perovskite Layers for High Efficiency Perovskite Solar Cells. *Energy Technology*, **2019**, *7*, 317-324.
175. Padrón-Hernández, W. Y.; Ceballos-Chuc, M. C.; Pourjafari, D.; Oskam, G.; Tinoco, J. C.; Martínez-López, A. G.; Rodriguez-Gattorno, G.; Stable inks for inkjet printing of TiO₂ thin films. *Materials Science in Semiconductor Processing*, **2018**, *81*, 75-81.
176. Adnan, M.; Lee, J. K.; All Sequential Dip-Coating Processed Perovskite Layers from an Aqueous Lead Precursor for High Efficiency Perovskite Solar Cells. *Scientific Reports*, **2018**, *8*, 2168.
177. Park, J.; Shin, K.; Lee, C.; Roll-to-Roll Coating Technology and Its Applications: A Review. *International Journal of Precision Engineering and Manufacturing*, **2016**, *17*, 537-550.
178. Hossain, M. A.; Khoo, K. T.; Cui, X.; Poduval, G. K.; Zhang, T.; Li, X.; Li, W. M.; Hoex, B.; Atomic layer deposition enabling higher efficiency solar cells: A review. *Nano Materials Science*, **2019**.
179. Hu, H.; Dong, B.; Hu, H.; Chen, F.; Kong, M.; Zhang, Q.; Luo, T.; Zhao, L.; Guo, Z.; Li, J.; Xu, Z.; Wang, S.; Eder, D.; Wan, L.; Atomic Layer Deposition of TiO₂ for a High-Efficiency Hole-Blocking Layer in Hole-Conductor-Free Perovskite Solar Cells Processed in Ambient Air. *ACS Applied Materials & Interfaces*, **2016**, *8*, 17999-18007.

180. Lu, H.; Ma, Y.; Gu, B.; Tian, W.; Li, L.; Identifying the optimum thickness of electron transport layers for highly efficient perovskite planar solar cells. *Journal of Materials Chemistry A*, **2015**, *3*, 16445-16452.
181. Lu, H.; Tian, W.; Gu, B.; Zhu, Y.; Li, L.; TiO₂ Electron Transport Bilayer for Highly Efficient Planar Perovskite Solar Cell. *Small*, **2017**, *13*, 1701535.
182. Batch and Roll-to-Roll Atomic Layer Deposition (ALD) processing for ultra-barrier and other applications. <https://www.vacuum-uk.org/pdfs/vs6/ftf/cpi.pdf>. (accessed on 10.05.2020).
183. Leskelä, M.; Niinistö, J.; Ritala, M.; *Comprehensive Materials Processing* **2014**, 101-123.
184. SVT Associates, Inc. <https://www.svta.com/>. (accessed on 25.03.2020).
185. Leskelä, M.; Ritala, M.; Atomic Layer Deposition Chemistry: Recent Developments and Future Challenges. *Angewandte Chemie International Edition*, **2003**, *42*, 5548-5554.
186. Hsieh, H.; Yu, J.; Rwei, S.; Lin, K.; Shih, Y.; Wang, L.; Ultra-compact titanium oxide prepared by ultrasonic spray pyrolysis method for planar heterojunction perovskite hybrid solar cells. *Thin Solid Films*, **2018**, *659*, 41-47.
187. Gavrilovic, T. V.; Jovanovic, D. J.; Dramicanin, M. D.; Synthesis of multifunctional inorganic materials: from micrometer to nanometer dimensions. In *Nanomaterials for Green Energy*; Bhanvase, B. A., Pawade, V. B., Dhoble, S. J., Sonawane, S. H. and Ashokkumar, M., Eds.; Elsevier: 2018; pp 61-62.
188. Emslie, A. G.; Bonner, F. T.; Peck, L. G.; Flow of a Viscous Liquid on a Rotating Disk. *Journal of Applied Physics*, **1958**, *29*, 858-862.
189. How to do a sol-gel coating using spin coating technique? <https://www.spincoating.com/en/featured-items/sol-gel-coating-process-using-spin-coating/205/>. (accessed on 20.02.2020).
190. Hong, S.; Han, A.; Lee, E. C.; Ko, K.; Park, J.; Song, H.; Han, M.; Han, C.; A facile and low-cost fabrication of TiO₂ compact layer for efficient perovskite solar cells. *Current Applied Physics*, **2015**, *15*, 574-579.
191. El Haimeur, A.; Makha, M.; Bakkali, H.; González-Leal, J. M.; Blanco, E.; Dominguez, M.; Voitenko, Z. V. Enhanced performance of planar perovskite solar cells using dip-coated TiO₂ as electron transporting layer. *Solar Energy*, **2020**, *195*, 475-482.
192. Huang, L.; Li, C.; Sun, X.; Xu, R.; Du, Y.; Ni, J.; Cai, H.; Li, J.; Hu, Z.; Zhang, J. Efficient and hysteresis-less pseudo-planar heterojunction perovskite solar cells fabricated by a facile and solution-saving one-step dip-coating method. *Organic Electronics*, **2017**, *40*, 13-23.
193. Brinker, C. J.; Dip Coating. In *Chemical Solution Deposition of Functional Oxide Thin Films*; Schneller, T., Waser, R., Kosec, M. and Payne, D., Eds.; Springer: 2013; pp 233-261.
194. Jolivet, J. *Metal Oxide Chemistry and Synthesis: From Solution to Solid State*; John Wiley & Sons: Chichester, England, 2000; .

195. Xu, Q.; Järn, M.; Lindén, M.; Smått, J.; Nanopatterned zinc titanate thin films prepared by the evaporation-induced self-assembly process. *Thin Solid Films*, **2013**, *531*, 222-227.
196. Lee, S. M.; Lee, D. G.; Lee, S.; Kim, B. J.; Kim, M.; Kim, D. H.; Choi, M.; Jung, H. S.; Effect of TiO₂ particle size and layer thickness on mesoscopic perovskite solar cells. *Applied Surface Science*, **2019**, *477*, 131-136.
197. Wang, M.; Feng, Y.; Bian, J.; Liu, H.; Shi, Y.; A comparative study of one-step and two-step approaches for MAPbI₃ perovskite layer and its influence on the performance of mesoscopic perovskite solar cell. *Chemical Physics Letters*, **2018**, *692*, 44-49.
198. Li, X.; Dai, S.; Zhu, P.; Deng, L.; Xie, S.; Cui, Q.; Chen, H.; Wang, N.; Lin, H.; Efficient Perovskite Solar Cells Depending on TiO₂ Nanorod Arrays. *ACS Applied Materials & Interfaces*, **2016**, *8*, 21358-21365.
199. Ha, S.; Heo, J. H.; Im, S. H.; Moon, J. H. Mesoscopic CH₃NH₃PbI₃ perovskite solar cells using TiO₂ inverse opal electron-conducting scaffolds. *Journal of Materials Chemistry A*, **2017**, *5*, 1972-1977.
200. Yong, P.; Zhao, D.; Margolese, D. I.; Chmelka, B. F.; Stucky, G. D.; Generalized syntheses of large-pore mesoporous metal oxides with semicrystalline frameworks. *Nature*, **1998**, *396*, 152-155.
201. Grosso, D.; Cagnol, F.; Soler-Illia, G.; Crepaldi, E.; Amenitsch, H.; Brunet-Bruneau, A.; Bourgeois, A.; Sanchez, C.; Fundamentals of Mesostructuring Through Evaporation-Induced Self-Assembly. *Advanced Functional Materials*, **2004**, *14*, 309-322.
202. Ortel, E.; Fischer, A.; Chuenchom, L.; Polte, J.; Emmerling, F.; Smarsly, B.; Kraehnert, R.; New Triblock Copolymer Templates, PEO-PB-PEO, for the Synthesis of Titania Films with Controlled Mesopore Size, Wall Thickness, and Bimodal Porosity. *Small*, **2012**, *8*, 298-309.
203. Vivo, P.; Ojanperä, A.; Smått, J.; Sandén, S.; Hashmi, S. G.; Kaunisto, K.; Ihalainen, P.; Masood, M. T.; Österbacka, R.; Lund, P. D.; Lemmetyinen, H.; Influence of TiO₂ compact layer precursor on the performance of perovskite solar cells. *Organic Electronics*, **2017**, *41*, 287-293.
204. X-ray reflectivity. <http://physics.valpo.edu/staff/arichter/XRR.htm>. (accessed on 03.06.2020).
205. XPS Surface Analysis. <http://www.andersonmaterials.com/xps.html>. (accessed on 20.03.2020)
206. Bubert, H. Book Review: Practical Surface Analysis. A2, Vol. 1. Auger and X-Ray Photoelectron Spectroscopy. 2nd Edition. Edited by D. Briggs and M. P. Seah. *Angew. Chem. Int. Ed Engl.* **1995**, *34*, 2059-2060.
207. Binnig, G.; Quate, C. F.; Gerber, C.; Atomic Force Microscope. *Physical Review Letters* **1986**, *56*, 930-934.
208. Tams, C.; Enjalbert, N.; The Use of UV/ Vis/ NIR spectroscopy in development of photo-voltaic cells. *Application Note* **2009**.
209. Optical vs Electron Microscopy. <http://www.asu.edu/courses/phs208/patternsbb/PiN/rdg/elmicr/versus.shtml>. (accessed on 20.03.2020).

210. Scanning microscope information. https://engineering.dartmouth.edu/microeng/equipment/SEM/SEM_intro.html. (accessed on 20.03.2020).
211. Ritchie, N. W. M.; Newbury, D.; Joy, D. C.; Michael, J.; Goldstein, J.; Scott, J. H.; *Scanning Electron Microscopy and X-Ray Microanalysis*; 2018; .
212. Ebnesajjad, S.; *Surface Treatment of Materials for Adhesion Bonding*; Elsevier: 2014; .
213. Photoluminescence Spectroscopy and its application. <https://archive.cnx.org/contents/81bb0311-98ee-4cfc-b3c8-0eab6aeace37@2/photoluminescence-spectroscopy-and-its-applications>. (accessed on 20.03.2020).
214. DSSC: Dye Sensitized Solar Cells. <https://www.gamry.com/application-notes/physechem/dssc-dye-sensitized-solar-cells/>. (accessed on 20.03.2020).
215. Juska, G.; Arlauskas, K.; Viliunas, M.; Kocka, J.; Extraction Current Transients: New Method of Study of Charge Transport in Microcrystalline Silicon. *Physical review letters*, **2000**, *84*, 4946-4949.
216. Züfle, S.; Altazin, S.; Hofmann, A.; Jäger, L.; Neukom, M. T.; Brütting, W.; Ruhstaller, B.; Determination of charge transport activation energy and injection barrier in organic semiconductor devices. *Journal of Applied Physics*, **2017**, *122*, 115502.
217. Juška, G.; Nekrašas, N.; Genevičius, K.; Investigation of charge carriers transport from extraction current transients of injected charge carriers. *Journal of Non-Crystalline Solids*, **2012**, *358*, 748-750.
218. Sandberg, O. J.; Sandén, S.; Sundqvist, A.; Smått, J.; Österbacka, R.; Determination of Surface Recombination Velocities at Contacts in Organic Semiconductor Devices Using Injected Carrier Reservoirs. *Physical Review Letters*, **2017**, *118*, 076601.
219. Lide, D. R. C. *CRC Handbook of Chemistry and Physics*; CRC Press/Taylor and Francis Group: Boca Raton, FL: 2005; .
220. Anderson, O.; Ottermann, C. R.; Kuschnerreit, R.; Hess, P.; Bange, K.; Density and Young's modulus of thin TiO₂ films. *Journal of Analytical Chemistry*, **1997**, *358*, 315–318.
221. Sandberg, O. J.; Sundqvist, A.; Nyman, M.; Österbacka, R.; Relating Charge Transport, Contact Properties, and Recombination to Open-Circuit Voltage in Sandwich-Type Thin-Film Solar Cells. *Physical Review Applied*, **2016**, *5*, 044005
222. Moehl, T.; Im, J. H.; Lee, Y. H.; Domanski, K.; Giordano, F.; Zakeeruddin, S. M.; Dar, M. I.; Heiniger, L.; Nazeeruddin, M. K.; Park, N.; Grätzel, M.; Strong Photocurrent Amplification in Perovskite Solar Cells with a Porous TiO₂ Blocking Layer under Reverse Bias. *The journal of physical chemistry letters* **2014**, *5*, 3931-3936.
223. Somsongkul, V.; Lang, F.; Jeong, A. R.; Rusu, M.; Arunchaiya, M.; Dittrich, T.; Hole blocking Pbl₂/CH₃NH₃Pbl₃ interface. *Phys. Status Solidi RRL*, **2014**, *08*, 763-766.
224. Sandberg, O. J.; Nyman, M.; Österbacka, R.; Effect of Contacts in Organic Bulk Heterojunction Solar Cells. *Physical Review Applied*, **2014**, *1*, 024003

225. Ummadisingu, A.; Grätzel, M.; Revealing the detailed path of sequential deposition for metal halide perovskite formation. *American Association for the Advancement of Science, Science Advances*, **2018**, *4*, e1701402.
226. Yang, S.; Zheng, Y. C.; Hou, Y.; Chen, X.; Chen, Y.; Wang, Y.; Zhao, H.; Yang, H. G.; Formation Mechanism of Freestanding $\text{CH}_3\text{NH}_3\text{PbI}_3$ Functional Crystals: In Situ Transformation vs Dissolution–Crystallization. *Chemistry of Materials*, **2014**, *26*, 6705–6710.
227. Eperon, G. E.; Burlakov, V. M.; Docampo, P.; Goriely, A.; Snaith, H. J.; Morphological Control for High Performance, Solution-Processed Planar Heterojunction Perovskite Solar Cells. *Advanced Functional Materials*, **2014**, *24*, 151–157.
228. Wahl, A.; Augustynski, J.; Charge Carrier Transport in Nanostructured Anatase TiO_2 Films Assisted by the Self-Doping of Nanoparticles. *The Journal of Physical Chemistry B*, **1998**, *102*, 7820–7828.
229. Otitoju, T. A.; Ahmad, A. L.; Ooi, B. S.; Superhydrophilic (superwetting) surfaces: A review on fabrication and application. *Journal of Industrial and Engineering Chemistry*, **2017**, *47*, 19–40.
230. Ishida, N.; Fujita, D. Superhydrophilic TiO_2 surfaces generated by reactive oxygen treatment. *Journal of Vacuum Science & Technology A*, **2012**, *30*, 051402.
231. Murugadoss, G.; Mizuta, G.; Tanaka, S.; Nishino, H.; Umeyama, T.; Imahori, H.; Ito, S.; Double functions of porous TiO_2 electrodes on $\text{CH}_3\text{NH}_3\text{PbI}_3$ perovskite solar cells: Enhancement of perovskite crystal transformation and prohibition of short circuiting. *APL Materials*, **2014**, *2*, 081511.
232. Coakley, K. M.; Liu, Y.; McGehee, M. D.; Frindell, K. L.; Stucky, G. D.; Infiltrating semiconducting polymers into self-assembled mesoporous Titania films for Photostatic application. **2003**, *13*, 301–306.
233. Abrusci, A.; Ding, I.; Al-Hashimi, M.; Segal-Peretz, T.; McGehee, M. D.; Heeney, M.; Frey, G. L.; Snaith, H. J.; Facile infiltration of semiconducting polymer into mesoporous electrodes for hybrid solar cells. *Energy & Environmental Science*, **2011**, *4*, 3051.
234. Rawolle, M.; Sarkar, K.; Niedermeier, M. A.; Schindler, M.; Lellig, P.; Gutmann, J. S.; Moulin, J.; Haese-Seiller, M.; Wochnik, A. S.; Scheu, C.; Müller-Buschbaum, P.; Infiltration of Polymer Hole-Conductor into Mesoporous Titania Structures for Solid-State Dye-Sensitized Solar Cells. *ACS Applied Materials & Interfaces*, **2013**, *5*, 719–729.
235. Lantiat, D.; Vivier, V.; Laberty-Robert, C.; Grosso, D.; Sanchez, C.; Gold Nanoelectrode Arrays and their Evaluation by Impedance Spectroscopy and Cyclic Voltammetry. *ChemPhysChem*, **2010**, *11*, 1971–1977.
236. Fisher, A.; Kuemmel, M.; Järn, M.; Linden, M.; Boissière, C.; Nicole, L.; Sanchez, C.; Grosso, D.; Surface Nanopatterning by Organic/Inorganic Self-Assembly and Selective Local Functionalization. *Small* **2006**, *2*, 587.
237. Singh, R.; Sandhu, S.; Lee, J.; Elucidating the effect of shunt losses on the performance of mesoporous perovskite solar cells. *Solar Energy*, **2019**, *193*, 956–961.

238. Kaewprajak, A.; Kumnorkaew, P.; Sagawa, T.; Improved photovoltaic performance and device stability of planar heterojunction perovskite solar cells using TiO₂ and TiO₂ mixed with AgInS₂ quantum dots as dual electron transport layers. *Organic Electronics*, **2019**, *69*, 26-33.
239. Mohamad Noh, M. F.; Teh, C. H.; Daik, R.; Lim, E. L.; Yap, C. C.; Ibrahim, M. A.; Ahmad Ludin, N.; Mohd Yusoff, Abd. Rashid bin; Jang, J.; Mat Teridi, M. A.; The architecture of the electron transport layer for a perovskite solar cell. *Journal of Materials Chemistry C* **2018**, *6*, 682-712.
240. Jeong, I.; Park, Y. H.; Bae, S.; Park, M.; Jeong, H.; Lee, P.; Ko, M. J.; Solution-Processed Ultrathin TiO₂ Compact Layer Hybridized with Mesoporous TiO₂ for High-Performance Perovskite Solar Cells. *ACS Applied Materials & Interfaces*, **2017**, *9*, 36865-36874.
241. Makuta, S.; Liu, M.; Endo, M.; Nishimura, H.; Wakamiya, A.; Tachibana, Y.; Photo-excitation intensity dependent electron and hole injections from lead iodide perovskite to nanocrystalline TiO₂ and spiro-OMeTAD. *Chemical Communication*, **2016**, *52*, 673-376.
242. Zhang, H.; Liu, M.; Yang, W.; Judin, L.; Hukka, T. I.; Priimagi, A.; Deng, Z.; Vivo, P.; Thionation Enhances the Performance of Polymeric Dopant-Free Hole-Transporting Materials for Perovskite Solar Cells. *Advanced Materials & Interfaces*, **2019**, *6*, 1901036.
243. Tress, W.; Yavari, M.; Domanski, K.; Yadav, P.; Niesen, B.; Correa Baena, J. P.; Hagfeldt, A.; Graetzel, M.; Interpretation and evolution of open-circuit voltage, recombination, ideality factor and subgap defect states during reversible light-soaking and irreversible degradation of perovskite solar cells. *Energy & Environmental Science*, **2018**, *11*, 151-165.
244. Saliba, M.; Orlandi, S.; Matsui, T.; Aghazada, S.; Cavazzini, M.; Correa-Baena; Juan-Pablo; Gao, P.; Scopelliti, R.; Masconi, E.; Dahmen, K.; Angelis, F. D.; Abate, A.; Hagfeldt, A.; Pozzi, G.; Graetzel, M.; Nazeeruddin, M. K.; A molecularly engineered hole-transporting material for efficient perovskite solar cells. *Nature Energy*, **2016**, *1*, 15017.
245. Liu, M.; Endo, M.; Shimazaki, A.; Wakamiya, A.; Tachibana, Y.; Identifying an Optimum Perovskite Solar Cell Structure by Kinetic Analysis: Planar, Mesoporous Based, or Extremely Thin Absorber Structure. *ACS Applied Energy Materials*, **2018**, *1*, 3722-3732.
246. Li, C.; Li, Y.; Xing, Y.; Zhang, Z.; Zhang, X.; Li, Z.; Shi, Y.; Ma, T.; Ma, R.; Wang, K.; Wei, J.; Perovskite Solar Cell Using a Two-Dimensional Titania Nanosheet Thin Film as the Compact Layer. *ACS Applied Materials & Interfaces*, **2015**, *7*, 15117-15122.

